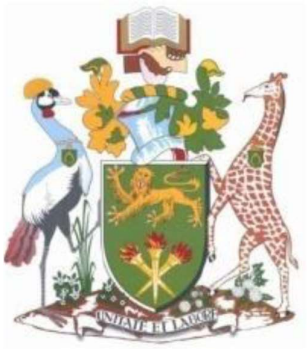

UNIVERSITY OF NAIROBI

ASSESSMENT OF THE INFLUENCE OF ASTRONOMICAL PARAMETERS ON THE SKILL OF RAINFALL FORECASTING IN EAST AFRICA

ROGER WAMBUGU NDICHU

I56/7753/2017

A DISSERTATION SUBMITTED IN PARTIAL FULFILMENT OF THE REQUIREMENT FOR MASTERS OF SCIENCE DEGREE IN METEOROLOGY AT THE DEPARTMENT OF METEOROLOGY, UNIVERSITY OF NAIROBI

AUGUST 2019

DECLARATION

I hereby declare that this dissertation is my original work and has not been submitted anywhere else for examination, award of degree or publication. Where other people's work or my own work has been used, this has properly been acknowledged and referenced in accordance with the University of Nairobi's requirements.

…….……. Date……..…….……..….

ROGER WAMBUGU NDICHU

I56/7753/2017

Department of Meteorology

School of Physical Sciences

University of Nairobi

This dissertation has been submitted for Examination with our approval as University supervisors;

…….. ……

Date……..…….…. Date……..…….….

PROF. J. ININDA DR. F.J. OPIJAH

Department of Meteorology Department of Meteorology

University of Nairobi University of Nairobi

P.O Box 00100-30197 P.O Box 00100-30197

Nairobi, KENYA. Nairobi, KENYA.

DEDICATION

This work is dedicated to all those who believe in the signs of the heavens and their influences in our climate system. This include the traditional forecasters who dwell on the physical observation of the heavens and their enduring work in telling the future of the climate conditions by use of these observations. Not forgetting the unfortunate misunderstanding of their work by some and the much respect accorded to them by many others due to their near accurate predictions in areas they operate.

I further dedicate this work to my father who valued education and hard work and always encouraged me to further my education. He was particularly happy when I embarked on this work and would have wanted to see the output.

Next, my maternal great grandfather who used his long experience in watching the skies to foretell the future weather conditions at a period when technology was not well developed. I am told he forecasted weather with good accuracy and never missed an event. Because of his experience, he was revered by the local people including the Mau-Mau warriors who would consult him on weather matters before embarking on long armed excursions into enemy territory.

Although the two are no longer with us, their good memories continue to control and guide my life.

ACKNOWLEDGEMENTS

I wish to express my appreciation for the guidance and suggestions provided by my supervisors Prof. J.Ininda and Dr. F. Opijah including the entire staff of UON-Meteorology Department. Their guidance during the period of my study gave me a lot of encouragement and understanding especially during difficult times.

To Dr. Opijah, I am much grateful to you for agreeing to supervise my work and taking up a lot of your time, going back and forth, to ensure that my input in this work stands the test of time.

I cannot forget to thank posthumously and most sincerely Prof. Ininda who passed on as he was waiting for the final draft of this study. I cannot forget his personal and immense interest in this work that inspired me to give this work a little more attention than I had envisaged.

I am grateful to all my friends and acquaintances who in one way or another contributed indirectly to this work some of whom deserve a special mention; David Njoroge, Eddie Muriuki, Dr. Richard Muita and the late Dr. Samuel Marigi. They may not know how much they influenced me to join the Msc. Program and their constant prodding to present this work (then an idea) as a project work in the program. I also posthumously thank Dr. Marigi for his useful suggestions and offering to be my future supervisor if I intended to further my studies.

I feel greatly indebted to my parents, my family and especially my wife who would wait on me as I burnt midnight oil doing my work to ensure that it was complete in time. That cup of tea she offered me at mid night kept me going.

Finally, to the ALMIGHTY GOD. I prayed to you for the success of this work and you answered my prayer. Thank you!

ABSTRACT

Seasonal forecasts generated in East Africa have mainly used the SST-based models in the last two decades with challenges of poor forecasting skills. In particular, the method of forecasting rainfall extremes has been too general and that these extremes occur much more frequently than forecasted. And furthermore, no forecasting model in use in the region provides the temporal variation or the intra-seasonal-to-interannual variability of rainfall. In addition to the low skills, the traditional Indigenous Knowledge (IK) forecasting methods are falling out due to climate change. One component of the IK, the astronomical observations, is viewed with a lot of scepticism and is considered as a non-science, therefore, inhibiting its application in science-based forecasting and research.

This study focuses on astronomical observations in its objective which is to determine the influence of the orbital parameters of planets and the moon on the weather and climate patterns in East Africa.

Results generated show that Saturn, Jupiter, Venus and Mars have a relationship with rainfall but at different levels. Both MAM and OND in all zones seem to show a variation from year to year that indicates strong astronomical influence in most cases. We also note that rainfall characteristics during two similar celestial phases but which occur at different times of the year are different, however, rainfall characteristics associated with the same observed phase and in the same month or period were found to be nearly the same.

To get to the same phase in the same month of the year, would take Saturn 30 years, Jupiter 12 years, Mars 15 years and Venus 8 years giving rise to what is refered to here as Saturn Rainfall Cycle, Jupiter Rainfall Cycle, Mars Rainfall Cycle and Venus Rainfall Cycle respectively. That means that the East African rainfall varies in cycles of 8, 12, 15 and 30 years. The rainfall cycles are easily determined by use of their key phases and can be predicted by use of astronomical calculations with little error and with sufficient accuracy way ahead of time.

Further, by using historical information, it was found out that severe climate extremes occur during the conjunctions of both Uranus and Neptune where Uranus takes ~83 years and Neptune takes ~163 years to orbit to the next conjunction. These periods, now called Uranus rainfall cycle and Neptune rainfall cycle respectively, coincide with the variation of severe extreme events in the study area. We can attribute those variations to the two planets' orbital motions.

The probabilistic models developed here use probability of occurrence or exceedance and have five categories; “Extreme Low”, “Below Normal”, “Normal”, “Above Normal”, “Extreme High” and “Phenomenal”. Using the probabilities of occurence on 2018 rainfall seasons, a qualitative verification process indicated relatively high probability values of up to 67% under “Above Normal” and “Extreme High” for MAM 2018 forecast in areas that mainly fall in the highlands East of the Riftvalley, while the period OND indicated high probability values of up to 83% under the category “Below Normal”. The season MAM 2018 was extremely wet and OND 2018 was extremely dry which means the probabilities had captured the extremes as projected.

Generally, from the results, it was found out that the planets have a relationship with the East African rainfall. Each one of them showed a certain level of contribution to the variation of monthly rainfall with the Planet Saturn indicating the biggest influence. The moon had relatively little influence to the monthly rainfall variation compared to the planets.

The phases of the planet can be hindcasted back in time to allow a dependable determination of rainfall variation of the past. In general, the use of these astronomical phases can be used to generate past and future climate scenarios in the region that can add useful body of knowledge to climate science that can be integrated in scientific reports like the IPCC Assessment Reports.

TABLE OF CONTENTS

LIST OF FIGURES

LIST OF TABLES

LIST OF SYMBOLS

☽	Moon
♄	Saturn
♂	Mars
♃	Jupiter
♅	Uranus
♀	Venus
☿	Mercury
♆	Neptune
$RR_{\psi-}$	Rainfall amount associated with planet ψ when observed in the Superior Conjunction phase
$RR_{\psi+}$	Rainfall amount associated with planet ψ when observed in the Opposition or Inferior Conjunction phase
$RR_{i\psi-}$	Rainfall amount in month i associated with Planet ψ when observed in the Superior Conjunction phase
$RR_{i\psi+}$	Rainfall amount in month i associated with Planet ψ when observed in the Opposition or Inferior Conjunction phase
$\overline{RR}_i$	Average Rainfall in the i^{th} month
$\overline{RR}'_{i,\psi_+}$	Average Rainfall Anomaly on month i during the period when the planet ψ is observed in the Opposition or Inferior Conjunction phase
$\overline{RR}'_{i,\psi_-}$	Average Rainfall Anomaly on month i during the period when the planet ψ is observed in the Superior Conjunction phase
P_{ij}	Probability of exceeding RR mm in i^{th} month of the year for j number of years
$P_{ij\psi_+}$	Probability of exceeding RR mm of rainfall in i^{th} month of the year for j number of years when the planet ψ is observed in the Opposition or Inferior Conjunction phase
$P'_{ij\psi_-}$	Probability Anomaly of exceeding RR mm of rainfall in i^{th} month of the year when the planet ψ is observed in the Superior Conjunction phase
ψ	Symbol used in this study to generally represent a planet

LIST OF ABBREVIATIONS AND ACRONYMS

ACF	Auto Correlation Function
AMO	Atlantic Multidecadal Oscillation
CLIVAR	Climate Variability and predictability
CMSS	Centre of Mass of the Solar System
CCD	Consecutive Dry Days
CWD	Consecutive Wet Days
CORDEX	Coordinated Regional Downscaling Experiment
DJF	December January February
ENSO	El Nino Southern Oscillation
ETCCDI	Expert Team on Climate Change Detection and Indices
EWMA	Exponentially Weighted Moving Average
FMA	February March April
GCM	General Circulation Models
GEV	Generalised Extreme Value
GHA	Greater Horn of Africa
GHACOF	Greater Horn of Africa-Climate Outlook Forum
GP	General Pareto
ITCZ	Inter-Tropical Convergence Zone
IOD	Indian Ocean Dipole
IK	Indigenous Knowledge
IPCC	Intergovernmental Panel on Climate Change
JCOMM	Joint WMO-IOC Commission for Oceanography and Marine Meteorology
JJA	June July August
KMD	Kenya Meteorological Department
LTM	Long Term Mean
LOD	Length of Day
MAM	March April May
MJO	Madden-Julian Oscillation
MM	Millimetres
NASA:	National Aeronautics and Space Administration
NHMs	National Hydrological and Meteorological services
NOAA	National Oceanic and Atmospheric Administration

OND	October November December
PCA	Principal Component Analysis
PDO	Pacific Decadal Oscillation
POT	Peaks over threshold
PRCPTOT	daily precipitation amount
PRESAO	Programme de Reinforcement et de Recherche sur la Sécurité Alimentaire en Afrique de l'Ouest.
QBO	Quasi-Biennial Oscillation
R95p	Moderate / very wet days
R99p	Extremely wet days
RCOF	Regional Climate Outlook Forum
SARCOF	Southern Africa Regional Climate Outlook Forum
SST	Sea Surface Temperature
TMA	Tanzania Meteorological Agency
WMA	Weighted Moving Average
WMO	World Meteorological Organization

CHAPTER ONE: INTRODUCTION

1.1 Background

For a long time, possibly hundreds or thousands of years, populations around the world have been fascinated by the heavenly bodies, their movements, especially the retrogrades, changes in brightness and colour and most of all their association to the local weather and climate events. People's lives have been dictated by the wide range of evolvement of the general constellation of the stars which is one area of science studied for a long time.

The early civilizations began the art of weather forecasting by using reoccurring astronomical observations and relating them with meteorological events in an attempt to monitor seasonal changes in weather. Many local people whose lives and livelihoods depended on the weather and climate relied also on folklore to forecast weather. These folklores and knowledge were passed down through generations and have become part of different cultures in many parts of the world. This art of forecasting weather was based on geocentric planetary alignments and may have begun in the ancient Mesopotamia (Krupp, 2003; Scofield, 2010).

Around 650 B.C., the Babylonians attempted to make short-term predictions on weather changes based on the appearance of clouds and some optical phenomena. By 300 B.C., Chinese astronomers had developed a calendar based on festivals, each associated with a unique type of weather condition (Krupp, 2003; NOAA, 2017; Scofield, 2010).

Around 340 B.C., Aristotle, a Greek philosopher, wrote a philosophical paper, *Meteorologica*, that had theories on development of weather elements like rain, wind, hail, clouds, thunder, lightning and hurricanes. He made observations on weather in an attempt to make a forecast, and his ideas in the paper were considered in the scientific world then to be the authority on key weather concepts for nearly 2000 years (NOAA, 2017; Scofield, 2010). It was further developed by the Greeks, the Arabs and others with key scientists like Ptolemy, Al-Kindi, Tycho Brahe and Joannes Kepler making enormous contributions during the Renaissance period of the 17th century.

However, the astronomical observations and subsequent interpretations made by the astronomers and meteorologists were not always correct and sometimes they did not work. This behaviour has the hallmarks of a climate change problem that the meteorologists in the past probably never considered at the time. That is why Aristotle's claims and ideas were taken to be erroneous even after making those observations at the time. It was unfortunate that during the 17th century many of his concepts were rejected. Almost same problem befell John Goad who made forecasts based on ideas of earlier scientists as given in *Astro-Meteorologica* but which were opposed and criticised and never given the necessary attention (Krupp, 2003; Scofield, 2010).

In the recent times, attempts have been made by scientists to relate astronomical cycles with meteorological and geophysical variations, sunspot numbers, Length of Day (LOD), electromagnetic energy, solar system barycentre, atmospheric and oceanic tides and the gravitational forces by the planets. (Wilson, 2008; Scafetta, 2010, 2014; Hung 2007, Goulter, 2003; Lindzen, 1967; Ivanov, 2002). These scientists have established that variations in meteorological parameters are due to atmospheric modulations related to astronomical factors.

Even more recent studies (e.g. Scafetta, 2010) suggest that the most dominant drivers of the climate oscillations have an astronomical origin. However, there has been opposition to this line of thought just like it had been during Goad's time. Some scientists are of the opinion that the gravitational forces from the planets are too small. Further, the studies indicate that since the gravitational forces generated by the planets are small, it does not make sense to believe that the planets play any role in modulating solar and terrestrial climate. This line of thought has been disputed by Hung (2007) and Scafetta (2010).

With the advent of modern science, the use of the celestial bodies in forecasting has not been given the attention it deserves and has generally been left out by scientists as it is considered a non-science and therefore has been relegated to the local community forecasters with Indigenous Knowledge (IK) to use.

Today, some scientists have gradually started to embrace newer methods with somewhat unconventional approach to seasonal forecasts (NOAA, 2017; Zuma-Netshiukhwi *et al.*, 2008; Ouma, 2009; Boko *et al.*, 2007; Zuma-Netshiukhwi *et al.*, 2013; Mapfumo *et al*., 2015) while some are moving towards Indigenous Knowledge (IK) jurisdiction or gaining support from it, the old forecasting skills have started showing signs of weakening in some areas in the region. It is probably this same problem that had been recurring for many years in the past.

In the conventional seasonal rainfall forecasts given over East Africa, it has been noted that there is a gap in forecasting skill. For example, Mason and Chidzambwa (2008), in their publication on the near 10-year verification period, deduced that below-normal rainfall was the most forecast category in the GHA in both the long rains and short rains seasons but the actual situation is different.

In this study, we introduce and employ forecasting methods that are not the usual conventional procedures of weather forecasting and climate prediction. The current conventional methods have a certain level of success but there is a huge gap to fill in the forecasting skills in the region. With even a higher occurrence of extremes in the recent past, a demand for well-developed forecasts of extremes has been on the rise and, unfortunately, none of the existing models or methods can provide an appropriate and satisfactory solution.

In this study, discussions were done on forecasts developed by Greater Horn of Africa-Climate Outlook Forecasts (GHACOF) and their weaknesses and it also addresses the role of the moon and the "stars" in IK forecasting and the Climate Change issues that are weakening forecasting skills in both scientific-based and traditional methodologies.

The study is aimed at demonstrating that monthly rainfall can be successfully modelled using factors derived from time variations of the Sun-lunar and Sun-planet factors using simple geometry. Rainfall can, therefore, be forecasted well ahead of time as the astronomical quantities can be calculated with accuracy many years ahead.

1.2 Statement of the Problem

Weather and Climate information has gradually become important and Regional Climate Outlook Forums (RCOF) and National Hydrological and Meteorological Centres (NHMC) have enhanced the exchange of information on seasonal forecasts among forecasters, researchers and different users in the region. However, many studies on scientific climate and weather in some parts of Africa show a serious problem that still exists between climate information provided at the source and climate information anticipated by the user. This includes an even bigger problem of inaccurate forecasts and low forecasting skills.

Inaccurate and generalised forecasts remain a major problem that leads to an acceptance challenge and a further challenge in effective use of the seasonal forecasts by users. It is noted that accuracy tends to decrease with smaller forecast units and localised information has a

tendency towards uncertainty and making it more accurate requires sufficiently long observational records.

Seasonal forecasts generated in the region mostly use the SST-based models that are usually given most weight in the development of the forecasts. That has been the practise in the last two decades and although in the recent past the Greater Horn of Africa-Climate Outlook Forum (GHACOF) has integrated the dynamical models in their forecasts, forecasting skill has not improved much (Kilavi and Colman, 2012).

Also, some forecasts of extremes are not well developed which is a common characteristic of the seasonal forecast modelling at the GHACOF (Goddard *et. al*., 2010; Frimpong, 2013; Ogallo, 2010). The method of forecasting rainfall extremes -both extremely low rainfall leading to drought conditions or extremely high rainfall leading to flooding conditions- is too general. In reality, these extreme conditions occur much more frequently than forecasted, which means forecasting skill for extremes is low.

Up to now, forecasters have not been able to account for deficiencies in forecasting models that do not factor in modes of intra-seasonal-to-interannual variability even with better and improved ENSO predictions (Goddard *et al*., 2010). It should be noted that overestimated probabilities, especially of the normal category, tend to reduce the effective use of many of these predictions and the usefulness of their applications. Although there is increased skill in forecasting seasonal rainfall in East Africa, it is still difficult to simulate convective precipitation that produces extreme rainfall, a problem faced by climate scientists today (Chidzambwa & Mason, 2008; Goddard *et al*., 2010). In addition to low skill, the alternative traditional weather forecasting methods using local indigenous knowledge are falling out as indicators and some other indicators are fast disappearing due to change in climate conditions.

One of the greatest drawbacks in IK applications -especially in astronomy- is the negative perceptions it has had to both climate scientists and IK adherents. In addition, policymakers in the region tend to view the application of IK for climate forecasting with a lot of scepticism (Briggs & Moyo, 2012; Saitabau, 2014). The use of celestial bodies layout and motions (of the planets and the moon) in the sky is considered a non-science and is classified as Indigenous Knowledge, therefore inhibiting its application in science-based forecasting and research. Scientific methods for climate forecasting are considered to be superior than the ‘conservative’ and ‘backward’ indigenous knowledge that most local farmers depend on.

1.3 Objectives of the Study

The main objective of this study is to determine the influence of the orbital parameters of planets and the moon on the monthly rainfall patterns in East Africa.

The specific objectives are to:

a) Assess the planets and the moons influence on the rainfall over East Africa;

b) Assess the intra-seasonal and inter-annual variations of rainfall for the given zones in East Africa; and

c) Assess the variation of the probabilities of rainfall exceedance or occurrence (in a season) associated with key phases of the celestial bodies for different homogenous rainfall zones.

1.4 Justification of the Study

In the recent past, climate conditions in the region have been rather erratic in time and space where the traditional weather conditions have changed resulting into an unfamiliar forecasting future. This has resulted in the climate sensitive users like the farmers (especially in dry and marginally dry areas) to start getting worried.

Access to seasonal weather forecasts helps farmers who are vulnerable to extreme weather in the region to make informed farming decisions. By choosing the most appropriate seeds and appropriate planting dates for the likely forecasted weather and climate conditions, farmers will look forward to increases in their yields as a result of forecasts based on this new methodology.

One sector mostly affected by intra-seasonal variability of rainfall is agriculture which is highly exposed to extremes that occur from year-to-year. A reason why the extremes are often so devastating to agriculture is that we do not know when they will occur next or how the next growing season will look like (Jones *et. al*., 2000). Future climatic uncertainties often lead to the use of common traditional strategies to survive and that means sacrificing some productivity to reduce risks. However, the new methodologies in this study promises to give better predictions of future climate conditions that are available well ahead of time and this will definitely influence farming decisions that mitigate unwanted impacts and unfavourable conditions.

For countries in the GHA, developing weather services to produce reliable forecasts often does not appear as a priority as such services are seen as a luxury, rather than a necessity. In the recent times, weather extremes are causing more and more human and economic losses, and in some cases the losses increase more rapidly than wealth creation. The development of a new forecasting method will result in a better warning system for the extremes and will benefit the local populations in terms of saved human lives and reduced property losses.

A further benefit from studying rainfall characteristics during certain key celestial body phases is to enhance our understanding of rainfall variability within the season to help improve the short-range, medium range and seasonal forecast made available to users (Warren *et al.,* 2002). Surveys done by Sonka *et al.*, (1992) show that users are not only concerned with rainfall totals for any season as is the norm with forecasts in the GHA, but also that they would benefit from more detailed forecasts that includes the spread of rainfall over time and space (Vogel, 2000) and particularly forecasts that include periods when the rainy season will set in so that farmers can make appropriate preparations (Obert *et al.*, 2016). Levey and Jury (1996) also noted the significance of the temporal distribution of rainfall within a season and understanding the characteristics of the wet and dry spells to agriculture which is a common problem in the GHA. Now that our new methodology introduces temporal distribution within a season, users will benefit from it as it indicates periods of wetness and periods of drought.

1.5 The Area of Study

The scope of this study covers the East African countries (Uganda, Tanzania, Kenya, Rwanda and Burundi) which is defined as the area within, 11.8°S to 5.2°N, 28.8°E to 41.9°E (Figure 1).

The area has an extensive range of unique terrain features that includes large areas under plain land, plateaus, mountains and mountain ranges, the rift valley, large rivers, lakes and wetlands (Goudie, 1996). Among these features, are Lake Victoria, the third largest in the world by size, and Lake Tanganyika, the third largest by volume (Salzburger *et. al*., 2014). One of Africa's well-known geological feature, the Rift Valley, has two sides; the Eastern branch and Western branch, on either side of Lake Victoria. The Great Rift Valley—as it is known—is a creation of complex geological processes that are responsible for the formation of most of the largest lakes and contribute immensely to the large variations in its topography. The rugged and rough escarpments bordering the Rift Valley have particularly dramatic formations in Kenya (Nyamweru, 1996). Two of the highest mountains in Africa, Mt. Kilimanjaro and Mt. Kenya are found here.

The region experiences a biannual rainfall pattern with two major rainfall peaks falling in the "long rains" season, March–May (MAM) and the "short rains" season, October–December (OND) (Shongwe *et al*., 2010). While the main OND seasonal rainfall may fall during October to December in some parts of the region, some other parts may experience the season from the month of September and it is a commonly accepted practise to call it OND (Anyah and Semazzi 2007).

The East Africa's climate is predominantly tropical and has a variety of climate conditions and a typical equatorial climate with characteristically high temperatures most of the year with little seasonal variation. Rainfall is mainly controlled by the Inter-Tropical Convergence Zone (ITCZ) and is strongly influenced by El Niño, and typically when this phenomenon prevails, the region receives more rainfall than normal. In almost all cases, El Niño is followed immediately by La Niña. However, when La Niña prevails, the southern parts of the region normally experience a drier-than-normal condition between November and March (WMO, 2013).

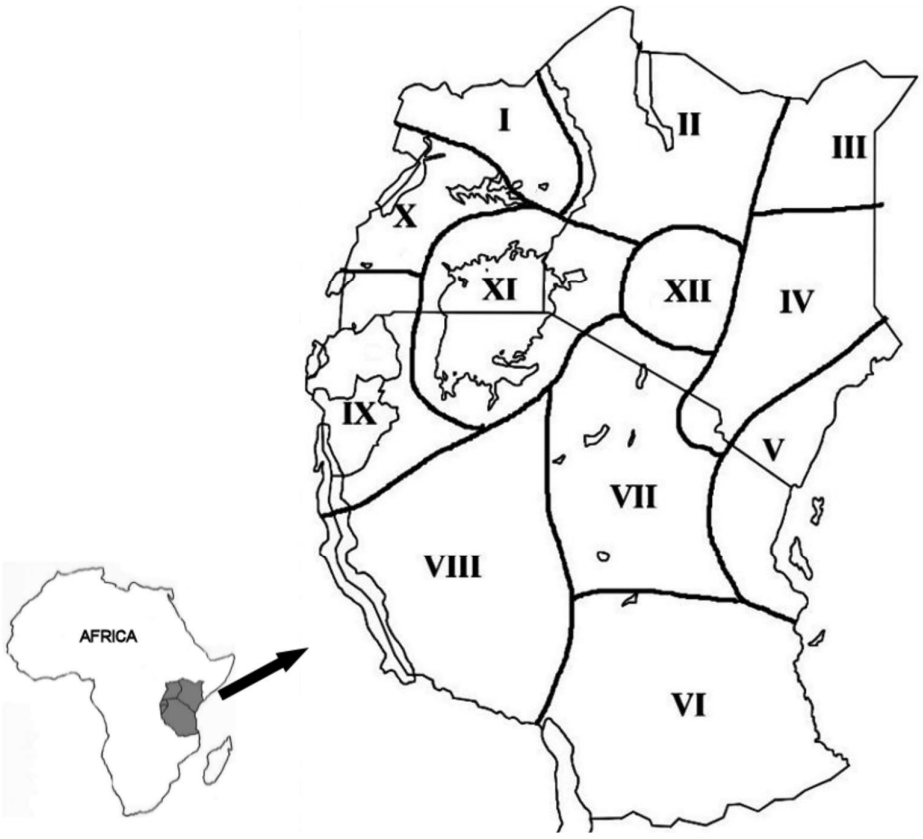

Figure 1 : Map of East Africa with demarcated 12 climatic zones I to XII covering the whole region (adopted and modified from Indeje *et al*., 2000 and ICPAC, 1999).

Other drivers of climate in the region are the Quasi-Biennial Oscillation (QBO), Indian Ocean Dipole (IOD), Easterly Waves and Madden Julian Oscillation (MJO), to name but a few.

This region is divided into 12 broad zones (Figure 1) based on the demarcations done in the study by Indeje *et al.,* (2000) and refined by integrating the earlier works on the same done for individual countries in ICPAC (1999). These zones were formed by generating homogeneous rainfall zones using principal component analysis (PCA) on historical precipitation dataset provided from the synoptic stations in the region.

CHAPTER TWO: LITERATURE REVIEW

This chapter is divided into six main segments; 2.1, Current Tools Used in Forecasting Seasonal Rainfall in the Region; 2.2, Indigenous Knowledge in Seasonal Rainfall Forecasting; 2.3, Rainfall Forecasting Using Indigenous Knowledge on Moon Characteristics, 2.4, The Use of Planets in Indigenous Rainfall Forecasting; 2.5, The "Stars" Observed in Indigenous Forecasting and Associated Planets; 2.6, Atmospheric Tides, Astronomical Cycles and Meteorological Variations; and 2.7, Determination of Rainfall Extremes in the Region.

2.1 Current Tools Used in Forecasting Seasonal Rainfall in the Region

The seasonal rainfall forecasts for the GHA region are issued by the Regional Climate Outlook Forum (RCOF) for the region, the Greater Horn of Africa-Climate Outlook Forum (GHACOF) for three main seasons; October-December (OND), June-August (JJA) and March-May (MAM). The forecasts are given as rainfall totals in three; above normal (AN), normal (N), and below normal (BN) rainfall categories.

The first regional forecast, GHACOF, was organised in Nairobi in 1999 to forecast seasonal rainfall for the GHA forum. The following years were a period of concerted research into the methodology and prediction skills of the seasonal rains. Since these early beginnings there has been a marked development in forecasting techniques and increased international collaboration to standardise prediction formats. For example, Graham *et al.* (2012) noted that many prediction centres in the region had replaced atmospheric systems influenced by SST anomalies, with coupled ocean-atmosphere systems.

Statistical methods of prediction are still popular and currently dominate forecast development at the GHACOF and at the National Hydrological and Meteorological Services (NHMSs) in the region. The methods are typically based on empirical-statistical relationships between historical seasonal rainfall data, typically from stations representing different homogenous rainfall zones, and pre-season (mainly tropical Indian, and Pacific oceans) SSTs anomalies (Graham *et. al*, 2012). It should be noted that predictors used at the GHACOF workshops are not limited to SST-based parameters, but these parameters dominate in the stepwise regression process.

However, when Mason and Chidzambwa (2008) conducted a verification study in the first ten years of operation on the forecasts from the three regions, PRESAO, SARCOF and GHACOF, they realised there was a problem that required attention. They concluded that the forecasts had systematic errors, with a tendency to overestimate.

Mason and Chidzambwa (2008) also found out that the forecasts for the MAM period showed poor judgement, with correct rates of only 56%, 49%, and 53% for the above normal, normal, and below-normal categories, respectively. They further showed the forecasts indicated poor resolution and reliability, although MAM season in this region is generally considered to be problematic to forecast and possesses relatively poor predictability. The Mason and Chidzambwa (2008) study further shows some serious biases in the forecasts which indicated a predominance of below-normal rainfall observed at 55% of the time, with the average forecast probability at 30%. It is the same issue with the average forecast probability for normal rainfall category at 40%, but occurred at only 31% of the time, while the corresponding values for the above-normal category were 30% and 14%, which is less than half of the forecasts. Some few cases of forecasted above-normal rainfall represented a huge difference from the climatological period and even the observed, and it was noted by Mason *et al*., 2008 that a failure of the forecasts to provide or indicate a reason for this shift in the forecast was considered a major weakness of the forecasting process in GHACOF.

The most common error noted by Mason and Chidzambwa (2008) for GHACOF forecasts was the bias of the forecasts towards the normal category. The probabilities determined for the normal category were found to be consistently higher than normal, and the normal rainfall received occurred notably much less often and less widely than given in the forecasts. Again, to make it worse, the increased probabilities for the normal category is not supported by evidence of any skill in forecasting. More generally, the probabilities usually show poor reliability which calls for a need to re-define the probability categories and possibly increasing the number of categories to probably five, which again, points to a need to evaluate the scientific thinking for the predictions (Mason and Chidzambwa, 2008). Unfortunately, the GHACOF has not provided any clear indications of solving these problems, therefore, the problems continue to persist.

The challenge cuts across all other RCOFs where verification results attained reflect on some level of failure. Hyvärinen *et. al*., 2015, when conducting verification of seasonal rainfall forecasts in Zambia and Malawi showed that the forecasts were somewhat reliable, but with a very low resolution. The forecasts also showed lack of contrasts as probabilities for one

category were found to be rarely higher than 40 % or less than 25 %. This sharpness that is supposed to define extremity is lacking in the RCOFs forecasts which means extremes are never forecasted.

In the past, seasonal forecasting in the RCOF process has been based primarily on the formulation of the multiple linear regression equation models using the classical statistical forecasting methods and the forecast time lag is built into the regression models (Wilks 2006). In more recent years, regression-based models in the forecasting centres have been used to downscale the outputs of General Circulation Models (GCMs) from some of the WMO-designated Global Producing Centres (GPCs) and other dynamical modelling centres (Mason and Chidzambwa, 2008), but has not been smooth sailing even with the new dynamical models.

However, all cannot be said to be negative as the dynamical prediction methodology has shown a little positive improvement in RCOF predictions. For example, Kilavi and Colman (2012) have developed a statistical-dynamical prediction approach for homogenous climatic zones of Kenya. In this combination, there was an attempt to include other predictors in the models for each selected zone, indices of dynamical model output, the SSTs and the atmospheric circulation indices. These are indices drawn from precipitation, the Principal Components (PCs) of model precipitation and the 850 *hPa* wind field.

Unfortunately, the results from the Kilavi and Colman (2012) study were not encouraging in some zones. Results so far indicated the need for further research to understand the statistical-dynamical models much more so that models can attain higher prediction skills. While methods and indicators or predictors used here are mainly the conventional type, there is need to expand this to other unconventional methods to fill in the gaps left out by the models.

2.2 Indigenous Knowledge in Seasonal Rainfall Forecasting

The use of the indigenous knowledge in forecasting has been part and parcel of the lives of the local East African populace for centuries. Many people who employ the use of indigenous knowledge use a variety of natural indicators, most of which are associated with short term weather forecasting and seasonal climate prediction (Zuma-Netshiukhwi *et al*, 2013).

For instance, Zuma-Netshiukhwi *et al,* 2013, indicated that most farmers in his area of study, South Africa, were not accustomed to the use and the application of science-based forecasts - weather forecasts or climate predictions. The farmers depend much on their past observational experiences, sometimes handed down from generation to generation, and local traditional

knowledge to do their farming. Traditional weather forecasts and climate predictions differ across communities, cultural background, and environment around the area under forecast (Garay-Barayazarra *et. al.*, 2011; Hart, 2007). These traditional skills, from many years of experience, are not well understood by most scientists, and are considered non-science while they have been found to be in regular use by farmers. These skills involve indicators which range from the configuration or the constellation of "stars" and the moon, cloud cover, animal behaviour, ants, behaviour of indigenous trees, to migration of birds and mammals and many others (Zuma-Netshiukhwi *et. al.*, 2013; Merchant*,* 1987*;* Olbrich *et. al.,*2003; Prendergast, 1999).

Nonetheless, in this study we will focus on the astronomical indicators as used in Indigenous Knowledge (IK) and discuss them in a little more detail as applied in different parts of Africa and more so in East Africa. In addition, in this study will consider the behaviour of the moon and the "stars" in the sky and how they are interpreted across communities to forecast weather and make climate predictions. These interpretations should be able to tell us something about the use astronomy that we can apply in this study.

2.3 Rainfall Forecasting Using Indigenous Knowledge on Moon Characteristics

In IK forecasting, there are many unique applicable indicators of meteorological and astronomical origin that include wind direction and strength, "star"-moon alignments, observed direction of the moon, colour of the moon, nature of the moon crescents, relative movement of "stars", types of clouds at certain periods, temperature conditions, colour of the sky, rainbow and others. These indicators are used to forecast the performance of the following rainy season (Graham *et al*., 2012).

In any location in GHA, not all astronomical indicators mentioned above are used. Some of those applied seem to work better than others and have varying levels of acceptance from region-to-region depending on their precision in seasonal prediction or weather forecasted. For example, the "stars" and moon alignments are the most applicable weather information sources in Borana tribe of Kenya and Ethiopia, while cloud colour is the preferred indicator in some communities in southern Africa. When one travels across the region, one notices a lot of confidence and widespread use of traditional forecasts, and especially "star" and moon watching for weather forecast and climate prediction (Graham *et al*., 2012).

To demonstrate how much astronomy is in use to forecast weather and climate prediction in parts of Africa, several studies done in the region have shown that many local communities have a lot of confidence in forecasts made from "star" and moon watching. For example, in Malawi, Zambia and Zimbabwe, when the moon crescent faces upwards it signifies retaining water which means no rain but when facing downwards it signifies releasing water from the skies in the next three days (Zuma-Netshiukhwi *et al*., 2013, Joshua *et al*., 2011, Mugabe *et al.,* 2010, Shoko & Shoko, 2013). When the moon presents a clear halo, good rains are received in South Africa (Zuma-Netshiukhwi *et al*., 2013) while the new moon indicates erratic rainfall in some south-eastern African countries-Malawi, Tanzania, Zambia and Zimbabwe (Joshua *et al.*, 2011, Kijazi *et al*., 2012, Mugabe *et al*., 2010, Shoko & Shoko, 2013; Risiro *et al*., 2012).

In South Africa, for instance, a similar appearance as is the case with the southern-eastern countries, has the same interpretation (Zuma-Netshiukhwi *et al., 2013*). However, the interpretation goes a little further: There are better chances of rainfall with the new moon unlike with the full moon. If a little rain is received during the new moon, a dry period follows, however, good rains at the new moon phase signifies wetness in the following month. During the waxing of the moon, farmers normally plant vegetables and flowers and transplant seedlings, while during waning of the moon, potatoes, sweet potatoes, groundnuts, etc are planted (O'mahony, 2006; Stigter *et. al*., 2012). There are many other techniques of using "star" patterns and relative movements to predict rainfall onset, to forecast wet days or dry days and to determine rainfall cessation dates (Stigter *et. al*., 2012; Crawford, 1989).

In Zimbabwe, when the moon evolves in shape, size and brightness, people take notice and associated weather or climate conditions are also noted. A very bright Moon indicates an approach of the winter season with no rain. The quarter moon or its absence during the summer indicates some rains falling within a very short time (Risiro*,* 2012). In general, the astronomical features observed are used to forecast weather conditions especially the onset within a period of about 14 days in this area.

In an area in northern Tanzania (Chengula and Nyambo, 2016), full moon signifies no rain. When its size is half and its horns point up, it signifies little or no rains. But when it is half size and the horns point either east or west, it indicates onset of rains. When a solar eclipse occurs, it is indicative of rainfall onset with a combination of other factors. It is surprising to note that 49% of farmers here say the IK forecasts are more reliable than the science-based forecasts with 23% of the farmers saying they are not reliable in this area. In a separate study in a

different part of northern Tanzania (Mahoo *et al*., 2015), an almost similar situation was noticed where 56% of farmers relied on IK forecasts more than scientific forecasts. A comparison made from a forecast made by IK forecasters and another forecast by Tanzania Meteorological Agency (TMA) of the rain season March-April-May (MAM) 2012 found out that the IK forecasts were more reliable.

Mahoo *et al*., 2015 also noted that when the Moon is surrounded with heavy clouds then it signifies a good rainfall season while a yellowish ring around it indicates onset for the two rainfall seasons. A slanted position of the moon crescent means a bad season, its circular shape indicates rainfall onset, while red moon and the white moon are indicative of onset of the *vuli* and *masika* rains respectively. At the coast of Tanzania, the same interpretation was collaborated by Fishermen who added that when the moon observed as thin and bright, and a small group of blinking stars appears, it indicates stormy weather in few days' time (Mwanahija*,* 2016). Mwiturubani further adds that misty sign on the Moon crescent as the year begins indicates adequate rainfall all the year-round, while misty sign in other times indicates rainfall onset.

In the Mwiturubani (2015) study in South Africa, one observation was noted, that is, the use of unconventional phases of the moon against what is observed elsewhere. Observation of the moon is done at two of its stages of evolution; increasing moon; and decreasing moon which are used to indicate certain associated weather conditions. When the mist is observed on the crescent moon on western evening sky (increasing moon or approaching Full Moon) it indicates that rainfall onset is possible within two weeks. Similarly, the misty sign on the crescent moon on the eastern morning sky (approaching New Moon) indicates rainfall occurrence before New Moon (increasing moon) (Mwiturubani, 2015).

One of the most interesting outcomes of the study is that the characteristic and nature of the crescent moon as the year begins can be used to determine the climate conditions the following year. For example, if the crescent moon (both decreasing and increasing) with misty signs in January indicates a wet year in the beginning. Alternatively, if the crescent moon is clear, drought will dominate the year that begins (Mwiturubani, 2015).

In Uganda, the use of the moon to forecast is not very frequently mentioned but is well known indicator among some communities. In those communities that practise moon sighting, when some sight a New moon that is red without a lining or the Moon appears bright or appears dark, then that indicates the onset of a dry season. However, when Moon appears white or grey or

bright and dark on one side with a visible ring then that indicates the onset of the rainy season (Okonya *et al*., 2013).

Farther from the region, in Zimbabwe, Full moon to New moon periods indicate rains expected to "clean" the new moon and if there are cloudy conditions up to half-size of the moon then a dry spell is to follow in the next 3 weeks. In most of the cases, people here observe that during the rain season, the new moon is associated with a wet condition. Whenever the new moon is observed, usually in the periods between the months of December and January, and no rains yet, then a prolonged dry spell may follow (Offat *et al*., 2015).

From most locations, in making weather forecasts and climate predictions, one notices that the Full Moon and New Moon phases are adversely mentioned with the exception of some parts of Tanzania where the periods approaching or receding from the key phases of the moon are used. In most cases, they aren't used independently but with other weather conditions or stars configurations.

2.4 The Use of Planets in Indigenous Rainfall Forecasting

In most of East Africa, the "star" constellation characteristics is as important an indicator as the moon phases and the "star" movement and patterns are associated with specific weather conditions from one place to another. The observations made and interpretations derived may differ from one case to another due to the differences in geographical uniqueness of the location, the local weather systems and even the people involved.

However, there are some observations that generate almost the same interpretation across many areas of Africa. For example, in vast areas of Botswana, Malawi, Swaziland, Zambia, Zimbabwe and South Africa, when a certain "stars" group has an eastward movement in clear skies, then rain falls in 3 days' time (Mogotsi *et al.,* 2011; Joshua *et al.,* 2011; Mugabe *et al*., 2010; Shoko & Shoko, 2013; Zuma-Netshiukhwi *et al*., 2013; Dube & Musi, 2002).

In a similar extended study in Zimbabwe (Risiro*,* 2012), the presence of certain "stars" in the sky is used frequently to determine the performance of the rain seasons. The people in Zimbabwe indicate that the *milky* way changes in harmony with the seasons. The *milky* way is normally almost at the centre of the sky in southern summer but shifts to the north in northern summer. Observations of a group of six "stars" in the western sky in winter season is used to forecast the onset of the season. This group of "stars", sometimes six, four, two or even single

depending on what area one come from, is what is normally observed and used by many traditional forecasters in Africa.

At the coast of Tanzania, if, an assembly of about ten small blinking "stars" in a group are observed it indicates rainfall associated with strong wind in the following few hours or days (Mwanahija, 2016). Further, during another study in northern Tanzania (Mwiturubani, 2015), noted that when "stars" congregate over the western sky, rainfall onset is likely to occur within the following two weeks, however, if it is in the eastern sky, it indicates cessation of the rainfall season. The observations are mainly done in the middle of the night.

Musembi and Cheruiyot (2016), conducted a study in south eastern Kenya where the only important astronomical observation involved the constellation of the "stars". They noted that there is a cluster of seven "stars" that is normally monitored. The cluster is always in the sky and is said to appear conspicuously with increasing lateness like does the moon. Around October, it is seen high up in the sky at 9 pm and its position continues to change with time. By early November, it is located at the sunrise horizon position when observed at 7 pm. When the cluster reaches this position, the "short rains" are expected to start within a week.

In western Kenya, a team of researchers (Ogallo *et al*., 2010) collected some astronomical observational data that gave them an insight into how certain night sightings in the sky are used for prediction. Information gathered from the locals showed three main types of "stars" used which seem to capture the attention of the researchers. The three are the *ininini* (signifying small stars), *Eyasulwe* and the *Obwangala* (signifying a bright "star"). They went ahead to explain that when the *Obwangala* appears in the sky in the early part of the night during the period, February-March, it implies rains will not be heavy in the MAM season while the appearance of *Eyasulwe* as it moves eastwards, in the period August-September, heavy rains are expected during the OND season. However, a dry condition is likely in OND when the *ininini* moves eastwards in the period July–August.

In southern Ethiopia and vast areas of northern Kenya, the study by Luseno *et al*., (2002) on the forecasting system by locals there, gave interesting accounts of how the forecast is generated and interpreted. The forecasting of weather events are based on the orientation and configuration of "stars" observable in the night sky a practice which is rather widespread among communities in southern Ethiopia and are known to use the "stars" to forecast rainfall and drought amongst other aspect of pastoral lives. Reading the "stars" is done once in the early night sky and again at midnight. Luseno *et al*., (2002) noted that in some situations, some

"stars" are read in conjunction with the position of the moon and the observations normally focus on four types of "star" group configuration used in forecasting in this region.

This comprehensive report has divided the "stars" into groups for convenience in forecasting. First group of "stars" has four stars in number, distinct, large and with a dazzling twinkle. These stars run across the southern hemisphere from east to west and are used for only climate prediction and weather forecasting in cases where other key stars do not appear. In addition, the brightness of the "stars" would indicate heavy rains for both MAM and OND rains, while dullness would indicate the contrary. The second group involves seven "stars" traversing the northern hemisphere westwards. A third group also consists of a small seven-star cluster in the sky in the middle hemisphere. When observed, it indicates very good rains in MAM season expected to begin in less than 2 weeks. However, the fourth group of "stars" is not used independently to predict, but also includes the movement of the moon as well. Each "star" is associated with a specific prediction (Luseno *et al*., 2002).

But what attracts our attention in the report by *Luseno* is the narrative of "lone stars" movements and their association with the moon as they seem to draw a lot of interest in the forecasters. For example, in a certain "star" configuration that consists of two "stars" observed, with the moon in the neighbourhood, and if clouds are spotted the following morning on the mountain tops in the area, this is an indication of a good rainy season. If hazy conditions appear that morning, chances of having rain that season are reduced (Luseno *et al*., 2002). The IK observations show that if one particularly large "star" is markedly bright near the moon, rain is expected with a delayed onset for that season.

Our focus is further drawn to another "lone star" normally viewed as the Morning "star". It is large in size but doesn't twinkle. If this "star" is sighted on the eastern horizon in the morning and this continues on for 5 to 6 months, both MAM and OND seasons are likely to have good rainfall. If it descends in the western horizon and reappears in the eastern horizon in less than 30 days, then, the coming season is expected to be good and if in less than 70 days, then the coming season is likely to be dry. If this "star" descends while the season is going on, then it has no effect on the amount of rain being received. If the "star" descends when the conditions are dry, dusty and windy, then the following rainy season may be dry (Luseno *et al*., 2002).

Whereas, the "stars" configurations seem to have a complicated system of interpretation, however, it apparently works much better and with more detailed information than the moon phases. While the science-based forecasters may give the moon a little more attention in matters

of atmospheric and oceanic influences, the use of the "star" behaviour by the traditional forecasters, which refers to the motions of the visible planets in the solar system, cannot be wished away. It is for this reason that this study will include the "stars" (planets) behaviour in its analysis.

2.5 The "Stars" Observed in Indigenous Forecasting and Associated Planets

In the previous sections, we dwelt much on what was observed in the skies in different seasons and times of the year. We also noticed that some IK weather and climate forecasters use some observed groups of "stars" to indicate the coming and the performance of certain seasons in their regions. Sometimes this is done in conjunction with the moon phases or (and) the unique attributes of the moon like shape, orientation, colour and brightness at certain times of the night.

In this sub-section, we attempt to explain what these forecasters observe with brief discussions on the celestial bodies observed. However, going deep into astronomy may not be necessary at this point as this is not the central theme of this study. Here and in subsequent sections, we delve deep into the subject where necessary for us to understand more especially where linkages and connections between weather / climate observations and the astronomical observations show a significant relation. It should be noted that this subject can be quite controversial and we wish to be as much objective as possible.

It is a well-known fact that the Earth and everything we see in the sky is moving. The stars in the constellations appear to be in the same place but they are not stationary and this is because they are far away so that their position in relation to each other does not seem to change. The planets, some of which appear as "stars" at night, are nearer and their movements are more conspicuous. The earth's journey around the Sun makes the constellations to travel round the celestial sphere once in a year. This is because each constellation is visible at different times of the year- some only in Boreal summer, some in Austral summer and others during or near the equinoxes (Muirden, 2005). That is why the IK forecasters are able to tell when the seasons are coming in or going away by looking at groups of 5 to 10 "stars" in the sky.

Nonetheless, some single "stars" observed do not seem to follow any season and move either singularly or as pairs and appear brighter than the rest. These "stars" are mainly the planets of the solar system, which are not real stars but celestial bodies that reflect light from the Sun. The two brightest "stars" of the night are Venus and Jupiter. Other planets that are visible to our naked eye are Mars, Saturn, Uranus and Mercury. One has to struggle to see the rest with

a naked eye or not see anything at all. While Jupiter, Saturn and Mars can appear throughout most the night when they are in opposition phase, Venus and Mercury appear for a short time as either evening or morning "stars" (Muirden, 2005). The behaviour of these planets as "stars" is the most dramatic of all bodies in the celestial scenery to the forecasters and their observations seem to give them some necessary assistance to forecast some weather or climate events.

2.6 Atmospheric Tides, Astronomical Cycles and Meteorological Variations

For a long time, attempts have been made by scientists to relate astronomical cycles with meteorological and geophysical variations, sunspot numbers, Length of Day (LOD), electromagnetic energy, solar system barycentre, atmospheric and oceanic tides and the gravitational forces by the planets (Wilson, 2008; Scafetta ,2010; Hung 2007, Goulter, 2003; Lindzen, 1967; Ivanov, 2002). Some scientists have been able to establish that variations in weather and climate are largely due to factors and influences that are of periodic or cyclic nature and that many are astronomical related probably emanating from influences of the Moon and the Sun. Other factors and influences may include modulation of solar irradiance and the evolution of the atmospheric and oceanic tides by the combined lunar and planetary motion. These influences are due to combinations of higher harmonics of the frequencies of revolution of the planets and the Earth around the Sun and the lunar orbital motion around the Earth (Vladimir, 2002).

For example, Li *et al*., (2011) presented an analysis of variations of the earth's length of day (LOD) and compared it with the geopotential heights and lunar phase. The analysis revealed that there was a strong correlation between the parameters that indicated an important relationship between astronomical and meteorological events. It was found that there is a 27.3-day and 13.6-day zonal oscillation in the atmosphere after a lunar phase change signifying the presence of a strong atmospheric tide. During each complete lunar cycle there is an approximate alternating change of 6.8-day-decrease followed by a 6.8-day-increase in U-wind, angular momentum and LOD.

Further to this, some scientists have expressed strong evidence that the astronomical forcings may be modulating LOD by presenting a 60-year cycle that is used to predict a 60-year temperature cycle (Klyashtorin, 2001; Klyashtorin and Lyubushin, 2007; Mazzarella, 2007, 2008). They also noted that change in LOD is understood to influence ocean oscillations such

as the Atlantic Multi-Decadal oscillation (AMO) and Pacific Decadal Oscillation (PDO), therefore, indicating that they are astronomically driven (Scafetta, 2010).

With the evidence coming out in the recent past, Scafetta, (2010), proposed an empirical model with a specific set of astronomic harmonics at different time scales that can simulate observed climatic variations and oscillations. The proposed empirical model performed much better than the GCMs by hindcasting observed meteorological parameters during the period 1850-2012. It was found that slightly more than half of the warming observed at various times since 1850, was likely induced by astronomical forcings with harmonic motions that are not yet factored-into the GCMs. The proposal is outlined in several papers (Scafetta, 2010, 2012a, b, c) in which it is indicated that the climate system is oscillatory and that these behaviours are synchronous with key astronomical oscillations.

Reference can also be made to studies by Wilson, (2008) and Hung, (2007) and their description of a Spin-Orbit oscillations of the planets and coupling between them and how this coupling exerts an alternating gravitational force that results in drag and acceleration on the Sun as they orbit between one conjunction phase to another. The acceleration is created as the inner planet approaches the outer planet and drag as it travels away from the outer planet creating an acceleration-drag cycle that is responsible for influencing the solar cycle.

Some studies (e.g. Wilson *et al*.,2008; Hung, 2007) have suggested that the variation of solar activities may be driven by the coupling mechanisms and the atmospheric tides which involves inertial motion of the Sun as a result of the shifting of the Centre of Mass of the Solar System (CMSS). Then, this shift, which is often chaotic, would influence the terrestrial climate by means of several and complicated mechanisms and feedbacks (Ivanka*,* 2000; Idso and Singer, 2009). This comes out well when you consider large solar flare occurrences which correspond with the alignment of Venus, Earth and Jupiter and the 11-year Schwabe solar cycle (Hung, 2007; Scafetta, 2010)

Further, it was shown that an analysis of solar flare activity and sunspot numbers confirms a relation between the solar activity and the planetary oscillations which is rather complex. Most of the largest known solar flares were observed to start when one or more planets with the highest influences (e.g. Venus, Earth, and Jupiter) were in conjunction or opposition sides. This was consistent with a sunspot cycle with periods that oscillate between 10 and 12 years. (Wilson, 2008; Scafetta, 2010; Hung, 2007)

The nearly exact forcing of the earth's atmosphere by the gravitational attraction of the moon received considerable attention last century, principally by Chapman (1918) and Eddington (1922), with a successful determination of the lunar semi-diurnal pressure tide L_2 in middle latitudes (Goulter, 2005). They theorised that the large-scale atmospheric oscillations are as a result of;

(a) the gravitational forces due to the motions of moon and sun, and

(b) the thermal forces due to the sun's heating.

The tides generated here signify oscillations generated by gravitational forces, *S(p)* or thermal forces *S(T)*; and Lunar gravitational forces, *L(p).* Such variations can be analysed and resolved into their harmonic components, with amplitudes S_n, L_n phases λ_n, σ_n and harmonic coefficients A_n, B_n, a_n, b_n so that; $S(p) = \sum S_n$, $L(p) = \sum L_n$

$$S_n = s_n \sin(nt + \sigma_n) = A_n \cos nt + B_n \sin nt \,, \tag{1}$$

$$L_n = l_n \sin(n\tau + \lambda_n) = a_n \cos n\tau + b_n \sin n\tau \,, \tag{2}$$

From equation (1) and (2), $A_n = s_n \sin \sigma_n$, $B_n = s_n \cos \sigma_n$, $a_n = l_n \sin \lambda_n$, $b_n = l_n \cos \lambda_n$. n is an integer usually $n = 1, 2, 3, 4$, for a reasonable representation for equation (1). Here, *t* and *τ* denote respectively mean solar time and mean lunar time. In equation (2) the main harmonic component is the semidiurnal one, $n = 2$. (Lindzen, 1967)

Goulter (2005) has gone further to express the tidal oscillations, (using pressure) as a sinusoidal variation, amplitude l_2, phase λ, and period τ∗, where τ∗ is the period in mean local lunar time of the lunar semi-diurnal oscillation. It may be written as the sum of mean local lunar Greenwich time τ and east longitude *θ*. Thus,

$$L_2(p) = l_2 \sin(2\tau + \lambda_2) = a_2 \cos 2\tau^* + b_2 \sin n\tau^* \,,$$

Where, $a_2 = l_2 \sin \lambda_2$, $b_2 = l_2 \cos \lambda_2$, $\tau* = \tau + \theta$

Then, $L_2(p) = l_2 [\cos 2\tau \cdot \sin(\lambda_2 + 2\theta) + \sin 2\tau \cdot \cos(\lambda_2 + 2\theta)]$

The l_2 and λ_2 vary geographically; they are the observationally determined quantities, which show the dependence of the wave on the geographic features of a place (Goulter, 2003).

All studies in this study have made attempts to show that the climate variations are influenced by a set of complex oscillatory motions as a result of multiple astronomical mechanisms. Indeed, the planets motions cause the solar system to oscillate at frequencies consistent with the orbital periods of the planets. The internal physical processes of the Earth and the Sun synchronize to the planetary oscillations although actual mechanisms that explain the observed climate oscillations are still widely unknown (Scafetta, 2010).

Finally, when the issue of meteorological and astronomical oscillations is mentioned, Milankovitch (1941) cycles theory always comes up. A widely accepted 1922 theory states that glacial cycles are controlled by the amount of radiation reaching the Earth's surface at about 65^{o} N around the Summer Solstice when sunshine melts glaciers. The amount of radiation at different latitudes in different seasons varies due to changes in three of the Earth's orbital parameters: 1) precession of the Earth's axis, 2) Earth's axial tilt and 3) Eccentricity of the Earth's orbit. He hypothesized that the combination of the cyclic variation of the orbital parameter have caused major changes to the earth's climate which includes ice ages. Though he did his work in the 1920s, Milankovitch's theories weren't proven until the 1970s and since then have gradually gained prominence in the recent times.

2.7 Determination of Rainfall Extremes in the Region

In the early 1960s, Brandley *et al*, (1962), Brier and Bradley, (1964) got an outstanding finding that extreme precipitation events in the US occurred less frequently days before full moon, and more frequently days later. The study carried out statistical analysis showing that the lunar-precipitation relationship was highly likely; they demonstrated that a 'lunar signal' was present in both total rainfall and extreme rainfall amounts. For a long time after, the same relationship has been simulated in other areas with some success (Keeling and Whorp, 1997; Keeling and Whorp, 2000).

Studies done with a focus on extreme rainfall in East Africa which is as a result of lunar or celestial motions is quite difficult to get. But general extreme rainfall studies in the region have been on the rise and a number of authors have been coming up with new extreme climate indices. However, one particular study, Gachari *et al.*, (2013), there was an attempt to relate rainfall extremes in Kenya to some lunar geometrical and astronomical variables and hence come up with some linear regression models. The models they developed suggested that the 1984 droughts in the region and others were largely due to a natural variability. They went on to state that the rainfall pattern could be estimated from some independent variables based on

solar and lunar geometry in a rainfall distribution model. They got a correlation coefficient greater than 0.7 between the model estimate and the variables which was sufficiently good.

It has been shown in various studies locally that increase or decrease in extremes may result when the mean, the variance or both the mean and variance of a distribution change. The modifications of rainfall may result in the changes in intensity and frequency of these events (IPCC, 2013). Rainfall indices in the region have been used by various researchers to determine the probability of rainfall occurrences. There are two approaches in generating the indices of extreme rainfall events; the first method is through the use of percentile-based thresholds while the second method is through the use of fixed thresholds. These approaches are suitable for assessing moderate extremes which usually occur a few times every year. The others are methods that model the occurrence of the extreme events at the tail end of the distribution, e.g., Generalized Extreme Value (GEV) and Generalized Pareto (GP) distributions.

Most studies have utilized the WMO recognized climate indices for ease of comparison while others have utilized statistical methods that rely on extreme value distributions to model the extremes and their return levels. These indices were developed by the Climate Variability (CCl/CLIVAR) Working Group on Climate Change Detection to create uniformity globally when analysing extreme climate events (Alexander*, et al.,* 2006).

The study on extremes in precipitation over the region has been attempted by several authors. One of the recent studies was done by Omondi *et al.,* (2018) and involved observed data running over the period 1971 to 2006 in East Africa. Another author, Shongwe *et al*., (2011) used the method of peaks over threshold (POT) and General Pareto distribution (GP) to analyse the rainfall extremes and their return periods over East Africa. Ngailo *et al*., (2015), has done modelling of extreme rainfall using the General Extreme Value (GEV) Theory for Tanzania.

2.7.1 *Extreme Value Modelling*

The Extreme Value Modelling aims at approximating maximum or minimum meteorological data that corresponds to the occurrence of the natural disaster or generally estimate a value that is more extreme than any that has been already observed (Coles, 2001; Beirlant, 2004). That leads us to the determination of return levels and return periods of the extreme rainfall and this forms the very beginning of an extreme value problem that can be solved if we assume GEV or GP distributions of the maximum values of rainfall dataset. A return level set at a threshold of RR mm with a return period, of T years, has a probability of exceedance given as $p[X >$

RR]. The return period and the probability of exceedance are related as follows; $T = \frac{1}{RR}$. For example, if $p = 0.05$, then the return period is $T = 20$ years.

Two interpretations of a return level, RR mm with a return period of T years are summarised below:

(i) T years is the waiting time for an event to recur (or the average waiting time until next occurrence of the same event); and
(ii) Number of events occurring within a T-year time period.

The statistical theory developed to deal with these problems and this type of data is known as Extreme Value Theory (MacDonald *et al*., 1992). The choice of what method to use depends on several factors; the shape, mean and the standard deviation of the maximum rainfall values. The models in the following sub-sections 2.7.2 to 2.7.4 have been used to model extreme rainfall in East Africa.

2.7.2 *Percentile Based Thresholds*

There are two approaches in generating the extreme indices; the first method is through the use of percentile-based thresholds while the second method is through the use of fixed thresholds. These approaches are suitable for assessing moderate extremes which usually occur a few times every year. This method has been used by Kuya (2016) and Omondi *et al.* (2018) and has gone on to show that Return levels are used in many studies due to their simplicity in applying and interpreting them.

Kuya, (2016) and Omondi *et al.,* (2018) used the following indices which are given in ID codes as; CCD (Consecutive dry days), CWD (Consecutive wet days), R95p (Moderate / very wet days), R99p (Extremely wet days) and PRCPTOT (daily precipitation amount). These climate Indices are also given and explained in Zhang and Yang, (2004) and because of their simplicity and ease of use they have become quite valuable. These climate indices are based on the full set of 27 descriptive weather and climate indices on extremes as defined by the Joint CCl/CLIVAR/JCOMM Expert Team on Climate Change Detection and Indices (ETCCDI) (Alexander et al., 2006).

Below are some of the relevant indices;

For the index CCD, RR_{ij} is the daily precipitation amount on day i in period j, where a count of the largest number of consecutive days satisfies the condition $RR_{ij} < 1$ mm

For the index CDW, RR_{ij} is the daily precipitation amount on day i in period j, where a count of the largest number of consecutive days satisfies the condition $RR_{ij} \geq 1$ mm

For the index R95p, RR_{wj} is the daily precipitation amount on a wet day w ($RR \geq 1.0$ mm) in period i and $RR_{wn}95$ is the 95th percentile of precipitation on wet days in the 1961-1990 period. If W represents the number of wet days in the period, then:

$$R95p_j = \sum_{W=1}^{W} RR_{Wj} \tag{3}$$

In Equation (3), $RR_{wj} > RR_{wn}95$

For the index R99p, RR_{wj} is the daily precipitation amount on a wet day w ($RR \geq 1.0$ mm) in the period j . $RR_{wn}99$ is the 99th percentile of precipitation on wet days in the period of study. If W represents the number of wet days in the period, then:

$$R99p_j = \sum_{W=1}^{W} RR_{Wj} \tag{4}$$

In Equation (4), $RR_{wj} > RR_{wn}99$

And finally, with the index PRCTOT, RR_{ij} is the daily precipitation amount on day i in period j. If i represents the number of days in j, then the index is given in Equation (5);

$$\text{PRCTOT}_j = \sum_{i=1}^{I} RR_{ij} \tag{5}$$

2.7.3 *Generalized Extreme Value Distributions*

The Generalized Extreme Value (GEV) distribution can be used in dealing with extreme elements like winds, precipitation (floods and droughts), temperatures (maximum and minimum) and other extremes emanating from the effects of Climate Change. It can be expressed in a set of three extreme value distributions; the *Weibull*, *Gumbel* and *Frechet* distributions. This model is appropriate when the maximum observations of each period with

a predefined and fixed length are gathered from a large number of identically and independently distributed variables (Coles, 2001).

The cumulative distribution function of these three distributions can be summarized by the GEV as follows;

$$G(RR, \xi, \sigma, \mu) = \begin{cases} exp - \left(1 + \xi\left(\frac{RR - \mu}{\sigma}\right)\right)^{\frac{-1}{\xi}}, \xi \neq 0 \\ exp\left(-exp\left(\frac{RR - \mu}{\sigma}\right)\right), \quad \xi = 0 \end{cases} \tag{6}$$

In Equation (6), RR is the extreme value, μ is a location parameter; σ is a scale parameter; and ξ is a shape parameter. For ξ > 0, we get the Frechet distribution, ξ = 0, the Gumbel distribution and ξ < 0 the Weibull distribution.

After the best probability function for the given data has been determined, the return levels of extreme rainfall can be determined. The T year return level, say RR_T, is the level exceeded on average only once in T years (RR_T) $= 1 - \frac{1}{T}$. (Ender and Ma, 2014 given in Ngailo *et al.,* 2016). The return level for GEV with return period $\frac{1}{p}$ is obtained by use of Equation (7);

$$Z_p = \begin{cases} u - \frac{\sigma}{\xi}\left(1 - \left(-\log(1-p)\right)^{\xi}\right), & \xi \neq 0 \\ u - \sigma\log\left(1 - \left(-\log(1-p)\right)\right), & \xi = 0 \end{cases} \tag{7}$$

2.7.4 *The Generalised Pareto (GP) Distribution*

The generalized Pareto distribution has a relatively simple statistical procedure and it is useful for modelling events that exceed a specified lower value at which the density function has a maximum. GP can be used with daily rainfall values above an extreme threshold that is relatively lower than that used in GEV (Hosking and Wallis 1987; Davison and Smith, 1990). Modelling the rainfall extremes with GP enables a more effective usage of extreme value information than that given by an analysis of annual maxima data, as used in GEV. While GP deals with a number of extreme values, GEV eliminates many extreme events that were not counted as the largest annual value.

The probability that a value *y* exceeds a given threshold *RR,* which is the distribution function of extreme values of *X* over *RR* is given in Equation (8);

$$F_{RR}(y) = Pr(X - RR \leq y | X > RR) = \frac{F(RR + y) - F(RR)}{1 - F(RR)} \quad (8)$$

*w*here $y = X - RR$. It has been shown in earlier studies that the distribution $F_{RR}(y)$ converges to GP when the threshold is sufficiently high (Balkema and De Haan 1974). Once the parameters are determined the cumulative distribution function for the GPD can be estimated in Equation (9):

$$GP(RR, \xi, \sigma, \mu) = \begin{cases} 1 - \left(1 + \xi\left(\frac{RR - \mu}{\sigma}\right)\right)^{\frac{-1}{\xi}}, \xi \neq 0 \\ \left(1 - exp\left(\frac{RR - \mu}{\sigma}\right)\right), \quad \xi = 0 \end{cases} \quad (9)$$

For this model, the return level is explained by RR_m that defines the extreme level that is exceeded on average once every *m* observations and is given in Equation (10),

$$RR_m = \begin{cases} RR + \frac{\sigma}{\xi}(\zeta_{RR} - 1), & \xi \neq 0 \\ RR + \sigma \log(m\zeta_{RR}), & \xi = 0 \end{cases} \quad (10)$$

The main weakness of these methods is that they begin by discarding all of the data that are non-extreme events, and hence reduce a large dataset into a small dataset. Extreme value methods become more appropriate if the full dataset, including non-extreme values, is reasonably large. They are traditionally used in areas where large amounts of data are routinely collected and hence may not be useful for our application in this study as our datasets are not large enough. GP is used in the study by Shongwe *et al*., (2010), to represent the distribution of observed and simulated extreme seasonal precipitation rates and return levels in East Africa for both OND and MAM seasons.

CHAPTER THREE: THEORETICAL FRAMEWORK

This study is undertaken to identify the extrinsic drivers of rainfall in the East Africa region by considering the astronomical influences. The study focuses on the motion geometry of the moon and the planets. This is intended for a more in-depth understanding of the subject by providing basic derivations of the angle of elongations and the instantaneous distances of the planets from the Earth.

3.1 Defining the Key Phases of the Bodies

The phase of the celestial body is defined in this study as a key point of inflection, the maximum or the minimum distance from the Earth or the maximum or minimum angle of elongation of the body.

In dealing with the celestial bodies, we will divide them into three, based on unique motions relative to Earth. These are: The Moon, Inferior Planets and Superior planets. Planets refer to Mercury, Venus, Mars, Jupiter, Saturn, Uranus and Neptune. The Inferior planets (with orbits smaller than Earth's orbit) are Venus and Mercury and the Superior planets (with orbits bigger than Earth's orbit) are Mars, Jupiter, Saturn, Uranus and Neptune. The geometry of the moon and the planet's orbital motions is constructed where the angle of elongation of individual planets and distance of the planets from the Earth are estimated. By using the distance of a planet from Earth, gravitational forces can be estimated at any given time during their full cycle.

The gravitational forces of these planets can be correlated and compared to rainfall through regression and the determination of the probability of exceedance during certain phases of the celestial bodies.

3.1.1 *The Motion Geometry Associated With Phases of the Moon*

The Moon exhibits different phases as the relative position of the three bodies -the Sun, Earth and Moon changes, appearing as a full moon when the Sun and the Moon are on opposite sides of the Earth and as a new moon when they are on the same side. The two phases of the moon occur when the Earth, Moon, and Sun lie (approximately) in a single axis. The time taken when

the moon orbits from full moon to full moon (which is referred to as a Lunar month or synodic period) is about 29.53 days (29 days, 12 hours, 44 minutes) on average. This synodic period or month is slightly longer than the period taken to make one full orbit around the Earth with respect to the fixed stars (referred to the sidereal period), which is about 27.32 days. This difference is caused by the fact that the Earth-Moon system is orbiting around the Sun (as the frame of reference) at the same time the Moon is orbiting around the Earth (as the frame of reference) (Gutzwiller, 1998).

Figure 2 shows a simple representation of the motion of the moon around the Earth assuming a perfect circular motion where the effects of eccentricity, precession and other influences from the solar system are disregarded. At point A, the moon is at new moon position and at point B, it is at full moon position. Let f(x) be a function representing a sinusoidal quantity that is proportional to the moon orbital oscillations, then the function can be expressed in a general Fourier series expression, (Equation 11),

$$f_n(x) = \sum_n \{A_n \cos(k_n x + a_n) + B_n \sin(k_n x + a_n)\} \tag{11}$$

In Equation (11), k is the wave number, A_n, B_n represent Amplitude, a_n, b_n signify phase coefficients and x is an independent variable.

By using Figure (2), if we choose the Sun-Earth axis as our reference, then the angle, λ , which is the angle of elongation between this axis and the Moon-Earth axis, varies in the range $0 \leq \lambda \leq 2\pi$ in the following expression, Equation (12) which is a simpler form of Equation (11) where k is equal to *1*,

$$f(\lambda) = A_0 \cos(\lambda + a) + B_0 \sin(\lambda + b) \tag{12}$$

In Equation (12), A_0, B_0 are Maximum Amplitudes, a, b are phase coefficients and λ is the Elongation Angle. Since the moon's motion is assumed to be perfect, the governing equation of the motion, Equation (12), would reduce to a simple cosine wave motion about the Earth-Sun axis represented by just one cosine component given in Equation (13);

$$f(\lambda) = A_0 \cos \lambda = A_0 \cos \frac{\pi}{12} t \tag{13}$$

In Equation (13), t is time and phase shift is equal to zero.

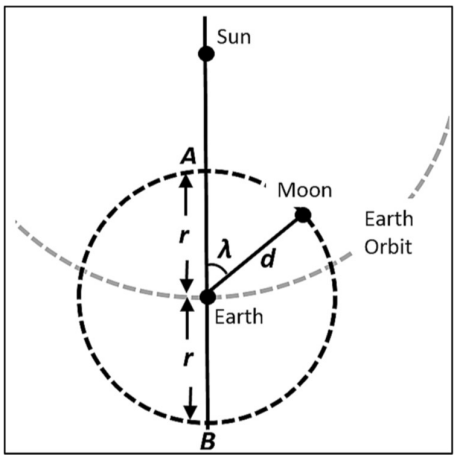

Figure 2 : Simple motion geometry of the moon assuming a perfect circular motion. The construction of this schematic representation is based on concepts from Gutzwiller, 1998

The main idea is to compare two scenarios when one phase is one extreme while another is the opposite extreme. Let the function, $f(\lambda)$ be directed towards the sun. Then at point A, the New Moon phase would be $\lambda = 0, f(\lambda) = A_0$ which is a maximum value of the function. At point B, Full Moon phase would be $\lambda = \pi, f(\lambda) = -A_0$, which is minimum value of the function.

In addition, First Quarter and Second Quarter phases of the moon would be $\lambda = 90$ degrees and $\lambda = 270$ degrees respectively at which point, the function is equal to zero. The distance, d is taken to be a constant.

If we assume that this factor, $f(\lambda)$, is proportional to an unknown rainfall modulating factor due to moon orbital motions, then the two phases, Full Moon and New Moon should possess opposite orbiting properties. This line of thought will form part of the null hypothesis that, the two 'opposing' phases should possess opposite rainfall properties if the moon orbital motions have any effect on rainfall.

3.1.2 *The Motion Geometry Associated with Inferior Planets*

Inferior planets are planets with a smaller orbit than the Earth's orbit. There are only two inferior planets; Mercury and Venus. The most important phases of these planets are the Inferior Conjunction and Superior Conjunction (considered in this study as "opposite" phases as the planet is positioned on opposite sides of the Sun at each of the two phases). Other phases exhibited by the planets are Maximum elongated East and Maximum elongated West; however, these phases are not used in this study.

The inferior planets are unique in that they appear mainly on the sunny side of the Earth. In reference to the Earth-Sun axis, the inferior conjunction occurs when the planet (point B) is between the Earth and the Sun in a single axis and Superior Conjunction occurs when the sun is between Earth and the planet (point A) in a single axis (Figure 3). Figure 3 shows the motions of the inferior planets between these conjunctions. Both conjunctions are at $\lambda = 0^0$. For the purposes of this study, the inclination angle, is taken to be constant.

Determination of the distance of the inferior planets from Earth at any given time is unlike the distances due to orbital motions of the moon, which are fairly regular around the Earth (with the assumptions made earlier), the motions of the inferior planets are a bit complex. Note that, distances are measured from the centre of the planets as the radi of the planets are too small, about 4 orders of magnitude lower than the distances between planets.

We can demonstrate this by deriving the distance of the planet from earth and the angle of inclination with time (by use of Figure 3).

The distance of the inferior planet from Earth at any time, t, is given by use of rules of cosines and given in Equation (14),

$$d^2(t) = r_\psi^2 + r_e^2 - 2r_e r_\psi \cos \propto (\mathrm{t}) \tag{14}$$

$$\propto (t) = \left(\frac{1}{\tau_\psi} - \frac{1}{\tau_e}\right) 2\pi t \tag{15}$$

In Equations (14) and (15), r_ψ is the distance of the inferior planet, ψ, from the Sun, r_e is the distance of Earth, *e*, from the Sun, *d* is the distance of Earth from the planet, λ, Elongation angle of the inferior planet from Earth, τ_ψ, sidereal period of the planet, ψ and $\tau_e$is the sidereal period of the Earth, *e.*

But the Equation (14) can be rearranged so that it has the following form,

$$r_e^2 = r_\psi^2 + d^2 - 2dr_\psi \cos\beta \tag{16}$$

and $\beta = \pi - \propto - \lambda$, so that,

$$r_e^2 = r_\psi^2 + d^2 - 2dr_\psi \cos(\pi - \propto - \lambda) \tag{17}$$

Making the angle of elongation the subject, therefore,

$$\cos(\pi - \propto - \lambda) = \frac{r_\psi^2 + d^2 - r_e^2}{2dr_\psi}$$

$$\lambda = \pi - \propto - \cos^{-1}\left(\frac{r_\psi^2 + d^2 - r_e^2}{2dr_\psi}\right)$$

and hence, on day *i* or Month *i*, Equation (17) becomes Equation (18),

$$\lambda(i) = \pi - \left(\frac{1}{\tau_\psi} - \frac{1}{\tau_e}\right)2\pi i - \cos^{-1}\left(\frac{r_\psi^2 + d_i^2 - r_e^2}{2d_i r_\psi}\right) \quad (18)$$

During both the inferior and superior conjunctions of the inferior planet, $\lambda = 0^0$ and $\propto = 0$ so that the Equation (18) becomes Equation (19),

$$0 = \pi - \cos^{-1}\left(\frac{r_\psi^2 + d^2 - r_e^2}{2dr_\psi}\right) \quad (19)$$

Solving for d in Equation (19), there are two possible solutions, $d = \left|-r_\psi \mp r_e\right|$ which are consistent with the diagram (Figure 3) where *d* has a maximum (at point B) and a minimum (at point A), that is, $d_{min} = r_e - r_\psi$ and $d_{max} = r_e + r_\psi$ respectively.

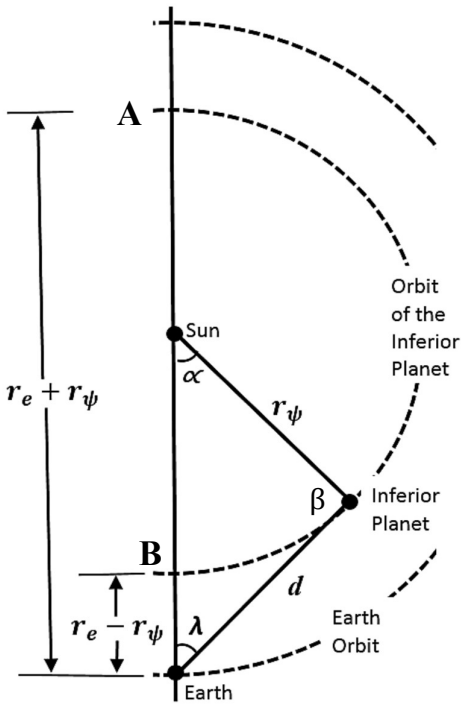

Figure 3: The motion Geometry of the inferior planet and the Earth in relation to the Sun. The construction of this schematic representation is based on concepts from Gutzwiller, 1998 and Wilson, 2013

For Venus, it takes 225 days (synodic Period) to orbit the Sun with reference to the distant stars. However, the full sidereal cycle (from inferior conjunction to inferior conjunction) takes

584 Earth days, about 1.6 Earth years. The sidereal cycle is in reference to observations of the Venus orbital motions from the Earth.

The other phases of the inferior planets are "maximum elongated East" and "maximum elongated west" which represent the maximum angle of elongation to the east and to the west of the Sun-Earth axis respectively. For Venus, both maximum elongated east and maximum elongated west are normally 46^0 (Wilson, 2013). For Mercury, the synodic period is given as 116 days and the maximum elongated angle 28^0. The mass of Venus and Mercury are given as $4.8685\ \text{x}10^{24}kg$ and $3.3022\ \text{x}10^{23}kg$ respectively.

3.1.3 *The Motion Geometry Associated with Superior Planets*

Superior planets are planets with an outer or bigger orbit than the Earth's orbit with both orbits being concentric, that is to say, they share the same centre. There are five superior planets; Mars, Jupiter, Saturn, Uranus and Neptune. The most important phases of these planets are the Superior Conjunction and Opposition (considered in this study as "opposite" phases as the planet is positioned on the opposite sides of the Sun at each of the two phases). Other phases exhibited by the planets are not used.

In reference to the Earth-Sun axis, the Opposition occurs when the Earth is between the planet and the Sun in a single axis and Superior Conjunction occurs when the sun is between Earth and the planet in a single axis. Both the Superior conjunction (λ equals to 0^0) and opposition (λ equals to 180^0) of the planets fall on the same axis (Figure 4). For the purposes of this study, the inclination angle, θ is a constant (Wilson, 2013).

Like the inferior planets, deriving the distance of the planet from earth and the angle of inclination with time follows the same process except that $r_e < r_\psi$ thus,

$$d^2{}_\psi(t) = r_\psi^2 + r_e^2 - 2r_e r_\psi \cos \propto (t) \qquad (20)$$

In Equation (20), the distance, *d* varies sinusoidally and has two solutions at $\propto = 0$ which are consistent with the diagram where *d* has a maximum and a minimum given as, d_{min}equals to $r_\psi - r_e$ and d_{max}equals to $r_\psi + r_e$. The symbol ψ represents a planet.

For Jupiter, which has cycles of one Earth-year and a month, about 398.9 days, i.e. from opposition to opposition or superior conjunction to superior conjunction, there are 11 cycles every 12 years. The planet Mars the smallest of the superior planets' orbits opposition to opposition every 26 months (about 780 days) but should be noted that its orbit is quite eccentric.

For our case in this study, we have assumed that the motion is free of eccentricity and hence circular.

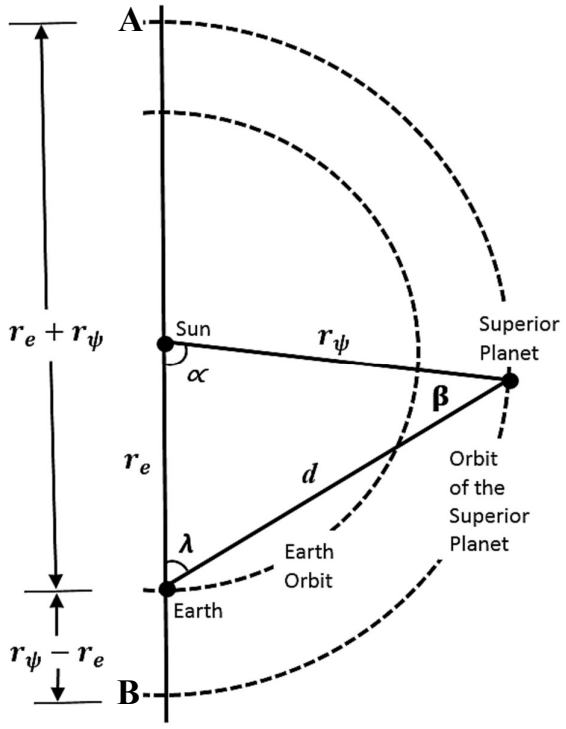

Figure 3(b): The Geometry of the Superior planet and the Earth motions in relation to the Sun. The construction of this Schematic representation is based on concepts from Gutzwiller, 1998 and Wilson, 2013.

The planets Saturn, Uranus and Neptune are farther away; Saturn and Uranus can be observed with a naked eye while Neptune the farthest is only visible through the use of a telescope. The Saturn, Uranus and Neptune times of opposition to opposition are 378 days, 370 days and 368 Earth days respectively.

The masses of Mars, Jupiter, Saturn, Uranus and Neptune are given as; $6.4185 \times 10^{23} kg$, $1.8986 \times 10^{27} kg$, $5.6846 \times 10^{26} kg$, $8.681 \times 10^{25} kg$ and $1.0243 \times 10^{26} kg$ respectively.

3.1.4 *Gravitational Forces and Associated Key Phases*

The gravitational force exerted by individual planet, ψ, on a unit mass of the atmosphere near the equator may be given as;

$$F_\psi(t) = G\frac{M_\psi}{d_\psi^2(t)} \tag{21}$$

$$F_{\psi}(t) = G\frac{M_{\psi}}{r_{\psi}^2 + r_e^2 - 2r_e r_{\psi}\cos \propto (t)} \tag{22}$$

In Equation (21), M_{ψ} is the mass of planet ψ, G is the gravitational constant and F_{ψ} is the gravitational pull on a unit mass of air on day, t, from planet ψ.

The Equations (21) and (22) can be used, to a fair approximation, to determine the relative strengths of the gravitational forces of attraction by different bodies. When a planet is at any of the conjunctions or opposition phase the gravitational force is at either maximum or minimum. The force calculated for the planet at the conjunctions gives maximum $(F_{\psi}[max])$ and minimum $\left(F_{\psi}[min]\right)$ values when the angle of elongation, $\propto$ is equal to 0 or 180 for day t or month t. They values are given in Equations (23) and (24);

$$F_{\psi}[max] = G\frac{M_{\psi}}{\left|r_e - r_{\psi}\right|^2} \tag{23}$$

$$F_{\psi}[min] = G\frac{M_{\psi}}{\left|r_e + r_{\psi}\right|^2} \tag{24}$$

3.3 Limitations of the Study

Our study is based on two main areas of focus-Meteorology and Astronomy. In astronomy, the motions of the planets are based on a number of factors, which, amongst many, may influence the direction of our study. One of the main problems that may be encountered are the influences that may come from perturbing forces from known and unknown sources within or outside the solar system. Although the influences are considered small, this study assumes they do not exist and considering the timeframe of this study, they can be considered in a future study.

Also considered is the effect of the eccentricity or elasticity of the Earth, Moon and the planets orbits. We have assumed the orbits to be perfect circles which in reality is not the case. To a good approximation they can be ignored. Also ignored is the effect of precision and obliquity of the earth's spin-orbit motions.

Studies of this nature require long lengths of data, possibly 100 years or more, however, rainfall data available for the study runs from 1948 to 2017 and therefore investigation will focus on a shorter study period of 1948-2017. However, Astronomy data for this study is available for 150 years.

3.4 Conceptual Framework of the Study

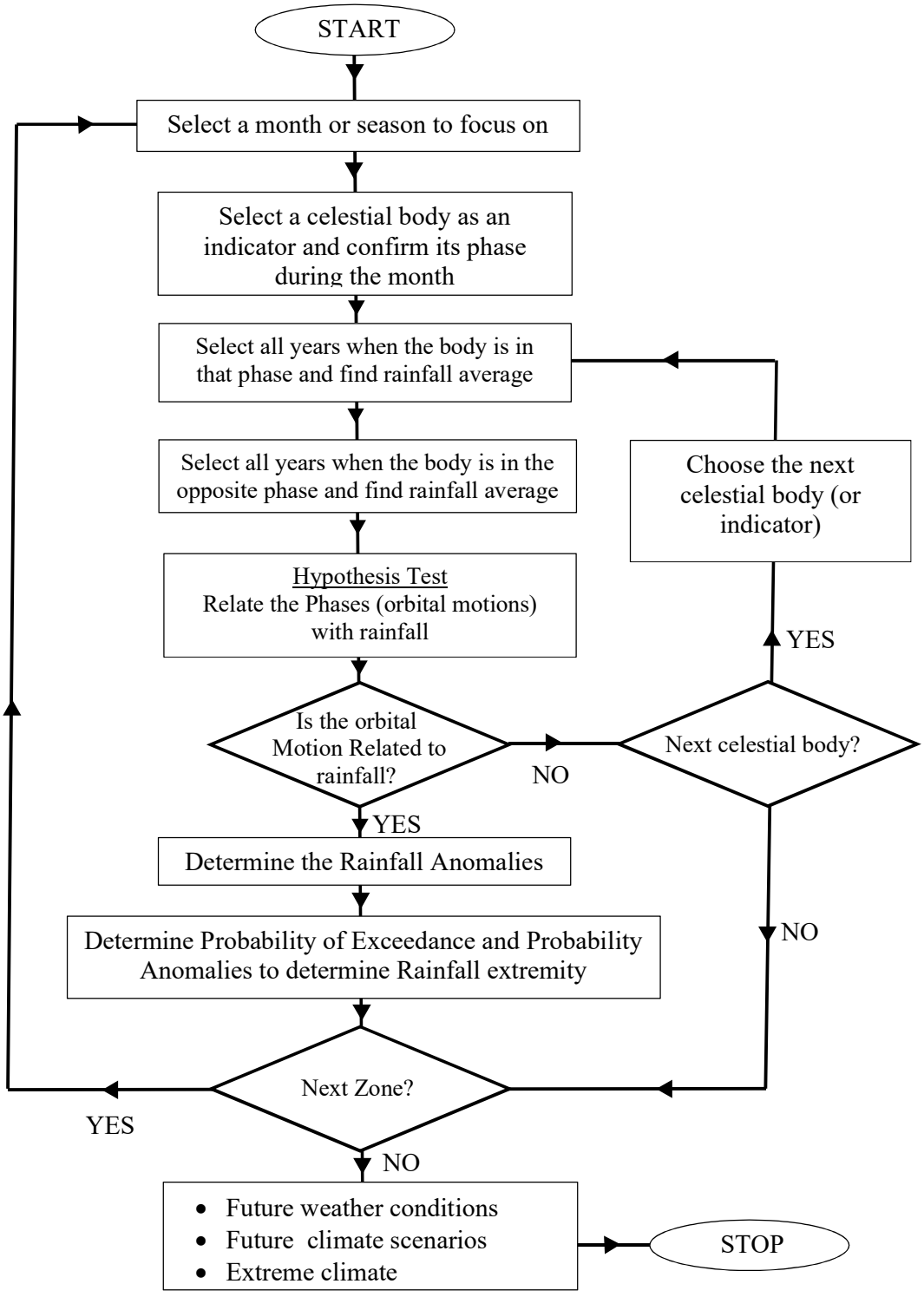

Figure 4 :This framework represents procedures of weather forecast and climate prediction by use of rainfall anomalies and probabilities of occurrence in each zone.

CHAPTER FOUR: DATA AND METHODOLOGY

A brief description of the datasets used, the source of data and the analytical methods applied to meet the objectives of the study are presented.

4.1 Data

4.1.1 *Data Types and Sources*

These datasets were mainly obtained from two sources and are described below;

a) Reanalysed monthly rainfall data for the 12 zones covering the region was obtained as Surface Precipitation Rate (mm/day). The data is an NCEP Reanalysis and was Produced and generated at the NOAA/ESRL PSD at: *http://www.esrl.noaa.gov/psd/data/timeseries/* . Climatology was set at 1981-2010.
b) Astronomical data on dates of the conjunctions and oppositions: The Moon phases and Planetary Ephemeris data has been provided in Moon and Planetary Ephemeris Phases Tables found in *www.Astropixels.com* through calculations by *Fred Espenak*. The calculations done to determine the dates are based on procedures described in Meeus (1998).

The specific sets of both Astronomical and Meteorological data are;

a) Reanalysed monthly rainfall datasets for the Zones I to Zones XII (1948-2017);
b) Moon Phases (Full Moon and New Moon) Dates (1900-2050)
c) Dates of Venus Conjunctions (1900-2050)
d) Dates of Jupiter Conjunctions (1900-2050)
e) Dates of Mars Conjunctions (1900-2050)
f) Dates of Saturn Conjunctions (1900-2050)

4.1.2 *Quality Control*

Data quality control is subjected to daily rainfall to ensure the data consistency within a dataset from a station. There are some substantial inconsistencies present in rainfall datasets due to

rainfall measurements usually made with human mistakes and measurement errors in records from instruments due to various factors. One may also find missing data which is not good for climate analyses. It is therefore necessary to fill-in the missing data before any data is subjected to analysis keeping the percentage of missing data at less than 10% for a station dataset. Again, basic quality control procedures and homogeneity tests are necessary for good quality data. In this study, we have used a simple homogeneity test using the single mass curve, where plotting cumulative values of rainfall records against time is done. A straight line indicates a homogeneous record while a shift in the cumulative line indicates heterogeneity.

4.2 Methodology

4.2.1 *Autocorrelation*

While the astronomical data is smoother in comparison to daily rainfall data, the rainfall data is highly variable and especially the daily rainfall data. It is the desire of this study to test the cyclicity of this data and make important comparisons with the astronomical data. A suitable statistical tool is the Autocorrelation.

Autocorrelation allows close examination of a relationship within an individual variable across a given time-dimension. This, therefore, assists in understanding time series cyclic properties which are useful in this study. Correlograms, and plots of the autocorrelation function subsequently provide descriptive and statistical methods that tell the nature and structure of a deterministic cycle component within the time-series.

Autocorrelation is correlation coefficient of a variable with itself at a given $lag\ k$. At $lag\ =\ 1$, the correlation coefficient determined is the first order correlation of the first N−1 observations $[x_t : t = 1, 2, \ldots, N-1]$ and the next $N-1$ observations $[x_t : t = 2, 3, \ldots, N]$. N is degrees of freedom.

Autocorrelation is given by Equation (25):

$$r_1 = \frac{\sum_{t=1}^{N-1}\left(x_t - \bar{x}_{(1)}\right)\left(x_{t-1} - \bar{x}_{(2)}\right)}{\sqrt{\sum_{t=1}^{N-1}\left(x_t - \bar{x}_{(1)}\right)^2}.\sqrt{\sum_{t=1}^{N-1}\left(x_{t+1} - \bar{x}_{(2)}\right)^2}} \tag{25}$$

In Equation (25), $\bar{x}_{(1)}$is the mean of the first $N-1$ observations and $\bar{x}_{(2)}$ is the mean of the last $N-1$ observations.

For reasonably large N, the difference between $\bar{x}_{(1)}$and $\bar{x}_{(2)}$would be negligible, and r_1 can be approximated by Equation (26),

$$r_1 = \frac{\sum_{t=1}^{N-1}(x_t - \bar{x})(x_{(t+1)} - \bar{x})}{\sum_{t=1}^{N-1}(x_t - \bar{x})^2} \quad (26)$$

In Equation (26),

$$\bar{x} = \frac{1}{N}\sum_{t=1}^{N-1} x_t$$

is the overall mean.

The correlation between observations separated by k time units is given as in Equation (27);

$$r_k = \frac{\sum_{t=1}^{N-k}(x_t - \bar{x})(x_{(t+k)} - \bar{x})}{\sum_{t=1}^{N-k}(x_t - \bar{x})^2} \quad (27)$$

The range of autocorrelation coefficients r_k determined provide decisive information about the internal structure of the time series and a plot of *k* against r_k is used to provide this information.

The standard error can be determined for lag k by use of Equation (28);

$$SE_k = \sqrt{\frac{1}{N}\sum_{t=1}^{k} r_i^2} \quad (28)$$

At lag 0*,* autocorrelation function is always equal to 1. An approximate 95% confidence limit is set for H_0: $r_k = 0$. If no autocorrelation estimate falls outside the limits defined by the confidence levels, with no outliers, we may assume that there is no serial correlation.

4.2.2 *Cross-Correlation*

Cross-correlation is a measure of similarity between two time series. The two, Cross-correlation and autocorrelation are commonly used for measuring the similarity of variables especially for "pattern recognition" and for "cyclicity'. Cross-correlation is the linear correlation coefficient between two time series as a function of time lag between the two series. This is a useful tool in relating meteorological parameters which represent events that are suspected to be related when lagged.

Consider N pairs of observations on two time series x_t and y_t. Cross-covariance function is given in Equations (29) and (30):

$$\gamma_{xy}(k) = \frac{1}{N}\sum_{t=1}^{N-k}(x_t - \bar{x})\left(y_{(t+k)} - \bar{y}\right) \ , For\ k\ =\ 1,2,3,\dots,N-1 \tag{29}$$

$$\gamma_{yx}(k) = \frac{1}{N}\sum_{t=1-k}^{N}(x_t - \bar{x})\left(y_{(t+k)} - \bar{y}\right) \ , For\ k\ =\ -1,-2,-3,\dots,N-1 \tag{30}$$

$\gamma_{xy}(k)$ is the cross-covariance when y_t lags x_t, $\gamma_{yx}(k)$ is the cross-covariance when x_t lags y_t, N is the series length, $\bar{x}$ and $\bar{y}$ are the sample means and k is the lag.

Cross-correlation is the cross-covariance scaled by the variances of the two series;

$$r_{xy}(k) = \frac{\gamma_{yx}(k)}{\sqrt{\gamma_{xx}(0)\gamma_{yy}(0)}} \tag{31}$$

In Equation (31), $\gamma_{xx}(0)$ and $\gamma_{yy}(0)$ are the sample variances of series x_t and y_t.

4.2.3 *Smoothening a Time Series*

Rainfall is a highly erratic variable which requires smoothening to make out clear variations within it. One of the most common methods of smoothening a time series is by using a weighted moving average. A weighted average is an average that has multiplying factors to give different weights to data in different terms in a time series. A weighted moving average (WMA) has ordered weights that decrease in a systematic or arithmetical progression. For example, in a day t, WMA has weight α, the day before which is $t-1$ has a weight $\alpha - 1$, etc…, down to one. The Weighted Moving Average is given by Equation (32);

$$y_t = \frac{\alpha x_t + (\alpha-1)x_{t-1} + (\alpha-2)x_{t-2} + \cdots + 2x_{t-n+2} + x_{t-n+1}}{\alpha + (\alpha+1) + (\alpha+2) + \cdots + 2 + 1} \tag{32}$$

In Equation (32), x_t is the rainfall totals at day t, y_t is the value of the WMA at any day t, and n is the number of days used. The above equation can be modified so that WMA can be obtained for the day in the middle of the rainfall totals being averaged and as a result we get Equation (33);

$$y_t = \frac{x_{t-(k-1)} + \cdots + (k-1)x_{t-1} + kx_t + (k-1)x_{t+1} + \cdots + 2x_{t+(k-2)} + x_{t+(k-1)}}{k + 2\{(k-1) + (k-2) + \cdots + 2 + 1\}} \tag{33}$$

Equation (33), x_t is the rainfall totals at day t, y_t is the value of the WMA at any day t and k is an integral that determines the number of days used for smoothing, which is equal to $(2k+1)$.This is the preferred equation for smoothening monthly totals. (Hunter,1986).

4.2.4 *Detecting Periodicity- Regression on Lagged Values*

Autocorrelation function (ACF) is a procedure for describing the characteristics of a temporal structure of a rainfall time-series (discussed in 4.2.2). We can calculate the coefficients which define the ACF using Equation (34):

$$r_k = \frac{\sum_{t=1}^{N-k}(x_t - \bar{x})\left(x_{(t+k)} - \bar{x}\right)}{\sum_{t=1}^{N-k} T(x_t - \bar{x})^2} \tag{34}$$

The ACF is a standardized version of an Autocovariance, and is defined in Equation (35):

$$\gamma_k = \frac{1}{N}\sum_{t=1}^{N-k}(x_t - \bar{x})(x_{t+k} - \bar{x}) \tag{35}$$

4.2.5 *Detecting Periodicity- Regression on Sinusoids*

If the above methods do not give desired results, it makes sense to use sinusoidal functions that are periodic themselves to describe the time-series variations. This method known as the frequency domain time series analysis employs a combination of sine and cosine functions in a simple form of Fourier series. Since sine and cosine functions are periodic, a squares fit of a time-series with combinations of sine and cosine functions as independent variables can be given as in Equation (36):

$$f(t) = \propto + \sum_{\lambda}(a_\lambda \cos(2\pi t\lambda) + b_\lambda \sin(2\pi t\lambda)) + u_i \tag{36}$$

The advantage of this approach is that one can fit many periodic functions directly using well-understood techniques and can produce statistical tests of the extent to which the different periodic components contribute to an overall series. For periodicity, this method is preferable.

4.2.6.1 *Determination of Rainfall Anomalies and their Variations*

Given a rainfall dataset from a zone or station, where *RR* mm is the observed or reanalysed values, it can be expressed in a matrix form as follows;

$$RR_{ij} = \begin{bmatrix} RR_{11} & RR_{21} & \dots & RR_{i1} \\ RR_{12} & RR_{22} & \dots & RR_{i2} \\ \vdots & \vdots & \vdots & \vdots \\ RR_{1n} & RR_{2n} & \dots & RR_{in} \end{bmatrix} \tag{37}$$

In the matrix (37), i is the month of the year (e.g. $1 \leq i \leq 12, i = 1$ (January), $i = 2$ (February)…) and j is the year under consideration with n being maximum (e.g. $1948 - 2017, n = 70$).

However, if we decided to select all years, m, associated with a certain phase of a planet ψ, occuring at a certain time of the year from the above dataset, n, then a new dataset of years representing the planet in the phase would take the form,

$$RR_{ij\psi} = \begin{bmatrix} RR_{11} & RR_{21} & \dots & RR_{i1} \\ RR_{12} & RR_{22} & \dots & RR_{i2} \\ \vdots & \vdots & \vdots & \vdots \\ RR_{1m} & RR_{2m} & \dots & RR_{im} \end{bmatrix} \quad (38)$$

In the matrices (37) and (38), n > m. These matrices were used for subsequent calculations and determinations of some further statistical analysis in sub-sections that follow. The result of this further analysis was used to derive rainfall attributes useful in forecasting and climate predictions.

The other consideration in this study is that, the gravitational forces exerted by the planets as they move is a quantity that varies sinusoidally as shown in the motion geometries (in Section 3.1). The "opposite" phases of the planets have been associated with maximum and minimum values of the gravitational forces exerted by the planets. This section attempts to statistically relate the two sets of variables, that is, rainfall during maximum gravitational force (or rainfall during minimum gravitational force) at a given month and gravitational forces of individual bodies. This was done using plots of regression and use of probability anomalies.

Rainfall anomalies were obtained from the difference between the observed rainfall at certain phases and the mean value. The observed values in month *i* are the means calculated from *j* years when a celestial body in one of the key phases is observed in a certain month, say January. The average value for month *i* for all *n* years is given in Equation (39);

$$\overline{RR}_i = \frac{1}{n}\sum_{j=1}^{n} RR_{ij} \quad (39)$$

Using the moon as an example (where new moon and full moon are the opposing phases), the rainfall average in month *i* when the full moon (ψ_+) is observed in some predetermined dates for "m" years is given in Equation (40);

$$\overline{RR}_{i,\psi_+} = \frac{1}{m}\sum_{j=1}^{m} RR_{ij} \tag{40}$$

And similarly, the rainfall average in month *i* when new moon (ψ_-) is observed at the same dates (as above) for "*l*"years is given in Equation (41);

$$\overline{RR}_{i,\psi_-} = \frac{1}{l}\sum_{j=1}^{l} RR_{ij} \tag{41}$$

From Equations (39), (40) and (41), the average rainfall anomaly on month *i* during the full moon (ψ_+) and New Moon (ψ_-) on the same dates would be;

$$\overline{RR}'_{i,\psi_+} = \overline{RR}_{i,\psi_+} - \overline{RR}_i \tag{42}$$

$$\overline{RR}'_{i,\psi_-} = \overline{RR}_{i,\psi_-} - \overline{RR}_i \tag{43}$$

A similar process is then repeated with the other celestial bodies with the average rainfall anomalies now assigned to the "opposite" phases, by use of Equations (42) and (43). The opposite phases are; New moon and Full moon for the Moon, Superior Conjunction and Inferior Conjunction for the inferior planets and Conjunction and opposition for the superior planets. The rainfall anomalies given in equation (42) and (43) can be correlated and compared to the gravitational force, $F_{i,\psi}$ as given in Equation (21) and (22).

4.2.6.2 *Setting Up the Null Hypothesis*

From section 3.1, it has been shown that the gravitational forces from the planets have a sinusoidal motion with maximum and minimum values at the opposite phases of the motions exhibited by all the bodies.

That, therefore, means that the rainfall at the two points should exhibit opposite characteristics and if a correlation coefficient was to be determined between rainfall variations associated with the Full Moon ($\overline{RR}'_{i,\psi_+}$) and rainfall variations associated with the New Moon ($\overline{RR}'_{i,\psi_+}$) they should show a strong relationship, that is, the correlation coefficient should have a value other than zero. If the two variables $\overline{RR}'_{i,\psi_+}$ and $\overline{RR}'_{i,\psi_-}$ were to be regressed, they would have a linear relationship represented in Equation (44);

$$\overline{RR}'_{i,\psi_+} = \sigma_1 \overline{RR}'_{i,\psi_-} + \sigma_2 \quad (44)$$

σ_1 and σ_2 are constants. The condition, $\sigma_1 < 0$ if the two were to have an opposite effect. In summary the null hypothesis is given as;

H_o: $\gamma > 0$, $\sigma_1 > 0$, $\sigma_1 = 0$, Orbital motions of the planets have no relation with the rainfall

H_1: $\gamma < 0$, $\sigma_1 < 0$, Orbital motions of the planets have a relation with the rainfall

This hypothesis was assessed for all the 12 zones and for all the planets in consideration including the moon to establish whether there is a relationship between their motions and the rainfall in these zones.

4.2.6.3 *Determination of Extremes by Probability of Exceedance and Probability Anomaly*

The probability of exceedance refers to the chance of the occurrence of rainfall exceeding some given value *RR mm*. The probability of exceedance $P[X > RR]$ is expressed as a fraction or as a percentage.

If the full dataset used in the study has $j = n$ years then the probability of exceedance of the same *RR* mm in the same month *i* is given in Equation (45) as;

$$P_{ij}[X > RR] = \frac{a}{n} \quad (45)$$

In Equation (45), a is the number of years that had more than *RR* mm in month *i*.

Let the symbol ψ_+ represent a celestial body in one phase and ψ_- in the opposite phase. And let the number of years when a certain phase of the celestial body occurs at a pre-determined period, for example, Full Moon, (represented by ψ_+) in e.g. the dates 1st to 7th March, be equal to b out of the set of years, m (refer to matrix (37) and (38)). The probability of rainfall exceeding RR mm in the i th month of the year for this dataset is given in Equation (46) as;

$$P_{ij\psi_+}[X > RR] = \frac{b}{m} \quad (46)$$

If the analysis was extended to years ($j = l$) when the New Moon (represented by ψ_-) was observed in the same dates and c number of years were found to be more than *RR* mm in the

same month i, then the probability of exceedance during this phase would be as given in Equation (47),

$$P_{ij\psi\_}[X > RR] = \frac{c}{l} \tag{47}$$

The three probabilities given in Equations (45), (46) and (47) were used to determine the characteristics of the monthly rainfall during the key phases of the moon and planets. The probability plots for $i = 1$ to $i = 12$ months will indicate the probability variations in a zone.

In general, if we set the thresholds at the following levels; RR = 0, 5, 10, 20, 30, 40, 50, 75, 100 mm, then the probability of exceedance associated with these thresholds can be given as given in the Matrix (48);

$$P_i = \begin{bmatrix} P_1[X > 0] & P_2[X > 0] & \dots & P_n[X > 0] \\ P_1[X > 5] & P_2[X > 5] & \dots & P_n[X > 5] \\ \vdots & \vdots & \vdots & \vdots \\ P_1[X > 100] & P_2[X > 100] & \dots & P_n[X > 100] \end{bmatrix} \tag{48}$$

For a celestial body, say, in opposition (represented by ψ_+) the matrix (48) can be written as Matrix (49);

$$P_{i\psi_+} = \begin{bmatrix} P_{1\psi_+}[X > 0] & P_{2\psi_+}[X > 0] & \dots & P_{n\psi_+}[X > 0] \\ P_{1\psi_+}[X > 5] & P_{2\psi_+}[X > 5] & \dots & P_{n\psi_+}[X > 5] \\ \vdots & \vdots & \vdots & \vdots \\ P_{1\psi_+}[X > 100] & P_{2\psi_+}[X > 100] & \dots & P_{n\psi_+}[X > 100] \end{bmatrix} \tag{49}$$

And for the same body in the opposite phase (represented by $\psi\_$) matrix (48) becomes matrix (50);

$$P_{i\psi\_} = \begin{bmatrix} P_{1\psi\_}[X > 0] & P_{2\psi\_}[X > 0] & \dots & P_{n\psi\_}[X > 0] \\ P_{1\psi\_}[X > 5] & P_{2\psi\_}[X > 5] & \dots & P_{n\psi\_}[X > 5] \\ \vdots & \vdots & \vdots & \vdots \\ P_{1\psi\_}[X > 100] & P_{2\psi\_}[X > 100] & \dots & P_{n\psi\_}[X > 100] \end{bmatrix} \tag{50}$$

In Equation (50), $1 \leq i \leq n$, and n = 365 days for a one-year period and n = 1095 for a three-year period.

The probability anomaly, $P_i'[X > RR]$ is defined in this study as the probability of the years associated with New Moon or Full Moon at certain predetermined dates (e.g. 1st to 7th March) subtracted from the normal. Using the Equations (45) and (46), the probability anomaly for the occurrence of rainfall of more than RR mm on month i during the Full Moon (ψ_+) is given in Equation (51) as;

$$P'_{i,\psi_+}[X > RR] = P_{i\psi_+}[X > RR] - P_i[X > RR] \quad (51)$$

$$= \frac{b}{m} - \frac{a}{n}$$

And similarly, during New Moon (ψ_-) and by using Equations (45) and (47), the probability anomaly for the occurrence of rainfall of more than *RR* mm in the same month during New moon would be as given in Equation (52);

$$P'_{i,\psi_-}[X > RR] = P_{i\psi_-}[X > RR] - P_i[X > RR] \quad (52)$$

$$= \frac{c}{l} - \frac{a}{n}$$

The quantities P'_{i,ψ_+} and P'_{i,ψ_-} were then plotted through the period $1 \leq i \leq 12$ where *i* is the month. A similar process was repeated with the other celestial bodies with a planet observed at opposing phases e.g. Venus at Inferior Conjunction and Venus at Superior Conjunction with various Probability Anomalies calculated at levels already assigned. It should be noted that the thresholds can be adjusted when the need arises. The two were also compared with the $F_{i,\psi}$ given in Equation (21) and (22).

4.2.7 *Modelling Rainfall by Sinusoidal Curve Fitting*

Naturally, rainfall variations do exhibit some sinusoidal characteristics that makes us to believe that the variations may be caused by drivers with sinusoidal characteristics. The periodic pattern of monthly rainfall data can be estimated by a periodic sinusoidal component with a known wavelength and modelled using the Fourier series concept as given in Equations (1), (2) and (36).

A sinusoidal model developed was as a result of the influence of some detected periods that are associated with the drivers. The models are capable of describing the rainfall data with minimum error by use of correlograms, histograms, residuals and other statistics. It should be noted that a better model is one that is generated with a wider range of historical data to detect many variations even those with large periodicities.

Datas with periodicities greater than the data range used in this study presented a challenge which influenced us to explore other means to detect them. These other means included the use of historical data of extreme climate and compare them with the celestial phases.

The residuals were assumed to follow the normal probability distribution with zero mean and a constant variance. This was evaluated using a probability plot of the residuals. In testing the validity of the fitted models, we used the F-statistics to test the overall significance of the sinusoidal models. In order to reject the null hypothesis that group means are equal, we needed a high F-value.

The models were fitted by non-linear least squares estimation using sinusoidal functions by adjusting the phase, amplitude and wave numbers for each sinusoidal component. Even with a good fit, sometimes the residual can be non-random suggesting that there are some key components missing in the models. Adjustments were made until the residuals did not show any discernible relationships.

Suppose the rainfall data variation in consideration contains a deterministic perturbation which has a periodic component at a given frequency, $2\pi/\tau$ where τ is the period of a cycle. This component would be given as in Equation (53);

$$\overline{RR}(t) = A\sin(t - t_o)k\frac{2\pi}{\tau} \tag{53}$$

If the perturbation contains *n* periodic components, Equation (53) becomes Equation (54);

$$\overline{RR}(\mathrm{t}) = \sum_{k=1}^{n} A_k \sin(t - t_k)k\frac{2\pi}{\tau_k} \tag{54}$$

From Equation (53) and Equation (54), *k* is the wave number, τ is the period of the cycle, τ_k is the period of a wave at wave number *k*, $\overline{RR}$ is model value, *t* is the time after conjunction or opposition, A_k amplitude at wave number k , t_o, initial time and t_k is the phase shift at wave number *k.*

Equation (54) was taken as the main signal of the perturbation, and was used to estimate the actual rainfall data. However, most rainfall datasets are normally characterised by changes in amplitudes or strengths of the data from time to time through a time series. The estimates may vary greatly if the problem is not factored into the curve fitting. To do so, we introduced a transient function as a factor of the Equation (54) so that it becomes Equation (55);

$$\overline{RR}(\mathrm{t}) = \left(C + B\sin\left(t - t_f\right)f\frac{2\pi}{\tau_k}\right)\sum_{k=1}^{n} A_k \sin(t - t_k)k\frac{2\pi}{\tau_k} \tag{55}$$

In Equation (55), C and B are constants, t_f is the phase shift and f is the wave number of the transient factor. By adjusting the variables and the constants and carefully selecting the correct wave numbers in Equation (55), we were able to get appropriate fit for all the datasets for all the zones.

CHAPTER FIVE: RESULTS AND DISCUSSIONS

In this chapter, the results of this study are presented and discussed with reference to the objective of the study, which is to determine the influence of planets orbital motions on the terrestrial weather and climate with the focus on the rainfall over East Africa. The three specific objectives set out in Section 1.3 of this study and their associated and obtainable results have been discussed in the sections; 5.2, 5.3, and 5.4.

5.1 Temporal Variation of Gravitational Forces

The variation of the gravitational forces exerted on a unit mass of air parcel on Earth by different planets is given in Figures 5 to 8. The forces have been calculated using Equations (21) and (22) based on the geometry of the orbits shown in Figures 2, 3 and 3(b).

Figure 5 shows the variation of gravitational force, $F_{♀}$ (x $10^{-8}N$) exerted by Venus (♀) on a unit mass of air parcel on Earth during a full Venus orbital cycle from superior Conjunction (t = day 1) to superior Conjunction (t = day 585). From the figure, we note sudden rise to the peak (at day 292) and then a sudden drop of the gravitational force within a short period of about 60 days as Venus transited through the Inferior Conjunction phase. The rest of the Venus orbital cycle is nearly even and at low values especially near the Superior conjunction phase.

This indicates a bigger physical influence of gravitational force by Venus during the Inferior conjunction phase than any other time during its cycle. It is during the Inferior conjunction phase that the planet is closest to the Earth. In the period before or after the Inferior conjunction, the planet appears as a bright morning or evening "star" in the sky, an observation commonly used by IK forecasters in climate predictions. This confirms the reason why the traditional forecasters (in western and northern Kenya) focus much on a bright morning or evening "star" in their forecasts (Ogallo *et. al*., 2010; Luseno *et. al*., 2002). All these observations and interpretations were discussed in sections 2.4 and 2.5.

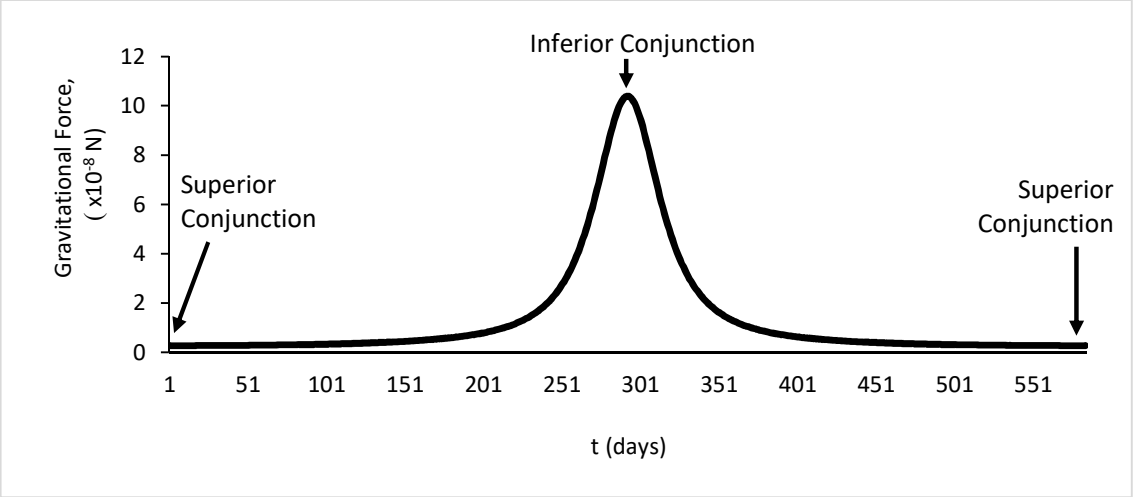

Figure 5: Variation of gravitational force exerted by Venus, $\boldsymbol{F_{♀}}$ $(\boldsymbol{10^{-8}N})$ on a unit mass of air parcel on Earth during a full Venus orbital cycle-from superior conjunction (t = day1) to superior conjunction (t = day 585).

Figure 6 shows the variation of gravitational force exerted by Jupiter, $F_{♃}$ $(\text{x } 10^{-8}N)$ on a unit mass of air parcel on Earth during a full Jupiter orbital cycle from Conjunction (t = 1) to Conjunction (t = 399). From the figure, we note a sinusoidal variation with a minimum point of the gravitational force exerted by Jupiter at approximately Day 200 after the opposition phase. The minimum point coincides with the conjunction phase while the maximum coincides with the opposition phase. The maximum force at opposition phase means that Jupiter exerts a relatively bigger gravitational force on Earth's atmosphere than any other time during its cycle. It is during the opposition phase that the planet is closest to the Earth.

Jupiter appears as one of the brightest stars when at its opposition phase and this tells us why it is a major focus of attention to the traditional forecasters in East Africa especially in the period before the main seasons (Luseno *et al*., 2002).

Figure 7 shows the variation of gravitational force exerted by Saturn, $F_{♄}$ on a unit mass of air parcel on Earth during a full Saturn orbital cycle-from Conjunction (t = 1) to Conjunction (t = 379). From the figure, we note similar features as those exhibited by Jupiter as shown in Figure 6 where a sinusoidal variation with a minimum point of the gravitational force exerted by Saturn at approximately Day 190 after opposition phase. It is at the opposition phase that Saturn exerts a bigger gravitational force on our atmosphere than any other time in its cycle.

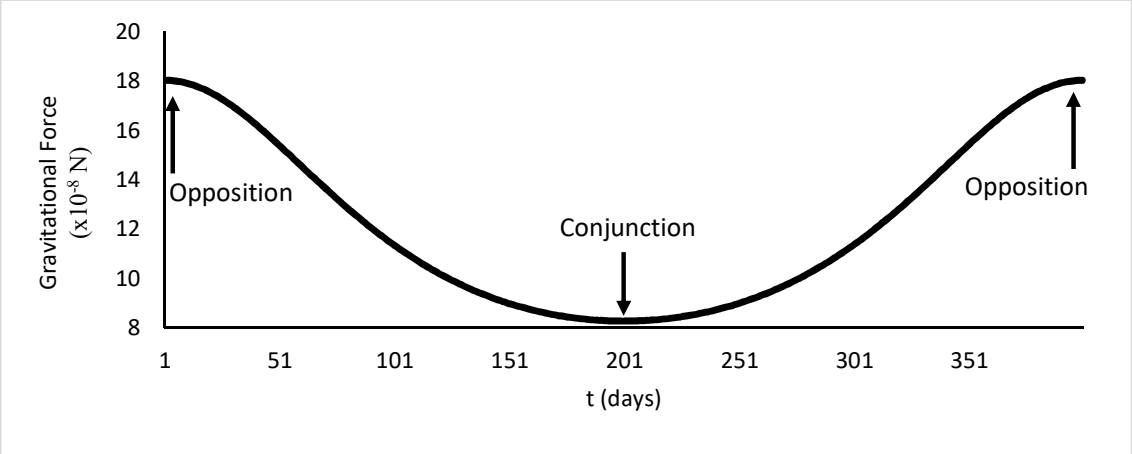

Figure 6: Variation of gravitational force , $F_{♃}$ exerted by Jupiter on a unit mass of air parcel on Earth during a full Jupiter orbital cycle-from opposition (t = 1) through conjunction to the next opposition (t = 399).

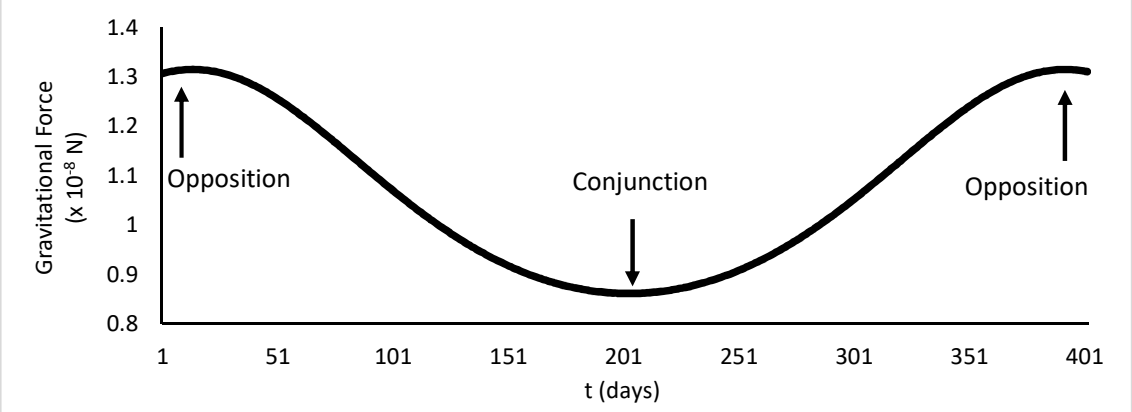

Figure 7: Variation of gravitational force, $F_{♄}$ exerted by Saturn on a unit mass of air parcel on Earth during a full Saturn orbital cycle-from opposition (t = 1) through Conjunction to the next opposition (t = 379).

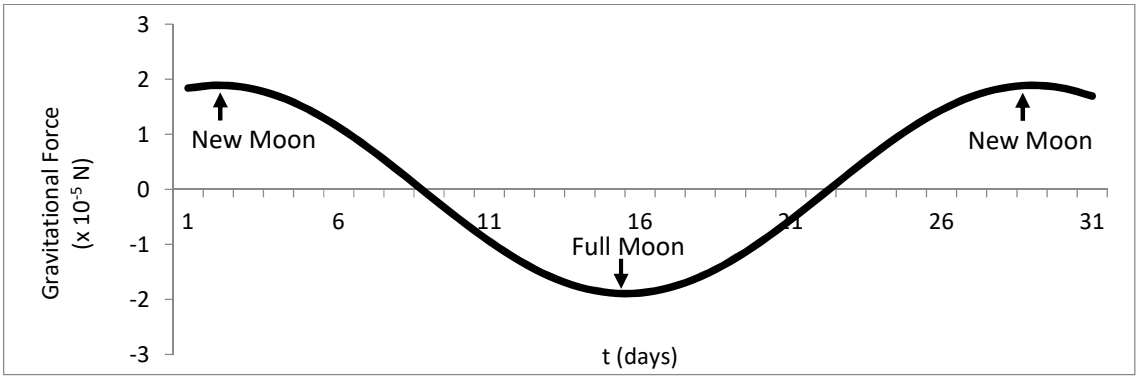

Figure 8: Variation of gravitational force by the moon exerted vertically upwards($\tilde{F}_{ψ}$) on a unit mass of air parcel on Earth during a full Lunar orbital cycle-from New Moon (t = 1) through Full moon phase to the next New moon phase (t = 28). Note that all other cyclic and orbital motions of the moon have been ignored.

Although both Jupiter and Saturn share nearly the same characteristics, Saturn appears to a naked eye as a faint "star" and is also frequently used in conjunction with other planets to make traditional forecasts.

The variation of gravitational force exerted by planet Mars follows the same pattern as that displayed in Figures 6 and 7, but spans from Conjunction (t = 1) to Conjunction (t = 783). However, it should be noted that the Mars orbit around the Sun is characterised by changes in its shape due to a highly eccentric orbit.

Figure 8 shows the variation of gravitational force by the moon exerted vertically upwards $\tilde{\mathbf{F}}_{\psi}$ on a unit mass of air parcel on Earth during a full Lunar orbital cycle-from New Moon (t = 1) through Full Moon phase to the next New moon (t = 28). Note that all other cyclic and orbital motions of the moon were ignored. When the gravitational force is directed or resolved vertically upwards (in the direction, $\widehat{\boldsymbol{k}}$), the maximum value is at New Moon phase while the Minimum value is at Full moon phase. The maximum and minimum values satisfy the conditions given in Equations (23) and (24). The absolute values of the gravitational forces of the moon are highest at the Full and New moon phases which confirms the occurrence of high oceanic tides during the two phases.

An important observation from the variations of the gravitational forces of the planets is that the forces exerted by Saturn are about one order of magnitude less than that of Jupiter and Venus and 3 orders of magnitude less than that of the moon (see the scales in Figures 5, 6 and 7 for comparison). Another observation to consider is that the periodicities of the cyclic variations of the forces exerted by Jupiter, Venus, Saturn and Mars are one order of magnitude higher than that of the moon. That means the variations of the gravitational forces of the planets can be associated with relatively longer time scale variations of rainfall when compared to those of the moon.

5.2 Results of the Planet and the Moon's Influence on Rainfall

5.2.1 *Influence of the Planets Position on the Monthly Rainfall*

Results presented in this study, compare and seek to show the relationship between variations of the monthly rainfall anomalies through the year for observations of planets at the opposite phases. It was not possible to use rainfall for all the 12 zones (see Figure 1 for easier reference to the zones), but randomly selected a few zones within the study area so that a number of geographical and climatic conditions of East Africa are considered.

Figure 9 shows two curves each representing variations of mean rainfall anomalies in Zone I. One curve is for Venus observed in the Inferior Conjunction phase ($\overline{RR}'_{i,♀_+}$); and the other when Venus is observed in the Superior Conjunction phase ($\overline{RR}'_{i,♀_-}$) both of which are observed during the period October-November.

From the variation of the curves it was noted that negative anomalies from April to December are observed during a superior conjunction while positive anomalies are observed during an inferior conjunction. This observation is even more conspicuous during the two main East Africa rainfall seasons especially during OND season. This means that observation of the two opposite phases in the period October to November means enhanced rainfall for one of the curves (representing variation of rainfall during Opposition) or reduced rainfall in the other curve (representing variation of rainfall during conjunction) in Zone 1. The correlation coefficient between the two curves is -0.4.

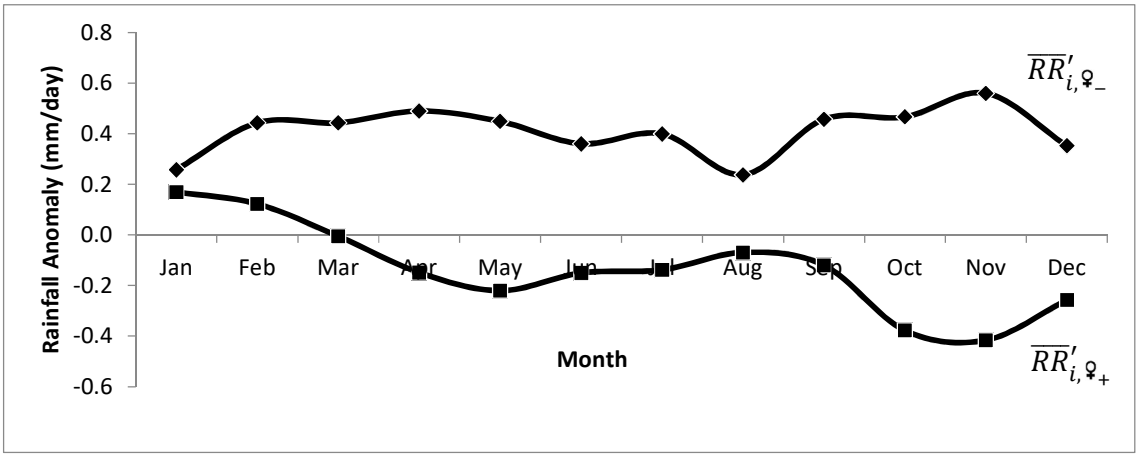

Figure 9: The curves of the variation of the mean rainfall anomalies (mm/day) in Zone 1 when Venus is observed in the inferior conjunction phase (diamond shapes), $\overline{\boldsymbol{RR}}'_{i,♀_-}$ and superior conjunction phase (square shapes) $\overline{\boldsymbol{RR}}'_{i,♀_+}$. Both phases are observed anytime within the period October-November. The base period is 1948-2017.

Figure 10 shows the curves of the variation of the mean rainfall anomalies (mm/day) in Zone 1 when Saturn is observed in the opposition phase (diamond shapes) and superior conjunction phase (square shapes). Both phases are observed anytime within the month of May. The base period is 1948-2017.

From the variation of the curves it was noted that negative anomalies are observed throughout the year during a superior conjunction phase of Saturn in May while positive anomalies are observed during an inferior conjunction. Just like the observed features in Figure 9, this

observation is even more conspicuous during the two main East Africa rainfall seasons and a little more prominent during the MAM season. This means that occurrence of the two opposing phases associated with Saturn in the period October to November also means enhanced or reduced rainfall in Zone1. The correlation coefficient between the two curves is -0.4.

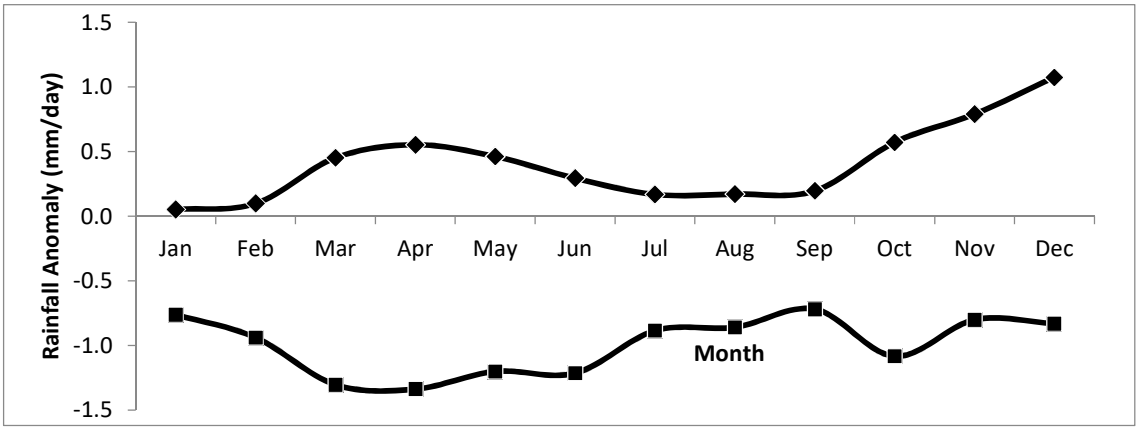

Figure 10: The curve of variation of mean rainfall anomalies in Zone 1 when Saturn is observed in the Opposition phase (diamond shapes), $\overline{RR}'_{i,\,\text{♄}_-}$ and the second curve when it is observed in Conjunction phase (square shapes) $\overline{RR}'_{i,\,\text{♄}_+}$. Both phases are observed anytime within the month of May. Base period 1948-2017.

While the two cases demonstrated in Figure 9 and Figure 10 exhibit features that are similar, not all cases are the same as the two figures. Figure 11 and Figure 12 (below) are good examples of rainfall anomaly variations that have other unique characteristics to consider.

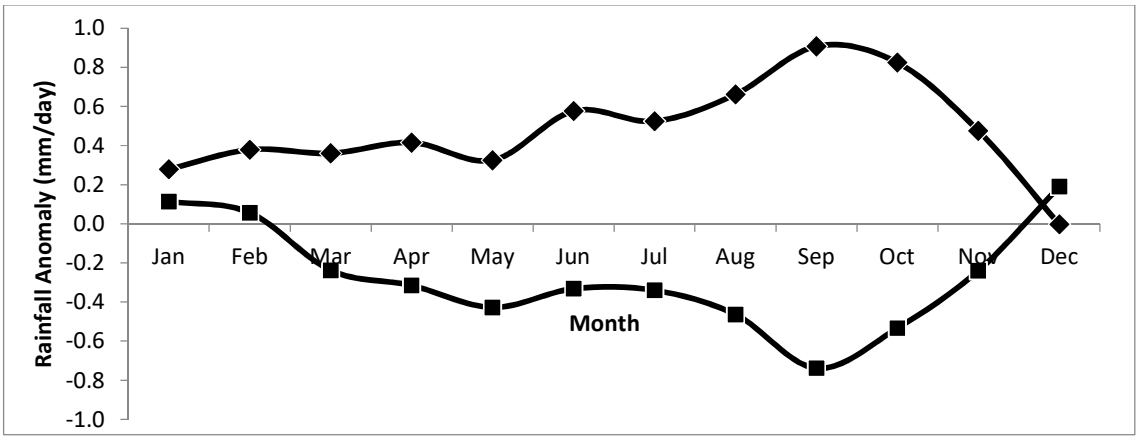

Figure 11 : The curves of the variation of the mean rainfall anomalies (mm/day) in Zone 3 when Saturn is observed in the opposition phase (diamond shapes) $\overline{RR}'_{i,\,\text{♄}_+}$ and conjunction phase (square shapes) $\overline{RR}'_{i,\,\text{♄}_-}$. Both phases are observed anytime within the month of February. The base period is 1948-2017.

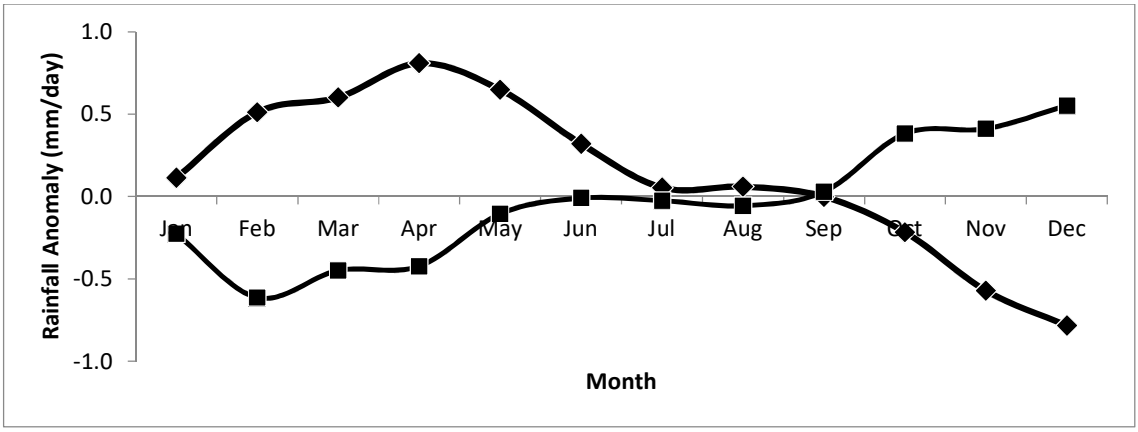

Figure 12: The curves of the variation of the mean rainfall anomalies (mm/day) in Zone 7 when Jupiter is observed in the opposition phase (diamond shapes) $\overline{RR}'_{i,\,4_+}$, and conjunction phase (square shapes), $\overline{RR}'_{i,\,4_-}$, both of which are observed during the month of March. The base period is 1948-2017.

Figure 11 shows the curves of the variation of the mean rainfall anomalies (mm/day) in Zone 3 when Saturn is observed in the opposition phase (diamond shapes) and conjunction phase (square shapes). Both phases are observed anytime within the month of February. It was noted that negative anomalies from March to November are observed during a superior conjunction phase in February while positive anomalies from March to November are observed during an inferior conjunction. The magnitude of the anomalies in both cases increase as one approaches September. This means that occurrence of the two opposing phases in the month of February signify enhanced or reduced rainfall in Zone 3 with the highest absolute values of the anomalies observed from August to October. The correlation coefficient between the two curves is -0.8.

Figure 12 shows the curves of the variation of the mean rainfall anomalies (mm/day) in Zone 7 when Jupiter is observed in the opposition phase (diamond shapes) and conjunction phase (square shapes). Both phases are observed anytime within the month of March. In this graph, negative anomalies are observed from October to December during an opposition phase of Jupiter in March while positive anomalies are observed between January and June during the same phase. On the other hand, positive anomalies are observed from October to December during a conjunction phase of Jupiter in March while negative anomalies are observed between January and May during the same phase.

The variations of rainfall during both phases exhibit opposite characteristics. The magnitude of the anomalies in both cases tend to maximize during both MAM and OND rainfall seasons. This means that occurrence of the two opposing phases of Jupiter in the month of March signify

enhanced rainfall in one season and a reduction of rainfall in the following season all in Zone 7. The correlation coefficient between the two curves is -0.9.

Table 1: Correlation Coefficients between two rainfall anomalies when Jupiter is observed in the Opposition phase ($\overline{RR}'_{i,\mathcal{U}_+}$) and rainfall anomalies when Jupiter is observed in Conjunction phase ($\overline{RR}'_{i,\mathcal{U}_-}$). For each zone, the correlation coefficients are displayed for each month during which the two phases are observed.

Zone	Jan	Feb	Mar	Apr	May	Jun	Jul	Aug	Sep	Oct	Nov	Dec
1	-0.7	-0.6	-0.2	0.3	-0.4	-0.1	-0.6	-0.2	0.3	-0.4	-0.1	-0.2
2	-0.4	-0.7	-0.7	-0.3	-0.3	-0.2	-0.7	-0.7	-0.3	-0.3	-0.2	-0.4
3	-0.5	-0.8	-0.9	-0.3	0.3	-0.8	-0.8	-0.9	-0.3	0.3	-0.8	-0.5
4	-0.4	-0.7	-0.8	0.0	0.6	-0.5	-0.7	-0.8	0.0	0.6	-0.5	-0.5
5	0.6	-0.5	-0.7	-0.9	-0.1	-0.1	-0.5	-0.7	-0.9	-0.1	-0.1	-0.1
6	-0.7	-0.7	-0.9	0.5	-0.4	-0.4	-0.7	-0.9	0.5	-0.4	-0.4	0.8
7	-0.9	-0.9	-0.9	0.3	-0.7	-0.9	-0.9	-0.9	0.3	-0.7	-0.9	-0.6
8	-0.9	-0.5	-0.5	-0.3	0.0	-0.1	-0.5	-0.5	-0.3	0.0	-0.1	-0.6
9	0.0	-0.3	0.0	-0.5	-0.4	-0.3	-0.3	0.0	-0.5	-0.4	-0.3	-0.7
10	-0.4	-0.4	-0.4	-0.2	-0.3	-0.6	-0.4	-0.4	-0.2	-0.3	-0.6	0.2
11	-0.8	-0.5	-0.6	-0.4	-0.7	-0.8	-0.5	-0.6	-0.4	-0.7	-0.8	-0.8
12	-0.4	-0.5	0.0	-0.3	-0.3	-0.3	-0.5	0.0	-0.3	-0.3	-0.3	-0.4

Table 1 shows an array of correlation coefficients where a coefficient is determined between, one; rainfall anomalies, when, Jupiter is observed in the Opposition phase and two; rainfall anomalies when Jupiter is observed in Conjunction phase all in the same month.

For each zone, the correlation coefficients are displayed in each month of observations of the two opposite phases. This table is a summary of relationships (in terms of correlation coefficients) between anomalies associated with opposite phases and covers all the zones. A negative value means there is an inverse relationship. A relatively bigger absolute value means the relationship is stronger. This simple inference was similarly applied to Tables 2, 3 and 4.

From Table 1, on average, there is a relatively good relationship between Jupiter orbital motions and the rainfall in the months of January, February, March, July and August which are mainly the off-season periods. During the rainfall season, the relationship is comparatively lower especially in the drier climates of the region. In February and March, higher negative values are found especially in areas in the eastern half of the study region (most of Kenya and the eastern half of Tanzania). The same high negative values are repeated in the months of July and August.

This behaviour can be related to the presence of a few drivers of climate during the off-season period so that the Jupiter orbital motion becomes one of the few dominant drivers. During the main rainfall season, a lot more drivers may be involved so that Jupiter's contribution to the total rainfall variation is relatively small and hence a relatively weaker relationship. This means that the observation of Jupiter in both conjunction and opposition phase can be used to determine off-season rainfall which is currently a big challenge.

However, there is an exception to this rule. In some cases, rainfall variations do not exhibit exact opposite behaviour because of a few data points with what seems to be characteristics of an outlier. In other cases, the correlation coefficient may acquire a positive value because of a single "outlier". By ignoring the "outliers", the correlation coefficient values have been found to indicate a better relationship.

Figure 13 shows the curves of variation of mean rainfall anomalies in Zone 7 when the new moon is observed and rainfall anomalies when Full moon is also observed, both during the same dates 11th - 15th March. In the graph, the variation goes through two years.

The rainfall variations associated with the phases of the moon have almost the same characteristics as the rainfall variations associated with the planets. The amplitudes in all the phases of the moon are found to be one order of magnitude less than the amplitudes of rainfall anomalies associated with the phases of the planets (see Figures 9, 10, 11 and 12 and compare the maximum and minimum values of the anomalies with the those in Figure 13). This is exhibited in all the zones and on this reason alone we find that the contribution to the overall effect on the rainfall by the moon on a longer time scale to be negligible and therefore ignored in subsequent analysis.

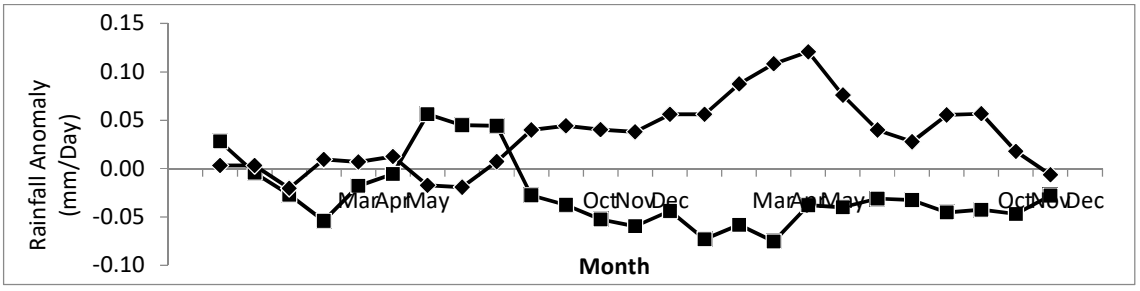

Figure 13**:** The curves of Variation of mean rainfall anomalies in Zone 7 when the new moon is observed and Full moon is also observed during the same dates 11-15 March. The variation goes through the year and the following 12 months. Base period 1948-2017

Table 2 : Table of Correlation Coefficients between two rainfall anomalies when, one Saturn is in the Opposition phase ($\overline{RR}'_{i,\text{♄}_+}$) and two; rainfall anomalies when Saturn is in Conjunction phase ($\overline{RR}'_{i,\text{♄}_-}$) . For each zone, the correlation coefficients are displayed for each month during which the two phases are observed.

Zone	Jan	Feb	Mar	Apr	May	Jun	Jul	Aug	Sep	Oct	Nov	Dec
1	-0.6	-0.8	-0.4	-0.3	-0.2	-0.6	-0.8	-0.4	-0.3	-0.2	-0.6	
2	0.0	-0.4	-0.2	-0.7	0.0	-0.4	-0.4	-0.2	-0.7	0.0	-0.4	
3	0.0	-0.6	-0.1	-0.8	-0.3	0.0	-0.6	-0.1	-0.8	-0.3	0.0	
4	-0.5	0.3	0.1	-0.9	-0.6	-0.1	+0.3	0.1	-0.9	-0.6	-0.1	
5	0.1	0.4	-0.1	-0.4	-0.2	-0.1	+0.4	-0.1	-0.4	-0.2	-0.1	
6	-0.5	-0.8	0.1	0.5	-0.6	-0.1	-0.8	0.1	0.5	-0.6	-0.1	
7	-0.7	0.5	0.1	-0.5	-0.2	0.0	+0.5	0.1	-0.5	-0.2	0.0	
8	-0.8	0.2	-0.1	0.1	0.1	-0.1	+0.2	-0.1	0.1	0.1	-0.1	
9	-0.1	-0.4	-0.8	-0.4	0.5	-0.4	-0.4	-0.8	-0.4	0.5	-0.4	
10	-0.8	0.0	-0.7	-0.1	-0.3	-0.6	0.0	-0.7	-0.1	-0.3	-0.6	
11	-0.6	-0.6	-0.4	-0.4	0.4	-0.6	-0.6	-0.4	-0.4	0.4	-0.6	
12	-0.4	-0.5	0.0	-0.3	-0.3	-0.3	-0.5	0.0	-0.3	-0.3	-0.3	

Table 2 shows correlation coefficients between, one; rainfall anomalies when Saturn is in the Opposition phase and two; rainfall anomalies when Saturn is in Conjunction phase all observed in the same month.

From the table, the coefficients exhibited show high negative values throughout the year. On average, relatively higher negative values of the coefficient are noted in January, February, April, July and September, mainly in zones I, III, VI, IX, X and XI, which cover most of Uganda, Burundi, Rwanda and a few parts of northern Tanzania and northern Kenya.

Like, Jupiter, the Saturn orbital motion seems to have a good relation with the rainfall in the dry period, January-February for the reason, that the drivers involved in influencing rainfall may be few with one of the main dominant drivers being the Saturn orbital motions.

Table 3 shows correlation coefficients between, one; rainfall anomalies when Venus is in the Inferior Conjunction phase, and two; rainfall anomalies when Venus is in Superior Conjunction phase all observed in the same cluster. Generally, coefficients exhibited in the table, show high negative values of the coefficient which shows a good relation with rainfall in the period October to February.

Table 3 : Table of Correlation Coefficients between rainfall anomalies when Venus is in the Inferior Conjunction phase ($\overline{RR}'_{i,♀+}$) and rainfall anomalies when in Superior Conjunction phase ($\overline{RR}'_{i,♀-}$) all observed in the same period (made up of 2 or 3 months). Due to the few number of observations made per month, it was found practical to combine two or three months to increase the number of observations per cluster.

Zone	Jan-Feb	Mar-Apr	May-Jun-Jul	Aug-Sep	Oct-Nov-Dec
1	-0.40	-0.27	-0.09	-0.10	-0.40
2	-0.77	-0.27	-0.03	-0.03	-0.77
3	-0.60	-0.19	-0.13	+0.38	-0.60
4	+0.27	-0.15	-0.46	+0.13	+0.27
5	+0.55	-0.27	-0.25	+0.04	+0.55
6	-0.88	-0.92	-0.63	-0.82	-0.85
7	-0.29	-0.66	-0.14	+0.25	-0.29
8	-0.19	0.00	+0.69	-0.58	-0.19
9	-0.77	-0.08	-0.69	-0.57	-0.77
10	-0.25	-0.31	-0.19	-0.33	-0.25
11	-0.41	0.00	-0.62	0.00	-0.41
12	-0.39	-0.36	+0.26	+0.09	-0.39

On average, high negative values of the coefficient were noted in October to February, mainly in zones I, II, III, IV, V, VI and IX, which cover mostly the dry lowlands of the region at a time when the overhead sun is to the south of the equator. For the rest of the period (March to September) for these zones, the relationship between rainfall and the Venus orbital motions is relatively poor. This can be interpreted to mean that zones I, II, III, IV, V, VI and IX have a good relationship with Venus orbital motions during OND and the subsequent dry season, January-February and could be a major factor in the off-season rainfall that falls during the January-February period. It is possible that the orbital motion of Venus forms one of the dominant drivers of climate during the period when the sun is mainly to the south of the Equator. During the period when the overhead Sun is to the north, a lot more drivers may be involved so that the contribution of Venus motions to the total rainfall variation is relatively small and hence a relatively weaker relationship.

Also noted is that zones X, XI and XII have a relatively poor relationship of Venus with rainfall throughout the year. This may be due to the fact that zones X, XI and XII are found in an area within the study area that is dominated by highlands, valleys, lakes, wetlands, numerous rivers and mountains. In addition, climate drivers are numerous in this area with effects from the

Congo, the ITCZ and other drivers making a complicated combination of climate influences. With the physical influences in the picture, the Venus orbital motions may not be able to offer significant contribution to the overall influence of rainfall in the area.

Table 4: Correlation Coefficients between rainfall anomalies when Mars is in the Opposition phase ($\overline{RR}'_{i,\sigma_+}$) and rainfall anomalies when in Conjunction phase ($\overline{RR}'_{i,\sigma_-}$) all observed in the same period. Due to the few number of observations made per month, it was found practical to combine three months to increase the number of observations per cluster.

Zone	Jan-Feb-Mar	Apr-May-Jun	Jul-Aug-Sept	Oct-Nov-Dec
1	-0.04	0.26	-0.39	-0.08
2	-0.16	-0.14	+0.30	-0.30
3	-0.09	-0.54	+0.22	+0.43
4	-0.79	-0.84	+0.06	+0.58
5	-0.42	-0.25	+0.91	-0.19
6	-0.51	+0.52	+0.61	-0.76
7	-0.79	+0.20	+0.72	-0.82
8	-0.29	+0.03	+0.81	-0.38
9	-0.21	-0.43	-0.80	+0.56
10	+0.08	-0.05	+0.04	+0.60
11	-0.03	+0.03	+0.36	-0.55
12	-0.22	-0.31	-0.07	-0.26

Table 4 shows Correlation Coefficients between, one; rainfall anomalies when planet Mars is in the Opposition phase and two; rainfall anomalies when Mars is in Conjunction phase all observed in the same period.

From Table 4, high negative values are found from the month of July to December and relatively lower values for the rest of the year. This is especially so in the zones IV to IX, which cover mainly areas south of the equator, that is, most of Tanzania, Rwanda, Burundi and southern parts of Kenya. On average, high negative values of the coefficient are noted in January to March, mainly in zones IV to VII, which cover mostly the dry lowlands near the Indian Ocean coast when the sun is to the south of the equator. During OND, areas of high negative values cover most of Tanzania which generally means the Mars orbital motions do have a relatively good relation with rainfall there. This means that the planet Mars can be a useful rainfall indicator for areas to the south of the equator.

Rainfall in zone I, II, III, X, XI and XII seem to have a poor relation with the orbital motion of Mars in nearly the whole year. These are areas mainly to the north of the equator.

5.2.2 *The Performance of MAM and OND when Planets are Observed at Different Phases*

The rainfall performance for the MAM and OND seasons refers to the rainfall anomalies determined for the seasons. Positive rainfall anomalies in a season means the season has performed well and negative rainfall performance means the season has performed poorly. In this study, I present the performance of the seasons when certain planet phases are observed.

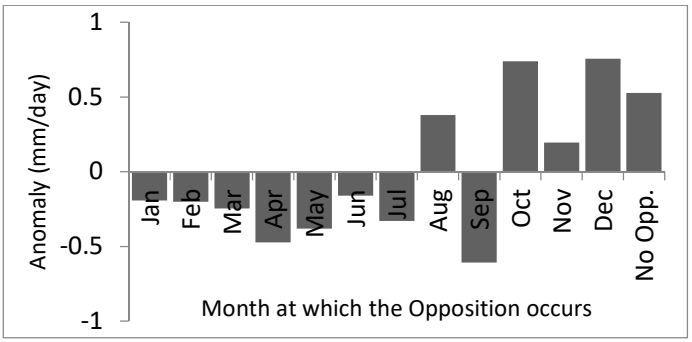

Figure 14: The Average Rainfall Anomaly in MAM season in Zone 1 when the Jupiter is observed at Opposition phase. An extra category is added at the end of the axis for years when there was no opposition observed.

Figure 14 shows the average rainfall anomaly in MAM season in Zone 1 when the planet Jupiter is observed at Opposition phase for a given month. The rainfall anomaly is determined for each and every month from January to December. From the graph, negative rainfall anomalies for MAM season are shown when Jupiter is observed at opposition at any time during the period January to July and positive anomalies are shown when Jupiter is observed at any time during the period October to December. This means that the MAM season in zone 1 performs poorly when Jupiter in Opposition phase is observed anytime between January and July and performs well when it is observed between September and December. The MAM season also performs well during the years when there was no opposition phase.

Almost a similar rainfall performance is noted in Zone IX when OND season is considered. Figure 15 shows the average rainfall anomaly in OND season for Zone IX when Jupiter is observed at Opposition phase. Like in Figure 14, the negative anomalies are noted between January and August when Jupiter in opposition is observed and positive values between

September and December. This means that the OND season in zone IX performs poorly when Jupiter in Opposition phase is observed anytime between January and August and performs well when it is observed between September and December. This also includes a cluster of years when there was no opposition phase.

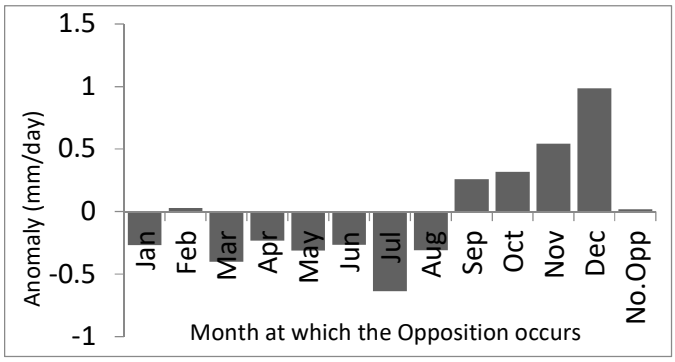

Figure 15: The average rainfall anomaly in OND season in Zone IX when the Jupiter is observed at Opposition phase. An extra category is added at the end of the axis for years when there was no opposition observed.

Figure 16 shows the average rainfall anomaly for MAM season in Zone I when the Planet Saturn is observed at Opposition phase. In general, positive MAM anomalies are shown any time Saturn is observed at Opposition phase between April and July and negative MAM anomalies when opposition observations occur the rest of the year. This means that the MAM season in zone I performs well when Saturn in Opposition phase is observed anytime between April and July and performs poorly when it is observed between September and December. The MAM season also performs poorly during the years when there was no opposition phase observed for Saturn.

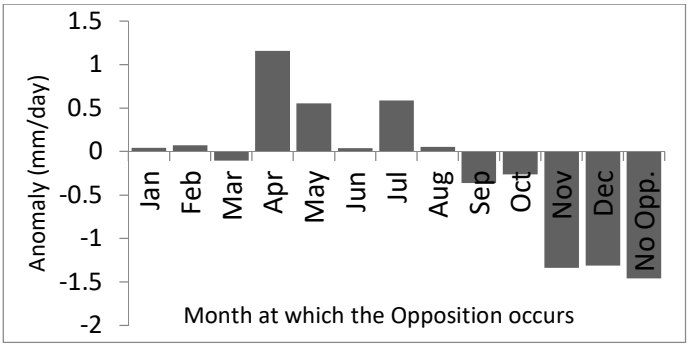

Figure 16 : The average Rainfall Anomaly in MAM season in Zone I when the Saturn is observed at Opposition phase. An extra category is added at the end of the axis for years when there was no opposition observed.

Figure 17 shows the average Rainfall Anomaly in OND season in Zone IX when the Saturn is observed at Opposition phase. Positive OND anomalies appear any time Saturn is observed at

Opposition phase between January and May and negative OND anomalies when opposition observations occur between June and November. This indicates that the OND season in zone IX performs well when Saturn in Opposition phase is observed anytime between January and May and performs poorly when it is observed between June and November. The OND season also performs poorly during the years when there was no opposition phase observed for Saturn.

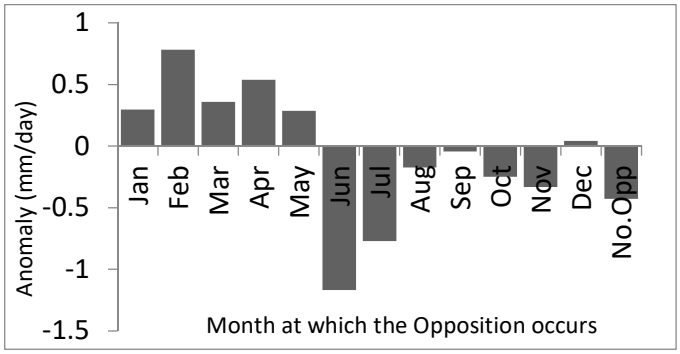

Figure 17 :The average Rainfall Anomaly in OND season in Zone IX when the Saturn is observed at Opposition phase. An extra category is added at the end of the axis for years when there was no opposition observed.

In all the four cases, Figures 14, 15, 16 and 17, we can deduce that not all opposition phases of the Saturn or Jupiter do behave the same way. The amounts of the OND and MAM rainfall anomalies vary with the time of the year when the oppositions of Saturn or Jupiter are observed. This means that rainfall characteristics during the same phase but at different times of the year are different and we believe this could be the same in all other zones. The only way to get the same rainfall characteristics in the same phase is when a phase is observed in the same month or cluster of another year. That can only happen when we consider a planet at a certain phase, say opposition, then the planet goes through a number of other oppositions before it falls back to the same phase in the same month or time of the year. This creates a rainfall cycle based on this line of thinking that is the focus in the next section.

5.3 Results of the Intra-Seasonal and Inter-Annual Variations of Rainfall

5.3.1 *Temporal Variation of Monthly Rainfall Anomalies*

In the last sub-section, we saw unique and consistent variation of the MAM and OND seasonal rainfall anomalies in zones I and IX associated with observations of Saturn and Jupiter oppositions made at individual months from January to December. Although we used Zones I and Zone IX (Section 5.2) in our analysis, it is assumed that all other zones are subject to

rainfall cycles of the same range as Zone I and Zone IX. This assumption is suggested due to the fact that the effects of the planets on the zones are global and would be appropriate if applied to all the zones.

Since the rainfall anomalies differ from Opposition to Opposition and from one conjunction to another, for both Saturn and Jupiter, we can assume that the anomalies only repeat when the same phase is observed in the same month of the year. For example, Jupiter at Opposition phase in January 1943, had the next Opposition phase in January 1954, 12 years later. The length of this cycle is 12 years and is referred to hereafter as "Jupiter rainfall cycle".

For that reason, there was a need to examine rainfall cycles based on the individual planet's opposition to opposition or conjunction to conjunction time span. In this section, we focus on the planets; Jupiter, Saturn, Mars and Venus whose cycles were considered in our analysis. The planets, Uranus and Neptune were also considered.

Table 5: Rainfall cycles based on time taken by the Venus in its orbital motion to move from Inferior Conjunction phase in January to the next Inferior Conjunction phase in January. Years of Inferior conjunction of Venus in January are indicated in the first column.

Year of Inferior Conjunction of Venus in January	Venus Rainfall Cycles
1950	1950-1957
1958	1958-1965
1966	1966-1973
1974	1974-1981
1982	1982-1989
1990	1990-1997
1998	1998-2005
2006	2006-2013
2014	2014-2021

Table 5 shows rainfall cycles based on time taken by the planet Venus in its orbital motion to move from Inferior Conjunction phase in January to the next Inferior Conjunction phase in January. Years of Inferior conjunction of Venus in January are also indicated in the first column (A comprehensive summary of the inferior and superior conjunction dates of Venus is provided in Table 15 and Table 17, in Annex 2). The length of this cycle is 8 years and is referred to

hereafter as the “Venus rainfall cycle”. It is true that this cycle has been known to exist in annual rainfall in some parts of the world since the beginning of the 20th century (Moore,1921; Naidu, 1999).

Table 6: Rainfall cycles based on time taken by the Saturn in its orbital motion to move from opposition phase in January to the next opposition phase in January. Years of opposition of Saturn in January are indicated in the first column.

Year of Opposition of Saturn in January	Saturn Rainfall Cycles
1946	1946-1975
1976	1975-2004
2005	2005-2034

Table 6 shows rainfall cycles based on time taken by the Saturn in its orbital motion to move from opposition phase in January to the next opposition phase in January. Years of opposition of Saturn in January are indicated in the first column. (see a comprehensive summary of the opposition dates of Saturn, Table 22, in Annex 2). The length of this cycle is about 30 years and is referred to hereafter as the “Saturn rainfall cycle”. This cycle has been detected in some parts of the world like India (Naidu, 1999).

Table 7 : Rainfall Cycles based on time taken by the Jupiter in its orbital motion to move from opposition phase in January to the next opposition phase in January. Years of opposition of Jupiter in January are indicated in the first column.

Year of Opposition of Jupiter in January	Jupiter Rainfall Cycles
1943	1943-1954
1967	1967-1978
1955	1955-1966
1979	1979-1991
1991	1991-2002
2002	2002-2013
2014	2014-2025

Table 7 shows rainfall cycles based on time taken by the Jupiter in its orbital motion to move from opposition phase in January to the next opposition phase in January. Years of opposition of Jupiter in January are indicated in the first column (A comprehensive summary of the opposition dates of Jupiter are provided in Table 16, in Annex 2).

Table 8 shows rainfall cycles based on time taken by the Mars in its orbital motion to move from opposition phase in January to the next opposition phase in January. Years of opposition of Mars in January are indicated in the first column. (see a comprehensive summary of the opposition and conjunction dates of Mars, Table 20 and Table 21, in Annex 2). The length of this cycle is about 15 years and is referred to hereafter as the "Mars rainfall cycle".

Table 8: Rainfall Cycles based on time taken by the Mars in its orbital motion to move from opposition phase in January to the next opposition phase in January. Years of opposition of Mars in January are indicated in the first column.

Year of Opposition of Mars in January	Mars Rainfall Cycles
1948	1948-1962
1963	1963-1978
1978	1978-1993
1993	1993-2008
2010	2010-2025

In summary, the rainfall cycles generated in the discussion above have the following average time lengths that are determined through averaging of the periods in the cycles given in Tables 5, 6, 7 and 8 to a summary given in Table 9.

Table 9: Planets considered and the average planet rainfall cycle time span. Two additional planets; Uranus and Neptune have been added and the cycle time span is taken as the sidereal period of the planets.

Planet	**Period of the Rainfall Cycle**
Venus	95.9 months (~8 years)
Jupiter	144.13 months (~12 years)
Mars	179.5 months (~15 years)
Saturn	360.23 months (~30 years)
*Uranus	~996 months (~84 years)
*Neptune	~1957 months (~164 years)

* Sidereal Periods are used as cycle periods

5.3.2 *Results from Sinusoidal Models by Curve Fitting*

The methods employed in the curve fitting exercise in this Sub-section are discussed in sub-Section 4.2.7. When the average rainfall variations are determined in each rainfall cycle, as

outlined in the Section 5.3, now there was need to create and display models to represent the rainfall in the cycles discussed. The models were fitted by a non-linear least squares estimation using a combination of sine functions.

Results presented in this sub-section, show the variation of the mean monthly rainfall anomalies ($\overline{RR_{\psi}}$) and the fitted curve (RR_{ψ}) for every planet (ψ) in all the 12 zones (The figures are given in the Annex 1). A statistical summary of the relationship between the two is given for each of the models to show the significance of the relationship (The summaries for each model are given in the Annex 1). The variables; $RR_{♄}$, $RR_{♃}$, $RR_{♂}$, and $RR_{♀}$ represent estimated rainfall anomaly associated with the Saturn, Jupiter, Mars and Venus rainfall cycles respectively in each of the twelve zones.

5.3.3 *Temporal Variation of the Anomalies in the Rainfall Cycles*

From the graphs, (Annex 1) there are certain rainfall anomaly variations that make unique formations as one transits from period to period and from one zone to the other.

Figure 18 shows the variation of the mean Rainfall Anomaly (mm/day) in Zone I in the Saturn 30-year cycle beginning at observations of Saturn in Opposition phase in January (in which t is equal to zero). In Zone I, the rainfall cycle of Saturn shows a period of high positive values from the 80th month (7th year) to about 200th month (16th year) after opposition phase followed by a period of negative anomalies from the 200th month. Significantly lower values are noted from about 290th month (24th year) to 361st month (30th year) at the end of the cycle.

However, other rainfall features in the rainfall cycles of Saturn deduced from other zones show a slightly different behaviour. In general, most of the zones show positive anomalies in the whole region in the first 80 months (~7 years) of the Saturn cycle after Opposition phase in January. Between 80 and 200 months (~7 to 17 years) after opposition in January, significantly positive anomalies are found in zones I, II, III, X, XI and XII which cover mainly the northern half of the study area while the rest of the area has small to large absolute values of negative anomalies.

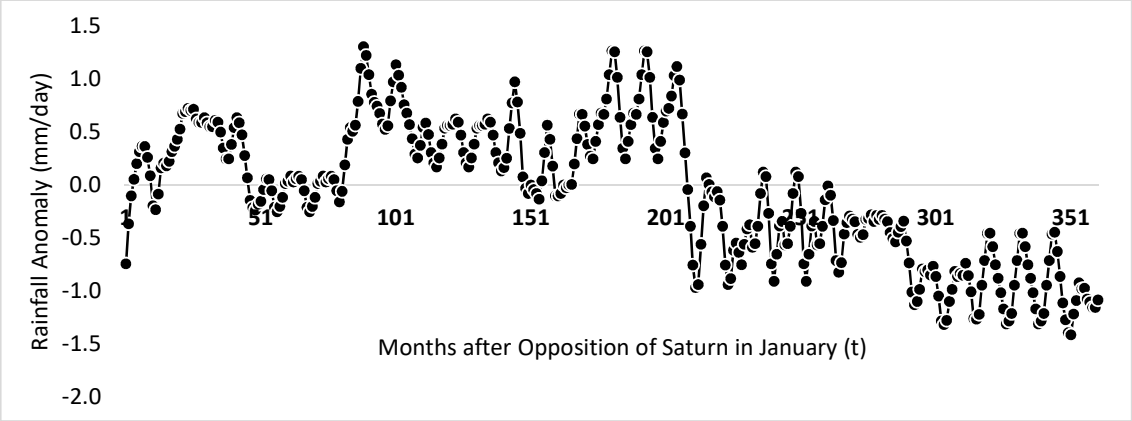

Figure 18 : Variation of the mean Rainfall Anomaly (mm/day) in Zone I in the Saturn 30-year cycle beginning at observations of Saturn in Opposition phase in January (t =1).

Between 200 to 270 months (~17 to 23 years) after opposition in January, the reverse occurs where the northern half has negative anomalies while the rest of the study area has positive anomalies. The last seven years of the cycle or about 23-30 years after the opposition in January, is characterised by negative anomalies in the whole region.

Similarly, other rainfall cycles show quite familiar features like the case above. Figure 19 is such one example. More information is provided in Annex 1.

Figure 19 shows the variation of the mean Rainfall Anomaly in Zone X in the Jupiter 12-year cycle beginning at Jupiter in Opposition phase in January. The graph shows a period up to about 90th month (~7.5 years) after opposition of the Jupiter in January which is dominated by negative anomalies but interrupted by few cases of positive anomalies. After the 90th month, the rest of the period up to the end of the Jupiter cycle is dominated by positive anomalies.

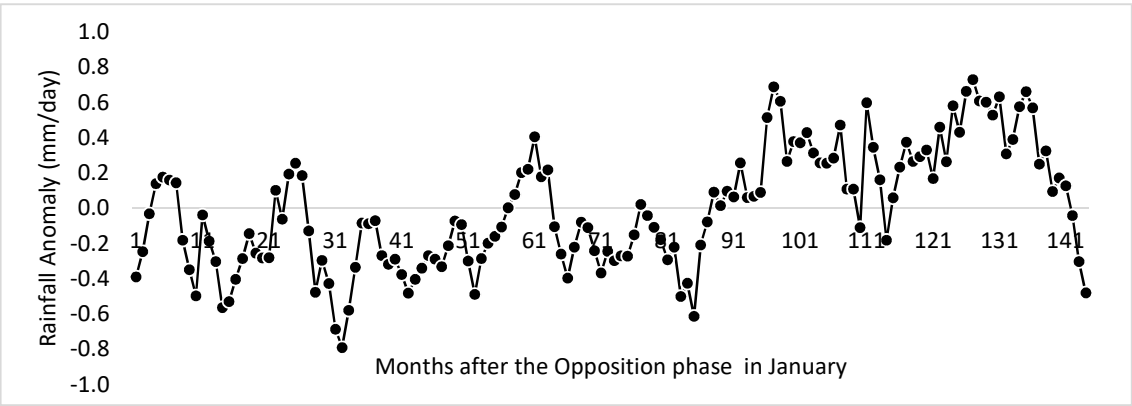

Figure 19 :Variation of the Mean Rainfall Anomaly (mm/day) in zone X in the Jupiter 12-year cycle beginning at Jupiter in Opposition phase in January.

The other zones have nearly the same characteristics as Zone X. Generally, the period 30 to 50 months (~2 to 4 years) after the opposition of Jupiter in January, most of the zones are characterised by negative anomalies. There are positive anomalies from the 7th year to the end of the cycle.

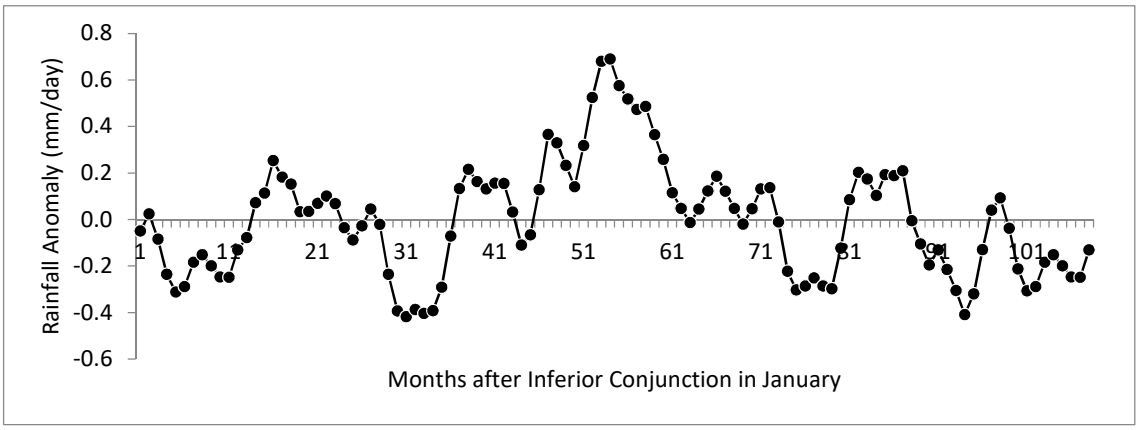

Figure 20 : Variation of the mean Rainfall Anomaly (mm/day) in zone II in the Venus 8-year cycle beginning at Venus in Inferior conjunction phase in January.

Figure 20 shows the variation of the mean Rainfall Anomaly in zone II in the Venus 8-year rainfall cycle beginning at Venus in inferior conjunction phase in January. From the graph, positive anomalies are clearly noted between 40 to 60 months after the inferior conjunction phase in January. These features are exhibited in some of the zones while in others there is a little deviation. In this case, most of the zones have positive anomalies in the periods 45 to 60 months and 75 to 96 months (~ 4 - 5 years and ~ 6 - 8 years) after the inferior conjunction in January. The first two years after the conjunction are characterised by negative anomalies in most areas.

Figure 21 shows variation of the mean Rainfall Anomaly in zone IX in the Mars 15-year cycle beginning at Mars in Opposition phase in January. The Mars Rainfall cycles have characteristics close in resemblance to the Saturn cycles where the cycle begins with positive anomalies before it drops to the negative values the rest of the cycle. For example, the variation shown in Figure 21 has positive anomalies in the beginning up to about 50 months (~ 4 years) after opposition in January for most zones.

However, afterwards most zones start showing negative anomalies especially in zones I, II, III, IV, VI and VIII which represent the dry lowlands of the study area. The negative anomalies

are more pronounced between 110 and 150 months (or 9 to 12 years) after the opposition in January.

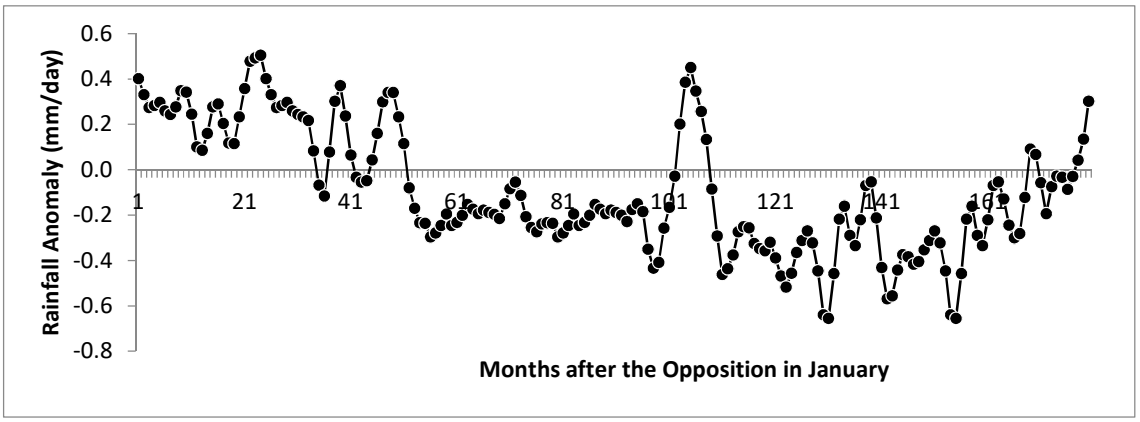

Figure 21 : Variation of the mean Rainfall Anomaly (mm/day) in zone IX in the Mars 15-year cycle beginning at Mars in Opposition phase in January.

Some other cycles that have been noted to exhibit unique characteristics are, for example, those that have variations that swing from one extreme to an opposite extreme as one goes along the cycle. Figure 22 shows the variations of the anomalies in a Jupiter rainfall cycle as a good example.

Figure 22 shows variation of the mean Rainfall Anomaly in Zone XI in the Jupiter 12-year cycle beginning at Jupiter in Opposition phase in January. From the graph, we see the difference between the maximum and the minimum values in the beginning of this cycle as small especially during the period 10 to 30 months. Afterwards the difference increases to large swings but the difference drops off steadily towards the end of the cycle.

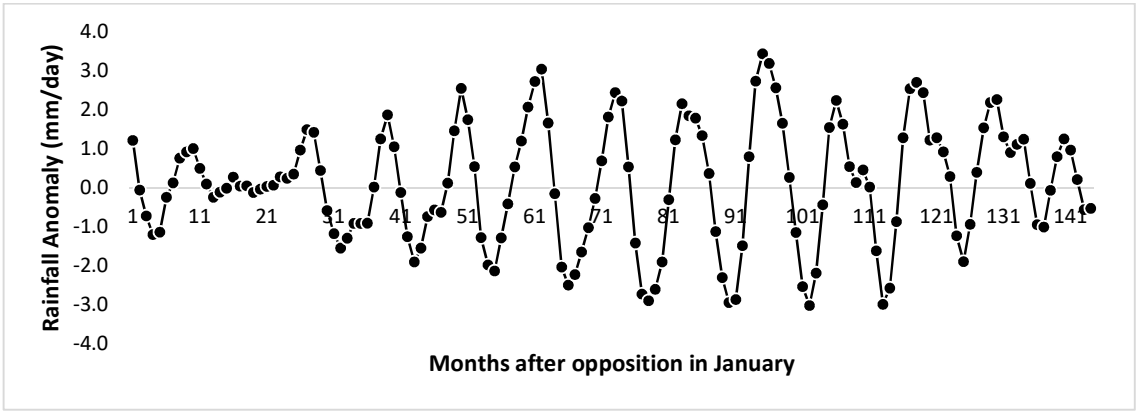

Figure 22: Variation of the mean Rainfall Anomaly (mm/day) in Zone XI in the Jupiter 12-year cycle beginning at Jupiter in Opposition phase in January.

5.3.4 *Results from Multiple Linear Regression Models*

Models generated in this sub-section have inputs from the models on rainfall cycles discussed in the previous sub-sections. The inputs are predictor variables, in this case $RR_{♄}$, $RR_{♃}$, $RR_{♂}$, and $RR_{♀}$ that represent estimated rainfall anomalies associated with the cycles of Saturn, Jupiter, Mars and Venus rainfall, respectively, in each of the zones. Each one of the predictor variables can be determined by varying the time and is calculated from the time of opposition or conjunction phase of each planet (as shown in Figures in Annex 1). The multiple linear regression model, RR, is a function of the predictor variables; $RR_{♄}$, $RR_{♃}$, $RR_{♂}$, and $RR_{♀}$. Equation 56, which is a model, shows the variation of RR for zone V given as;

$$RR(t) = 0.431 * RR_{♄}(t) - 0.167 * RR_{♀}(t) - 0.196 * RR_{♃}(t) + 0.526 * RR_{♂}(t) \quad (56)$$

Figure 23 shows the variation of the model and the actual Rainfall Anomaly for Zone V. A simple sine curve is fitted to the actual rainfall anomaly. The graph shows the variation of the zone V model plotted against the actual rainfall anomalies. Visually examining the two curves, certain important observations are made. While the two curves seem to be compatible and consistent with each other, there are certain parts of the curves representing the two quantities that do not fit right. The last 10 years (about the year 2008 to 2017) appear to be a period when the model overestimates while the middle period (mainly the 1960s, 1970s and 1980s) are underestimated. This confirms the overestimation problem in GHACOF forecasts in the verification study of Mason and Chidzambwa (2008).

By fitting a sine curve to the actual rainfall anomaly, the sine curve reveals a variation with a periodicity of about 85 years that is not inherent in the model. The curve has a maximum value in about 1977 and a minimum falls just about the end of the training period, 2017, or thereafter. This variation of the actual rainfall anomaly coincides with the 84-year rainfall cycle of Uranus in which planet Uranus was in opposition in approximately the year 1951 and in the conjunction phase with the Sun in 1993. The maximum occurs about 26 years after the opposition and the minimum occurs about 26 years after conjunction. From that observation, the variation of the actual anomalies can be attributed to the orbital motion of the Uranus.

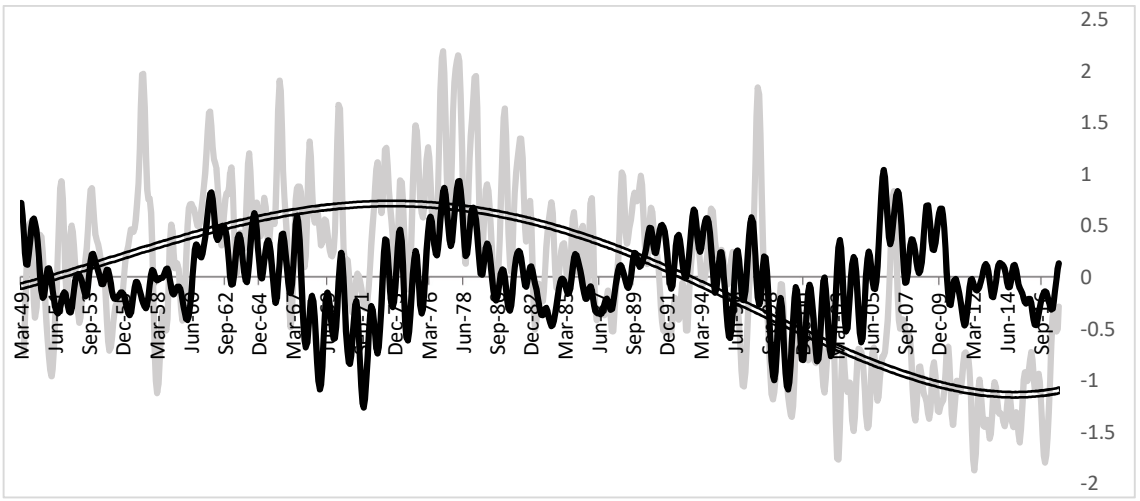

Figure 23: The variation of the model $\boldsymbol{RR(t)}$ (black curve) and the Rainfall Anomaly $\boldsymbol{RR(t)}$ (grey curve) for Zone V. A simple sine curve is fitted to the actual rainfall anomaly. The model is fitted with a line that passes through the x-axis.

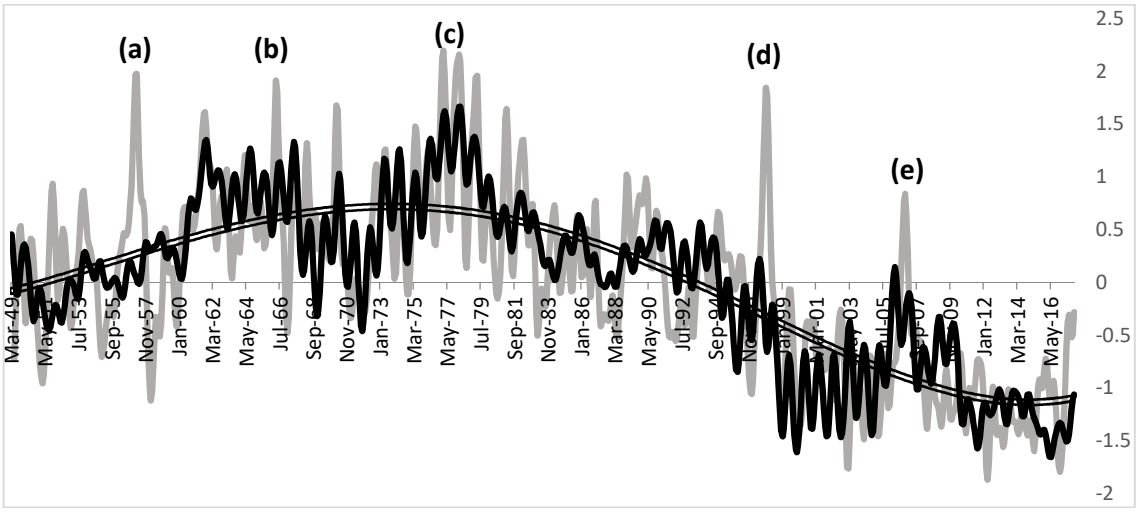

Figure 24: The variation of the model $\boldsymbol{RR(t)}$ (black curve) and the Rainfall Anomaly $\boldsymbol{RR(t)}$ (grey curve) for Zone V. A simple sine curve is fitted to the rainfall anomaly. The model is corrected by the use of the given sine curve to fit it into the actual rainfall anomaly curve.

If we now correct the variation of the model by including the Uranus rainfall cycle, this results in the variation of a new integrated model in Figure 24.

Figure 24 shows the variation of the model and the actual Rainfall Anomaly for Zone V. A simple sine curve is fitted to the rainfall anomaly.

Clearly, from the graph (Figure 24), the two quantities are now more consistent than before correction except for a few conspicuous data points that seem to exhibit outlier characteristics. These points marked a, b, c, d and e (in Figure 24) which represent the years 1957, 1966, 1977-78, 1997-98 and 2006-07 respectively are associated with some of the major El-Nino events between 1948 and 2017. This may mean that the astronomical indicators are not sensitive to El-Nino events and cannot be used to model their occurrence.

5.3.5 *Past Climate Scenarios and the Model*

One way of verifying qualitatively if the models have any skill especially on long range variability is to examine past climate scenarios outside the training period, 1948-2017. In this sub-section, we used the zone V because there is reliable historical climate information in the area that can be used to compare with the variations of the corresponding model, zone V model (Equation 56) which is run from the year 1820 AD to 1899 AD.

Figure 25 shows the variation of the Zone V model from 1820 to 1899. The periods (a), (b), (c) and (d) indicated in the graph are periods of intense drought and famine events at the coast of East Africa which includes areas covered in zone V.

When the periods of notable negative and positive anomalies were distinguished, we noticed a cycle that developed further interest. To check if there was any consistency with the local climate conditions, we searched into the political histories of the communities in the area for any clue on extreme weather narratives and records especially on drought or famine that may have been generated by lack of rainfall.

We noted that periods (a), (b) and (c) were characterised by frequent dry conditions and tribal warfare not only in zone V but even in some other zones which means that the events were not localised but were widely felt even in other zones. The climate conditions in period (d) were not widespread but found to have been intense in some areas.

Period (a) may have lasted between 1836 and 1840 where a series of famines affected nearly the whole of the East African coast. Cases of people selling themselves as slaves for food were quite common in the area (Wrigley 1964; Lehman *et. al*. 2003; Nicholson, 2001).

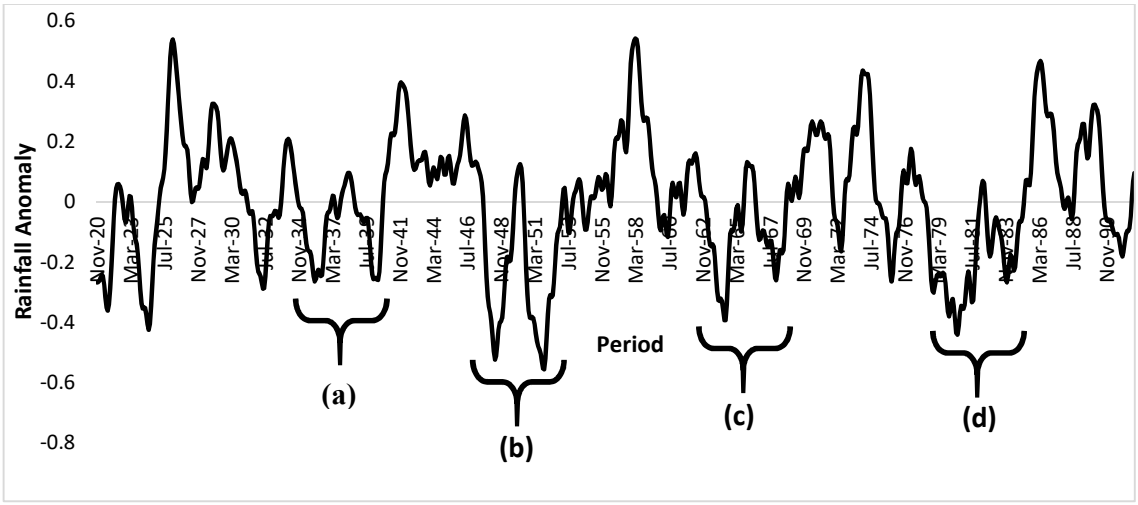

Figure 25 : The variation of the model $RR(t)$ from 1820 to 1899 for zone V. The periods (a), (b), (c) and (d) are periods of intense drought and famine at the coast of East Africa which includes areas covered in zone V.

Although not much is said about Period (b), one mention by a missionary, Dr. Krapf, in comments made in his diary, suggests of a severe drought in south eastern parts of Kenya in the 1860s. Period (c) was dominated by a series of famines at the coast in which most of the coastal people were affected. In particular, drought had ravaged the Bura people of coastal Kenya by 1862. Period (d) was equally severe in zone V where the *Mwakisengi* famine affected most of the coast and south eastern areas of Kenya (Merritt 1975).

From the climate conditions noted in Figure 25, there is a general inference that the conditions in the four periods do coincide with the negative anomalies hindcasted by the model. This further tells us that the model can be used to map out times of droughts and times of wetness by estimating the rainfall anomalies in the past.

However, it should be noted that the variations of the zone V model in Figure 25, do not include the sine curve correction discussed in sub-section 5.3.4. More knowledge on these corrections is obtained in the next sub-section.

5.3.6 *Climate Conditions Associated with Conjunctions of Uranus and Neptune*

While the ultimate model uses predictor models associated with Saturn, Jupiter, Mars and Venus, the other planets Uranus and Neptune have not been used because study data range would not allow.

In sub-section 5.3.4, we saw a clear consistent relationship between the orbital motions of Uranus and the actual rainfall anomalies through the fitted sine curve. Here, we examine the past climate conditions in the study area and beyond when the same or nearly the same Uranus-Neptune planet configurations were possible.

It is now evident and largely accepted that climate conditions in the area have been deteriorating due to decline in rainfall since the 1980s; however, in the region, the conditions have become far much worse since 1999 because of an abrupt decrease in rainfall after 1999 (Lyon *et. al.*, 2012). There have been more cases of below normal rainfall in the last 10 years than it was 30 years earlier. This decline has been attributed to a gradual increase in SSTs in the south-central Indian Ocean and west Pacific Ocean. In some other studies it has been attributed to changes in anthropogenic aerosol emissions, natural variability in the recent droughts and land-use change (Rowell et. al., 2015).

We further noted that 1993 is the year of conjunction of Neptune with the Sun and that from 1993 to 2018, which is about 25 years, subtends an angle slightly more than 50° from Earth-Sun Axis. Coincidentally, the year 1993 is the year of conjunction of Uranus with the Sun. Uranus takes about 13 years to subtend the same angle.

Figure 26 shows timelines of periods when the bodies Uranus, Neptune and the Sun form conjunctions. The conjunctions in consideration are Uranus-Sun Conjunction (square), Neptune-Sun Conjunction (diamond) and Uranus-Neptune Conjunction (triangle) all between 1478 and 2050 AD. The periods shaded in grey and indicated by (a), (b), (c) and (d) represent times of extreme aridity in the region. The periods have been selected based on longevity and intensity of local extreme events in the region mainly generated from political histories of the local communities in and around zone V.

From historical records, we were able to come up with three major drought-famine periods between 1478 and 1900 AD. All the three periods indicated by (a), (b), and (c) in Figure 26 coincided with planets conjunctions falling at the beginning of each of the periods. Period (d) is the period 1993-2018 and period (e) falls after 2018 for approximately 25 years assuming it goes by the same approximate time span of the other periods.

For comparison purposes, the three periods are described and compared to the current period to show similarities in climate conditions to the current climate conditions the study area is currently experiencing.

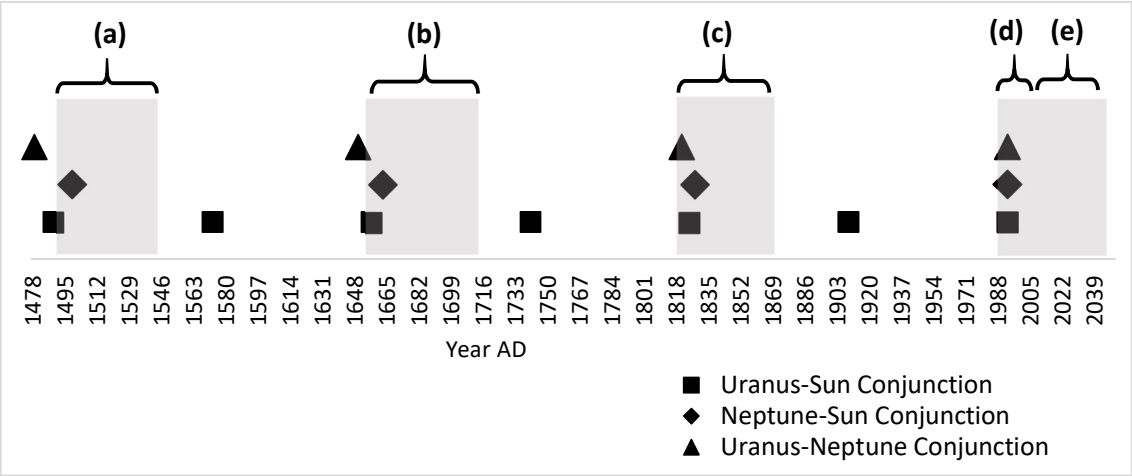

Figure 26 : Timelines of periods when the bodies Uranus, Neptune and the Sun form conjunctions; Uranus-Sun Conjunction (square), Neptune-Sun Conjunction (diamond) and Uranus-Neptune Conjunction (triangle) all between 1478 to 2050 AD. The periods shaded in grey and indicated by (a), (b), (c) and (d) represent times of extreme aridity in the region. The periods have been selected based on longevity and intensity of local extreme events in the region mainly generated from political histories of the local communities in and around zone V.

In period (a), there were widespread drought and famine conditions which brought about great disorder in the whole region. The region was hardest hit in the 1530s and 1540s and it seems to have had more effect in neighbouring countries like Ethiopia and Somalia. Large migrations were common in the whole of East Africa with communities moving to higher grounds or safer areas. Nile flood records showed low levels of the Nile confirming dry condition in the region (Toussoun, 1925; Lamb, 1966)

Period (b), was characterised by drying rivers and lakes, for example lake Naivasha was evidently low during 1670-1680 (Verschuren, 2000). Movements of mt. Kenya communities uphill between 1650 and 1750 with communities raiding and fighting was quite common (Muriuki, 1969). Engaruka and Pangani valley settlements in Tanzania were decimated when water supply dwindled and may have completely disappeared around 1670-1690 when most of the region was under a severe famine (Ryner *et. al*., 2002). In general, most of the region was considered severely dry about the period 1670-1730.

The third, period (c), was characterised by tribal warfare and widespread conflict where thousands were killed by combined effect of conflict and starvation. It was considered a disaster by most communities and is remembered by some up to date because of its severity (Mwaniki, 1982; Herrings, 1979). Dry conditions were quite frequent in 1840s, 1850s and 1860s with rivers and lakes drying up, for example, lake Naivasha was at its lowest since 1250 AD and it

had been reduced to a paddle by 1845 (Nicholson, 2001; Verschuren, 2000). A number of areas were littered with environmental refugees who became easy target for slave raiders.

Both Period (d) and (e) are in the fourth cycle of the Uranus-Neptune orbital motions and while (d) is in the period 1993-2018, period (e) is in the period 2018-2043.

The coincidences from the three periods cannot be ignored. If the history of the other cycles is anything to go by, then we are likely to have poor climate conditions as a result of lack of enough rainfall and we are likely to have even drier conditions in approximately 25 years starting 2018 which falls in period (e).

5.4 Results of the Variation of Probabilities of Rainfall Exceedance or Occurrence

The probability of exceedance refers to the chance of the occurrence of rainfall values exceeding some given value $RR\ mm$. The probability of exceedance $P[X > RR]$ is expressed in equations (46) and (47) and by using thresholds given in Table 10, where six categories, based on different levels of severity, are generated. The categories currently in use in our forecasts are Normal, Below Normal and Above Normal (based on terciles). However, the new categories include the levels: Extreme Low, Extreme High and Phenomenal (based on standard deviation). To avoid confusion in understanding the categories, "Above Normal" range also includes Extreme High and Phenomenal, "Extreme High" range also includes Phenomenal and Below Normal range includes "Extreme Low".

Table 10 : A list of categories and the corresponding probabilities based on the Standard Deviation. Z is the normalized values of RR and the σ is the Standard Deviation.

Categories	Probability of Occurrence
Phenomenal	$P[Z > 2\sigma]$
Extreme High	$P[Z > \sigma]$
Above Normal	$P[Z > 0.5\sigma]$
Normal	$P[-0.5\sigma < Z < 0.5\sigma]$
Below Normal	$P[Z < -0.5\sigma]$
Extreme Low	$P[Z < -\sigma]$

Results in this sub-section focus on the Saturn phases in zone XII where the results of probability of occurrence through the year (January-December) are exhibited when Saturn is observed in opposition separately in June and July.

Table 11: Table of Probability of occurrence (%) of Monthly Rainfall in the given classes in Zone XII when the Saturn is observed at Opposition in the month of June. Bolded figures are the focus of our discussions.

	Jan	Feb	Mar	Apr	May	Jun	Jul	Aug	Sep	Oct	Nov	Dec
PHENOMENAL	33	33	17	0	17	17	0	0	0	0	0	0
EXTREME HIGH	50	50	**50**	**33**	**33**	33	0	0	0	0	0	0
ABOVE NORMAL	50	67	**67**	**50**	**50**	33	0	17	17	17	17	0
NORMAL	33	17	0	17	50	33	83	67	17	0	50	100
BELOW NORMAL	17	17	33	33	0	33	17	17	67	**83**	**33**	0
EXTREME LOW	0	0	0	33	0	0	0	0	17	0	0	0

Table 11 gives the Probabilities of occurrence of Monthly Rainfall in the given classes for Zone XII when the Saturn is in Opposition phase in the month of June. In general, for Table 11, there are relatively higher probabilities between January and June under the categories “above normal” and “extreme high” and between September and November under “below normal” category.

In 2018, Saturn was in Opposition phase in June. The probabilities in Table 11 represent what the situation would be in any year when Saturn is observed in Opposition phase in the month of June.

The above results show consistency with the situation in MAM and OND 2018 seasons when zone XII was exposed to two opposite rainfall extremes. The rainfall conditions of MAM 2018 season were fairly wet throughout the period which had begun at the end of February. The exceptionally heavy rainfall resulted in extensive flooding with the loss of lives and property, displacement of population, major disruption of livelihoods and damage to infrastructure (Kilavi *et. al.*, 2018) while the conditions of OND 2018 season were extremely dry leading to extensive crop failures (FEWSNET, 2018).

An assessment of the probabilities in Table 11 during the period MAM shows relatively high values of up to 67% under “Above Normal” and “Extreme High” while the period OND shows high values of up to 83% under the category “Below Normal”.

The situation is much clearer when we consider the Probability Anomalies given in Table 12 which are determined from Table 11 by use of the Equation (51). Table 12 gives the Probabilities Anomalies of Monthly Rainfall in the given classes for Zone XII when the Saturn is in Opposition phase in the month of June.

From the table, the MAM season is dominated by positive anomalies of up to 33% under "Above Normal" and in the OND season, up to 58% under "Below Normal" category. These 2018 seasons performances were well captured by the probabilities.

Table 12: Table of Probability Anomaly (%) in the given classes in Zone XII when the Saturn is at Opposition in the month of June. Bolded figures are the focus of our discussions.

	Jan	Feb	Mar	Apr	May	Jun	Jul	Aug	Sep	Oct	Nov	Dec
PHENOMENAL	26	23	12	-4	11	9	-7	-6	-4	-7	-9	-13
EXTREME HIGH	31	28	**29**	**10**	**14**	11	-21	-18	-21	-18	-25	-25
ABOVE NORMAL	21	33	**33**	**12**	**21**	-2	-28	-11	-17	-13	-22	-29
NORMAL	-14	-27	-34	-11	1	-11	30	11	-23	-46	3	34
BELOW NORMAL	-7	-5	1	0	-22	13	-2	0	**40**	**58**	**19**	-4
EXTREME LOW	0	0	-16	22	-4	0	0	0	11	-1	0	0

Table 13: Table of Probability of occurrence (%) of Monthly Rainfall in the given classes in Zone XII when the Saturn is observed at Opposition in the month of July.

	Jan	Feb	Mar	Apr	May	Jun	Jul	Aug	Sep	Oct	Nov	Dec
PHENOMENAL	17	33	0	0	0	17	0	0	0	17	0	17
EXTREME HIGH	33	33	17	33	33	33	17	33	17	33	17	50
ABOVE NORMAL	33	67	33	33	50	33	33	50	33	33	50	50
NORMAL	67	17	50	50	17	17	33	50	50	33	50	50
BELOW NORMAL	0	17	17	17	33	50	33	0	17	33	0	0
EXTREME LOW	0	0	0	0	0	0	0	0	0	0	0	0

Table 13 gives the Probabilities of occurrence of Monthly Rainfall in the given classes for Zone XII when the Saturn is in Opposition phase in the month of July. The probabilities in Table 13 represent the situation in any year when Saturn is observed in Opposition phase in the month of July. In 2019, the opposition of Saturn was in July and Table 13 may represent the probability variations of 2019.

Table 14 gives the Probabilities Anomalies of Monthly Rainfall in the given classes for Zone XII when the Saturn is in Opposition phase in the month of July. The bolded figures in the in the MAM season indicates relatively higher probability Anomalies in the months of April and May under the "Extreme High" category while it is relatively higher in March under the "Normal" category. This can be interpreted to mean that the rainfall in the zone XII started off at normal levels in March and then pick up in April and May 2019.

Table 14: Table of Probability Anomaly (%) in the given classes in Zone XII when the Saturn is at Opposition in the month of July. Bolded figures are the focus of our discussions.

	Jan	Feb	Mar	Apr	May	Jun	Jul	Aug	Sep	Oct	Nov	Dec
PHENOMENAL	9	23	-4	-4	-6	9	-7	-6	-4	**9**	-9	**3**
EXTREME HIGH	14	11	-4	**10**	**14**	11	-4	16	-4	**16**	-8	**25**
ABOVE NORMAL	4	33	0	-5	**21**	-2	5	22	0	**4**	**12**	**21**
NORMAL	20	-27	**16**	22	-32	-27	-20	-6	10	-12	3	-16
BELOW NORMAL	-24	-5	-16	-17	11	29	14	-16	-10	8	-15	-4
EXTREME LOW	0	0	-16	-12	-4	0	0	0	-6	-1	0	0

A report by a Kenya Food Security Steering Group (KFSSG) on the assessment of the "Long Rains" season 2019 indicated that the rains delayed in some areas with the onset coming in the month of April (KFSSG, 2019). Although the report targeted the ASAL areas, the zone XII covers part of the ASAL areas around it and so it can represent the general situation in the area. Comparing the variation of the probabilities in Table 14 and the KFSSG report leads me to conclude that there is consistency between them.

CHAPTER SIX: SUMMARY, CONCLUSIONS AND RECOMMENDATIONS

6.1 Summary

This study focused on astronomical observations that relate to monthly rainfall recorded in East Africa. It has three objectives one of which is to test whether the orbital motions of the celestial bodies have any effect on the rainfall over East Africa. The others are to develop models with temporal variations or the intra-seasonal-to-interannual variability of rainfall and to determine the occurrence of rainfall extremes.

To easily understand the concept behind this study, a motion geometry of the planets was designed based on whether a planet has an outer or an inner orbit in reference to the Earth's orbit. The moon's motion geometry was also considered. From these geometries, gravitational forces exerted by the planets were determined and compared to the key phases of the planets. The maximum and minimum values of the forces coincided with the key phases of the planets. Results generated show that the orbital motions of Saturn, Jupiter, Venus and Mars have a relationship with the monthly rainfall.

Both MAM and OND rainfall seasons seem to show a variation from year to year that indicates strong astronomical influence. We also noted that rainfall characteristics during two similar phases of a planet but which occur at different times of a year are different. Rainfall characteristics associated with the same observed phase of a planet and in the same month or corresponding period of another year were found to be nearly the same. To get to the same phase in the same month of the year, it takes Saturn 30 years, Jupiter 12 years, Mars 15 years and Venus 8 years. That means that the East African rainfall varies in cycles of 8, 12, 15 and 30 years.

As a result, a curve fitting exercise was done to the mean rainfall anomalies developed based on the cycles between 1948 and 2018 for individual planets. Subsequently, a sinusoidal model was created for each planet and in each zone.

Further, by using historical climate information, it was found out that severe climate extremes occur during a period of approximately 50 years beginning just about the conjunctions of both Uranus and Neptune with the sun where Uranus takes ~84 years and Neptune takes ~164 years to orbit to the next conjunction. These periods were thereafter called Uranus rainfall cycle and Neptune rainfall cycle. We attributed the variations of the historical climate extremes since 1821 AD to the two planets' orbital motions.

The probabilistic models developed in this study used probability of occurrence and have five categories; “Extreme Low”, “Below Normal”, “Normal”, “Above Normal”, “Extreme High” and “Phenomenal”. The use of the three new categories, not used before in the past, that is, “Extreme Low”, “Extreme High” and “Phenomenal” provides an opportunity to determine the occurrence of extreme rainfall. By using the Zone XII model on 2018 rainfall seasons, a qualitative verification process indicated relatively good results for both seasons which indicates that the models can be used for prediction.

6.2 Conclusions

Generally, from the results, it was found out that the planets have a relationship with the East African rainfall. Each one of them showed a certain level of contribution to the variation of monthly rainfall with the Planet Saturn indicating the biggest influence. The variation of monthly rainfall due to the orbital motions of the Moon shows low values of one order of magnitude lower than those of the planets in all zones which means its influence in the monthly rainfall is also small. The moon has relatively little influence to the monthly rainfall variation compared to the planets. It means that the phases of Saturn can be used to determine monthly rainfall in an area while the moon phases cannot be useful in the monthly rainfall determination.

The rainfall cycles are based on orbital cycles of the planets which are easily determined by use of their key phases. The phases can be predicted by use of astronomical calculations with little error and with sufficient accuracy way ahead of time. Similarly, the phases can be hindcasted back in time by the same calculations to allow a dependable determination of rainfall variation of the past. In general, the use of these astronomical phases can be used to generate past and future climate scenarios in the region that can add useful body of knowledge to climate science.

Probability of exceedance/ Occurrence of rainfall can be used to determine periods of high or low probability of extreme rainfall in any of the zones with some degree of skill. The six categories generated have one more category added, Phenomenon, which may include extreme rainfall in forecasting.

We can finally conclude that the orbital motions of the moon and planets have an influence on the rainfall and that the rainfall extremes are favoured by certain phases of the planets. The occurrence of these extremes is also astronomically influenced.

6.3 Recommendations

During the course of this study, there are many assumptions made. Most of these assumptions were mainly in the field of astronomy and this may have hindered a more analytical examination of the astronomical indicators. An input into this study from the field of astrophysics would enrich it. It is recommended that the future expansion of this work to include an input from astrophysics and atmospheric physics to give it a comprehensive analysis.

One of the reasons for including the disciplines, astrophysics and atmospheric physics is that they can inject other aspects of astronomical and atmospheric influences that may come into our atmosphere. One of them is the influence that may come from perturbing forces from known and unknown sources within or outside the solar system.

It should be noted that throughout the course of this study, the Sun's influence was not factored in. We know that the Sun is the source of the Earth's radiant energy and that the Sun's gravity far exceeds that of the moon and the planets. It is recommended that the Sun's gravitational forces, the radiant energy and associated factors be included in future studies.

The study was also done within very tight timelines and may not have allowed enough time for in-depth analysis of the subject. As the study has highlighted many areas of expansion, gaps that require bridging and limitations encountered, a little more time should be given to go much deeper into this line of research.

All the above can only be done if the funding agencies allocate more resources for research. I encourage the policymakers to give this area of study a little more attention as it is emerging as a promising and better way of dealing with climate prediction.

A great deal of effort is required to sensitise the users of the weather and climate information on the scientific influence of the planets and the moon on seasonal rainfall in East Africa. This will demystify the misunderstanding that the influences from the stars emanate from the spirit world. This will also make the user appreciate more the products that come from a process that has an input from watching the skies.

REFERENCES

Adams, W.M. (1996) Lakes. In: Adams W, Goudie A, Orme A (eds). The physical geography of Africa. Oxford University Press, Oxford pp.122-133

Alexander, L. V., X. Zhang, T. C. Peterson, J. Caesar, B. Gleason, A. M. G. Klein Tank, M. Haylock, D. Collins, B. Trewin, F. Rahimzadeh, A. Tagipour, K. Rupa Kumar, J. Revadekar, G. Griffiths, L. Vincent, D. B. Stephenson, J. Burn, E. Aguilar, M. Brunet, M. Taylor, M. New, P. Zhai, M. Rusticucci and J. L. Vazquez-Aguirre, (2006) Global observed changes in daily climate extremes of temperature and precipitation, *J. Geophys. Res*.,**111**

Anyah, R. O., and F. H. M. Semazzi, (2007) Variability of East African rainfall based on multiyear RegCM3 simulations. *International Journal of Climatology*, **27**:pp357–371

Balkema, A., and de Haan, L. (1974) Residual life time at great age, *Annals of Probability*, **2**, pp792–804.

Balling, R. C., Jr., and Cerveny, Randall S. (1995) Influence of Lunar Phase on Daily Global Temperatures, *Science*, **267**:pp1481

Beirlant, J., Goegebeur, Y., Segers, J. and Teugels, J., (2004) Statistics of Extremes, *Theory and Applications*, Wiley.

Benedict, Ruth, (1935) *Zuni Mythology*. Columbia University Contributions to Anthropology, no. 21. New York: Columbia University Press. AMS Press reprint, 1969.

Boko, M.I, Niang, A., Nyong, C., Vogel, A.,Githeko, M., Medany, B., Osman-Elasha, Tabo,R. and Yanda, P. (2007) Africa climate change 2007: Impacts, adaptation and vulnerability. Contribution of Working Group II to the Fourth Assessment Report of the Inter-governmental Panel On Climate Change. pp.433-467.

Bradley D. A, Woodbury M. A and Brier G. W. (1962) Lunar Synodic Period and Widespread Precipitation. *Science* **137**: No. 3522, pp. 748-749.

Brier G. W. and Bradley D. A. (1964) The Lunar Synodic Period and Precipitation in the United States. *Journal of the Atmospheric Sciences*. **21**: No. 4, pp.386-395.

Briggs, J., & Moyo, B. , (2012) The Resilience of Indigenous Knowledge in Small-scale African Agriculture: Key Drivers. *Scottish Geographical Journal*, **128**(1): pp64-80.

Chapman, S. (1918) The lunar atmospheric Tide at Greenwich, 1854-1917. *Quart. J. Roy. Meteor. Soc*., **44**, pp271-280

Charvatova I., (2000) Can origin of the 2400-year cycle of Solar activity be caused by Solar Inertial Motion. *Ann. Geophysicae* **18**: pp399-405.

Chengula F. and B. Nyambo, (2016) The significance of indigenous weather forecast knowledge and practices under weather variability and climate change: a case study of smallholder farmers on the slopes of Mount Kilimanjaro. *International Journal of Agricultural Education and Extension* Vol. **2**(2), pp 31-43

Chidzambwa, S., & Mason, S. J., (2008) Report of the valuation of Regional Climate Outlook Forecasts for Africa during the Period 1997-2007. ACMAD *Technical Report*, Niamey, ACMAD.

Climdex, (2012) Datasets for Indices of Climate Extremes. https://www.climdex.org/indices.html (Accessed on 31 March 2018)

Coles, S, G. (2001) *An Introduction to Statistical Modelling of Extreme Values*, Springer. pp 208

Crawford E. A., (1989) The Lunar Garden: Planting by the Moon Phases (NY, NY: Weidenfeld & Nicholson), pp 9-50.

Cushing, Frank Hamilton, Barton Wright, (1992) *The Mythic World of the Zuni*, University of New Mexico Press, hardcover, ISBN 0-8263-1036-2.

Davison, A. C. and Smith, R. L., (1990) Models for exceedances over high thresholds. *Journal of the Royal Statistical Society*. Series B (Methodological), pp 393–442.

Desalegn A., M. Radeny and C. Mungai, (2017) Indigenous knowledge in weather forecasting: Lessons to build climate resilience in East Africa. https://ccafs.cgiar.org/news/indigenous-knowledge-weather-forecasting-lessons-build-climate-resilience-east-africa-0#.Wq0J3n--mpo (accessed on 18 March 2018)

DeSilva R. P., N.D.K. Dayawansa and M. D. Ratnasiri , (2007) A comparison of methods used in estimating missing Rainfall data. *The Journal of Agricultural Sciences*, 2007, vol.**3**, no.2.

Dube, M. A., & Musi, P. J., (2002) Analysis of Indigenous knowledge in Swaziland: Implications for Agricultural Development. *African Technology Policy Studies Network*., Nairobi, Kenya.

Eddington, A. S. (1922) The Propagation of Gravitational Waves. *Proceedings of the Royal Society of London* **A102**, pp268-282.

Ender, M. and Ma, T., (2004) Extreme Value Modelling of Precipitation in Case Studies for. *International Journal of Scientific and Innovative Mathematical Research*, **2**(1): pp23–36.

FEWSNET (2018) East Africa Food Security Alert. Famine Early Warning System Network. https://reliefweb.int/report/somalia/east-africa-food-security-alert-december-7-2018 (Last accessed 6 June 2019)

Funk, C., G. Senay, A. Asfaw, J. Verdin, J. Rowland, J. Michaelson, G. Eilerts, D. Korecha and R. Choularton, (2005) Recent drought tendencies in Ethiopia and equatorial-subtropical eastern Africa. Washington DC, FEWS-NET.

Frimpong, H. N., (2013) Indigenous knowledge and climate adaptation policy in northern Ghana, *Backgrounder*,**48**.

Gachari F., Mulati D. M., Mutuku J. N. (2013) Gravitational Atmospheric Tidal Potentials as Factors in Rainfall Modelling. *International Journal of Science and Technology* Vol. **2** No. 6, pp 446-456.

Garay-Barayazarra, G.; Puri, R., (2011) Smelling the monsoon: Senses and traditional weather forecasting knowledge among the Kenyah Badeng Farmers of Sarawak, Malaysia. *Ind. J. Trad. Knowl*. **10**: pp21–30.

Goddard, L., Aitchellouche, Y., Baethgen, W., Dettinger, M., Graham, R., Hayman, P., Conrad, E., (2010) Providing Seasonal-to-interannual Climate Information for Risk Management and Decision-making. *Procedia Environmental Sciences*, **1**, pp81-101.

Goudie, A.S. (1996) Climate: Past and Present. In Adams W, Goudie A, Orme A (eds). The physical geography of Africa. Oxford University Press, Oxford pp.34-59

Goulter S. W. (2005) The structure of the lunar semi-diurnal pressure tideL2. *Q. J. R. Meteorol. Soc*.(2005),**131**, pp723–758

Graham R., A. Colman, M. Vellinga and E. Wallace, (2012) Use of dynamical seasonal forecasts in the consensus outlooks of African Regional Climate Outlook Forums (RCOFs). ECMWF Seminar on Seasonal Prediction, 3-7 September 2012

Guiley R. E., (1991) The Lunar Almanac, London, *Piatkus*. P. pp147

Gugulethu Z, K. Stigter and S. Walker (2013) Use of Traditional Weather/Climate Knowledge by Farmers in the South-Western Free State of South Africa: Agrometeorological Learning by Scientists. *Atmosphere* 2013, **4**(4): pp383-410

Gutzwiller M. C. (1998) Moon-Earth-Sun: The oldest three-body problem. *Reviews of Modern Physics*, Vol. **70**: No. 2

Hart, T.G.B. (2007) Local knowledge and agricultural application: Lessons from an Ugandan parish. *S. Afr. J. Agric. Ext*., **36:** pp229–268

Herrings R. S. (1979) Hydrology and chronology: The Rhodah Nilometer as an arid dating Interlacustrine History. In *Chronology, migration and drought in Interlacustrine Africa*, edited by J. B. Webster, pp39-86

Hosking, J.R.M. and J.R. Wallis, (1987) Parameter and quantile estimation for the generalized Pareto distribution, *Technometrics*, **29**(3): pp339–349.

Hung, C.C., (2007) Apparent relations between solar activity and solar tides caused by the planets. Report NASA/TM-2007-214817

Hunter J.S., (1986) The exponentially weighted moving average. *Journal of quality Technology*, **18**: pp203-209.

Hyvärinen, O., Mtilatila, L., Pilli-Sihvola, K., Venäläinen, A., Gregow, H. (2015) The verification of seasonal precipitation forecasts for early warning in Zambia and Malawi. *Advances in Science and Research*, Vol. **12**: pp.31-36.

Indeje, M., F. H. M. Semazzi, and L. J. Ogallo, (2000) ENSO signals in East African rainfall seasons. *Int. J. Climatol.*, **20**: pp19–46.

Ivanov V. V., (2002) Periodic weather and climate variations. Institute of Marine Geology and Geophysics, Russian Academy of Sciences. *Phys.-Usp*. **45:** pp719

Jacob N. T., J. Reuder, E. Rutalebwa, S.. Nyimvua, M. d.S. Mesquita, (2016) Modelling of Extreme maximum Rainfall using Extreme Value Theory for Tanzania. *International Journal of Scientific and Innovative Mathematical Research,* Vol. **4**, Issue 3

Jones J.W., J.W. Hansen, F.S. Royce, C.D. Messina, (2000) Potential benefits of climate forecasting to agriculture. *Agriculture, Ecosystems and Environment* **82:** 169–184.

Joshua, M. K., Ngongondo C., Chipeta, L., Mpembeka, F., (2011) Integrating Indigenous Knowledge with Conventional Science: Enhancing Localised Climate and Weather

Forecasts in Nessa, Mulanje, Malawi. *Physics and Chemistry of the Earth*, **36**(14-15), pp996-1003.

Keeling C. D., Whorf T. P., (1997) Possible forcing of global temperature by ocean tides. Proc. *Natl. Acad. Sci*. **94**, pp8321-8328.

Keeling C. D., Whorp T.P., (2000) The 1800-year oceanic tidal Cycle: A possible cause of rapid climate Change. *PNAS.* **97**, No. 8., pp3814-3819.

KFSSG, (2019) The 2019 "Long Rains" season assessment report. Kenya Food Security Steering Group, *Government of Kenya Report*, August 2019. pp68

Kijazi A. L., Chang'a, L. B., Liwenga, E. T., Kanemba, A., & Nindi, S. J., (2012) The use of indigenous knowledge in weather and climate prediction in Mahenge and Ismani Wards, Tanzania. *Proceedings of the first Climate Change Impacts, Mitigation and Adaptation Programme Scientific Conference*. pp42-48

Kilavi, M. and A.W. Colman (2012) Integration of statistical and dynamical methods in seasonal forecasting: an example for Kenya. WCRP Africa Newsletter, Nov. 2012.

Klyashtorin, L.B. (2001) Climate change and long-term fluctuations of commercial catches: The possibility of forecasting. FAO Fisheries Technical Paper, 410, 86 p.

Klyashtorin, L. and A. Lyubushin, 2007; Short Term Global Dt Prediction Using (60–70)-Years Periodicity. *Energy & Environment*. Vol 23, Issue 1, 2012

Kohyama T., J. M. Wallace, (2016) Rainfall variations induced by the lunar gravitational atmospheric tide and their implications for the relationship between tropical rainfall and humidity. *Geophysical Research Letters*, 2016

Krupp, E. C. (2003) Echoes of the Ancient Skies: The Astronomy of Lost Civilizations, Astronomy Series, Courier Dover Publications Inc., Mineola, New York, pp. 62–72

Kuya E. K., (2016) Precipitation and temperatures extremes in East Africa in past and future climate. Masters Thesis, University of Oslo, Norway.

Lamb, H.H., (1966) African lake-level change, world rainfall pattern anomalies and related a spects of climatic change in the 1960s. *Meteorological Magazine* **95**, 181-183.

Lehman V.; D. Eno (2003) The Somali Bantu, their History and Culture. Cultural Resource Centre, Washington, DC.

Levey K.M., M.R., Jury (1996) Composite intraseasonal oscillations of convection over southern Africa. *Journal of Climate* **9**: pp1910–1920.

Li, G. Q., H. F. Zong, and Q. Y. Zhang, (2011) 27.3-day and average 13.6-day periodic oscillations in the Earth's rotation rate and atmospheric pressure fields due to celestial gravitation forcing. *Adv. Atmos. Sci*., **28**(1), pp45–58.

Lindzen, R. S., (1967) Thermally driven diurnal tide in the atmosphere. *Quart. J. Roy. Meteor. Soc.,* **93,** pp18–42.

Lucio R., (2003) Flussi e riflussi (Flows and ebbs), Feltrinelli, Milano, ISBN 88-07-10349-4.

Luseno W. K., J. G. McPeak, C. B. Barrett, P. D. Little and Getachew Gebru, (2002) Assessing the value of climate forecast information for pastoralists: Evidence from southern Ethiopia and northern Kenya. *IRI Technical Report* 02-03: pp70-92

Lyon Bradfield, David G. DeWitt, (2012) A recent and abrupt decline in the East African long rains. *Geophysical Research Letters*. Vol. **39**, Issue 2.

MacDonald G., Abarbane H., Koonin S., Levine H., O., Rothaus (1992) *Statistics of Extreme Events with Application to Climate*. The MITRE Corporation ll~lT NUMIEl JASON Program Office A10 JSR-90-05 7525, Colshire.

Mackey R., (2007) Rhodes Fairbridge and the idea that the solar system regulates the Earth's climate - Rhodes Fairbridge. *Journal of Coastal Research*, Special Issue **50**, pp955-968.

Mafongoya, P.L. and Ajayi, O.C. (2017) Indigenous Knowledge Systems and Climate Change Management in Africa, *CTA*, Wageningen, The Netherlands, pp316.

Mahoo H, W. Mbungu, I. Yonah, J. Recha, M. Radeny, P. Kimeli, J. Kinyangi, (2015) Integrating Indigenous Knowledge with Scientific Seasonal Forecasts for Climate Risk Management in Lushoto District in Tanzania. CCAFS Working Paper no. 103. CGIAR *Research Program on Climate Change, Agriculture and Food Security* (CCAFS). Copenhagen, Denmark.

Mapfumo P., Mtambanengwe F., Hikowo R. (2015) Climate and development. Building on Indigenous Knowledge to Strengthen the Capacity of Smallholder Farming Communities to Adapt to Climate Change and Variability in Southern Africa.

Mason, S.J. and S. Chidzambwa, 2008: Verification of RCOF Forecasts. World Meteorological Organization. An International Expert Review Meeting on Regional Climate Outlook Forums. Arusha, United Republic of Tanzania, 3 - 7 November 2008.

Mazzarella, (2009) Sun-Climate Linkage Now Confirmed. Energy & Environment. Vol 20, Issue 1.

Meeus, Jean (1998) Astronomical Algorithms, 2nd ed, ISBN 0-943396-61-1

Merchant, M.E.; Flanders, R.V.; Williams, R.E., (1987) Seasonal abundance and parasitism of house fly (Diptera: Muscidae) pupae in enclosed, shallow-pit poultry houses in Indiana. Environ. Entomol., 16: pp716–721.

Merritt, E. H. (1975) A History of the Taita of Kenya to 1900. PhD. Dissertation, Department of History, Indiana University.

Mhita, M.S., (2006) Training manual traditional knowledge for nature and environmental conservation, agriculture, food security and disaster management in Tanzania. UNEP. Online: *http://www.unep.org/ik/PDF/Tanzania%20Ik%20Training%20MANUAL.pdf*.

Michael R. M., (1999) The Star of Bethlehem: The Legacy of the Magi, Rutgers University Press. New Brunswick and London, pp187

Milankovitch, M. (1998) [1941]: Canon of Insolation and the Ice Age Problem.: Department for Equality and Teaching Resources, Belgrade. ISBN 8617066199.; (Online: *http://www.leif.org/EOS/197-203-Milankovich.pdf*)

Mogotsi, K., Moroka, A. B., Sitang, O., & Chibua, R., (2011) Seasonal precipitation forecasts: Agro-Ecological knowledge among rural Kalahari communities. *African Journal of Agricultural Research,* **6**(4): pp916-922.

Moore Henry Ludwell (1921) The Origin of the Eight-Year Generating Cycle. *The Quarterly Journal of Economics* Vol. **36**, No. 1 (Nov., 1921), pp. 1-29

Mugabe, F. T., Mubaya, C. P., Nanja, D., Gondwe, P., Munodawafa, A., Mutswangwa, E., … Murewi, C., (2010) Use of Indigenous Knowledge Systems and Scientific Methods for Climate Forecasting in Southern Zambia and North Western Zimbabwe. *Zimbabwe Journal of Technological Sciences*, **1**(1): pp22-36.

Muirden, J. (2005) Astronomy: A complete and practical guide to the night sky. Kingfisher Publications Plc., London. pp70

Muriuki Godfrey, (1969) A History of the Kikuyu to 1904, Ph.D. thesis, University of London, E.A Publishing House, Nairobi

Mwanahija S. S., (2016) Local knowledge of fishermen in weather prediction in Moa and Kwale coastal villages, Tanzania. WIO *Journal of Marine Science* **15** (1): pp79-89

Musembi D.K. and H. K. Cheruiyot, (2016) A Case for Validation of Indigenous Knowledge in Forecasting Rainfall among the Kamba Community of Makueni County, Lower Eastern Kenya. *J. Meteorol. Related. Sci*. Vol **9**, Issue 2, pp 26-34 http://dx.doi.org/10.20987/jmrs.4.08.2016

Mwanahija S. Shalli (2016) Local knowledge of fishermen in weather prediction in Moa and Kwale coastal villages, Tanzania. *Western Indian Ocean Journal of Marine Science* **15** (1), pp79-89

Mwaniki, H.S. Kabeca (1982) A Pre-colonial History of the Mt. Kenya, (1400-1908), Ph.D Thesis, Dalhouse University: Canada.

Mwiturubani D. A. (2015) The role of indigenous Weather Forecast in Enhancing agricultural Production in Tanzania. *Journal of the Geographical Association of Tanzania.* pp38-55.

Naidu C V, B R Srinivasa Rao and D V Bhaskar Rao (1999) Climatic trends and periodicities of annual rainfall over India. Meteorol. Appl. **6**, 395–404.

Ngailo J. T. (2016) Modelling of Extreme maximum Rainfall using Extreme Value Theory for Tanzania. International Journal of Scientific and Innovative Mathematical Research (IJSIMR)Vol. **4**, Issue 3, pp34-45

Nicholson, Sharon E. (2001) Climatic and environmental change in Africa during the last two centuries. *Clim Res*, Vol. **17**: 123–144, 200

NOAA (2017) Weather forecasting through the ages. Early history. (Online: *https://earthobservatory.nasa.gov)*

Nyamweru, C.K. (1996) The African Rift System. In Adams W, Goudie A, Orme A (eds). *The physical geography of Africa*. Oxford University Press, Oxford pp. 18-33

Obert J., P. L. Mafongoya, C. Mubaya, O. Mafongoya, (2016) Seasonal Climate Prediction and Adaptation Using Indigenous Knowledge Systems in Agriculture Systems in Southern Africa: A Review. *Journal of Agricultural Science*; Vol. **8**, No. 5

Offat M. I., C. Miriam, (2015) Integrating Indigenous Knowledge Systems into Climate Change Interpretation: Perspectives Relevant to Zimbabwe. *Greener Journal of Educational Research* ICV: 6.05 Vol. **5 (2)**, pp 27-36

Ogallo L., G. Ouma, A. Pala, G. Wayumba, (2010) Integrating Indigenous Knowledge in Climate Risk Management to Support Community Based Adaptation. *Final Technical Report* ICPAC, pp25.

Ogallo, L., (2010) The Mainstreaming of Climate Change and Variability Information into Planning and Policy Development for Africa. *Procedia Environmental Sciences*, **1**, pp405-410

Okonya J. S., J. Kroschel., 2013: Indigenous knowledge of seasonal weather forecasting: A case study in six regions of Uganda. *Agricultural Sciences* Vol.**4**: No.12, pp641-648

Olbrich, D.L.; King, B.H., (2003) Host and habitat use by parasitoids (Hymenoptera Pteromalidae) of house fly and stable fly (Diptera Muscidae) pupae. *Great Lakes Entomol*., **36**, pp179–190.

O'mahony, G. (2006) Rainfall and moon phases. *Quart. J. Roy. Meteorol*. Soc. 2006, **91**, pp196–207.

Ongoma, V; C., Haishan & Omony, G. (2018) Variability of Extreme Weather Events over the Equatorial East Africa, a case study of Rainfall in Kenya and Uganda. Theoretical and Applied Climatology. **131**. pp295-308.

Ouma, G., (2009) Linking traditional and modern forecasting in western Kenya. Stories from the field. (Accessed April 22, 2018, from *http://idrc.org/minga/ev-148990-201-1-DO_TOPIC.html*)

Prendergast, H.D.V.; Davis, S.D.; Way, M. (1999) Dryland Plants and Their Uses. In Spiritual Values of Biodiversity; Posey, D.A., Ed.; Intermediate Technology Publications: London, UK, pp 233–235.

Randall, D.A., R.A. Wood, S. Bony, R. Colman, T. Fichefet, J. Fyfe, V. Kattsov, A. Pitman, J. Shukla, J. Srinivasan, R.J. Stouffer, A. Sumi and K.E. Taylor, (2007) Climate Models and Their Evaluation. In: Climate Change 2007: The Physical Science Basis. Contribution of Working Group I to the Fourth Assessment Report of the IPCC. Cambridge University Press, Cambridge, United Kingdom and New York, NY, USA.

Risiro J., D. Mashoko, Doreen, T. Tshuma, and E. Rurinda, (2012) Weather Forecasting and Indigenous Knowledge Systems in Chimanimani District of Manicaland, *Zimbabwe Journal of Emerging Trends in Educational Research and Policy Studies* **3**(4): pp561-566

Roberts S. W., (1959) control chart tests based on geometric moving averages. *Technometrics,* **1**, pp239-251

Rowell, David P. Ben B. B. Booth, Sharone. Nicholson, and Peter Good, (2015) Reconciling Past and Future Rainfall Trends over East Africa. *Journal of Climate*. Vol. **28**

Russell, J. M., T. C. Johnson (2007) Little Ice Age drought in equatorial Africa: Intertropical con-vergence zone migrations and El Niño–Southern Oscillation variability. *Geology* ***35****,* pp21–24

Ryner, M., Holmgren, K., Taylor, D.(2008) A record of vegetation dynamics and lake level changes from Lake Emakat, northern Tanzania, during the last c. 1200 years. *J Paleolimnol*, Vol. **40**:583–601

Saitabau, Henri Ole (2014) Impacts of climate change on the livelihoods of loita maasai pastoral community and related indigenous knowledge on adaptation and mitigation directorate of research and collections. National Museums of Kenya. pp35

Saliba, G., (1994) Early Arabic Critique of Ptolemaic Cosmology: A Ninth-Century Text on the Motion of the Celestial Spheres. *Journal for the History of Astronomy* **25**: pp115–141

Salzburger W., Bert Van Bocxlaer and Andrew S. Cohen (2014) Ecology and Evolution of the African Great Lakes and their Faunas. *Annu. Rev. Ecol. Evol. Syst*. 2014. **45**, pp519–45

Scafetta, N., (2010) Empirical evidence for a celestial origin of the climate oscillations and its implications. *Journal of Atmospheric and Solar-Terrestrial Physics* **72**, pp951-970.

Scafetta, N., (2012a) A shared frequency set between the historical mid-latitude aurora records and the global surface temperature. *Journal of Atmospheric and Solar-Terrestrial Physics* **74**, pp145-163.

Scafetta, N., (2012b) Testing an astronomically based decadal-scale empirical harmonic climate model versus the IPCC (2007) general circulation climate models. *Journal of Atmospheric and Solar-Terrestrial Physics* **80**, pp124-137.

Scafetta, N., (2012c) Multi-scale harmonic model for solar and climate cyclical variation throughout the Holocene based on Jupiter-Saturn tidal frequencies plus the 11-year solar dynamo cycle. *Journal of Atmospheric and Solar- Terrestrial Physics* **80**, pp296-311.

Scofield, B., (2010) A History and Test of Planetary Weather Forecasting. University of Massachusetts, Amherst. Open Access Dissertations. Paper 221, pp 239

Shoko, K., & Shoko, N., (2013) Indigenous Weather Forecasting Systems: A Case Study of the Abiotic Weather Forecasting Indicators for Wards 12 and 13 in Mberengwa District Zimbabwe. *Asian Social Science*, **9**(5): pp285-297.

Shongwe M. E., G. J. V. Oldenborgh, B. V. D. Hurk, M. V. Aalst, 2010: Projected Changes in Mean and Extreme Precipitation in Africa under Global Warming. Part II: East Africa. *Journal of Climate*, **24**, pp3718-3733.

Sonka S.T., Hofing S.L., Changnon Jr S.A., (1992) How agribusiness uses climate predictions: implications for climate research and provision of predictions. *Bulletin of the American Meteorological Society* **73**: pp1999 – 2009.

Steve G., C. Parkinson, and M. Chahine, (2002) Weather Forecasting through the Ages. The Earth Observatory. EOS Project Science Office. https://earthobservatory.nasa.gov/Features/WxForecasting/wx.php (Accessed on 11 March 2018)

Stigter C. J. and Yunita T. Winarto (2012) What Climate Change Means for Farmers in Asia. *Earthzine*, 4, online http://www.earthzine.org/2012/04/04/ (accessed on 16 April 2018).

Stigter, C.J.; Dawei, Z.; Onyewotu, L.O.Z.; Xurong, M., (2005) Using traditional methods and indigenous technologies for coping with climate variability. *Climat. Chang*. 2005, **70**, pp255–271

Stubbs P., (1963) Why should the Moon affect the weather? *New Scientist*, 7 March 1963.

Tennant W. J., and B. C. Hewitson, (2002) Intra-Seasonal Rainfall Characteristics and their importance to the seasonal prediction problem. *Int. J. Climatol*. **22**: pp1033 – 1048

Tousson, O. (1925) Mémoire sur l'Histoire du Nil; *Mémoire de l'Institut d'Egypte*.

Vanacker, V., M. Linderman, F. Lupo, S. Flasse, and E. Lambin (2005) Impact of short-term rainfall fluctuation on interannual land cover change in sub-Saharan Africa. *Global Ecology and Biogeography* **14**: pp123-135.

Verschuren D, Laird KR, Cumming BF, (2000) Rainfall and drought in equatorial east Africa during the past 1,100 years. *Nature*. **403**(6768):pp410-4.

Vladimir A. Chobotov (2002) Orbital mechanics, Volume 1, Ed 3 illustrated, *American Institute of Aeronautics and Astronautics*, 2002, pp460

Vogel C., (2000) Usable science: an assessment of long-term seasonal forecasts amongst farmers in rural areas of South Africa. *South African Geographical Journal* **82**: pp107 – 116

Waerden B. L., (1987) The Heliocentric System in Greek, Persian and Hindu Astronomy, Annals of the New York Academy of Sciences, **500** (1): pp525–545.

Waheed, K. A., (1978) Islam and The Origins of Modern Science, Islamic Publication Ltd., Lahore, pp 27

Wara, M.W., A.C. Ravelo, M.L. Delaney, (2005) Permanent El Niño-like conditions during the Pliocene Warm Period. *Science* **309**: pp758-761.

Wilson I. R. G., (2013) The Venus–Earth–Jupiter spin–orbit coupling model. *Pattern Recogn. Phys*., **1**: pp147–158

Wilson, I., Carter, B., & Waite, I. (2008) Does a Spin–Orbit Coupling Between the Sun and the Jovian Planets Govern the Solar Cycle? *Publications of the Astronomical Society of Australia*, **25**(2): pp85-93

WMO (2013) The Climate in Africa: http://www.wmo.int/pages/prog/wcp/wcdmp/documents/1147_EN.pdf (Accessed on 30 March 2018)

WWF (2006) Climate Change Impacts on East Africa -A Review of the Scientific Literature, World Wide Fund for Nature Gland, Switzerland, pp 12. (online: *https://www.wwf.or.jp/activities/lib/pdf_climate/environment/east_africa_climate_change_impacts_final.pdf*)(Accessed on 18 March 2018).

Wrigley, C. (1964). The History of East Africa, Volume I. Edited by Roland Oliver and Gervase Mathew. Oxford: Clarendon Press, 1963. pp. xiii, 500. 63s. *The Journal of African History*, **5**(2), pp299-304.

Zuma-Netshiukhwi, G.N.; Beinzonhuit, R. (2008) Indigenous knowledge on rainfall forecasting. *Farm. Wkly*., **4** and **5,** pp22–23.

Zuma-Netshiukhwi, G.; Stigter, K.; Walker, S. (2013) Use of Traditional Weather/Climate Knowledge by Farmers in the South-Western Free State of South Africa: Agrometeorological Learning by Scientists. *Atmosphere*, **4**, pp383-410.

ANNEXES

Annex 1: Rainfall Cycle Models and their Statistical Summaries

The full results of the rainfall cycle models are presented here. Graphs show the variation of the mean monthly rainfall anomalies ($\overline{RR_\psi}$) and the fitted curve (RR_ψ) for every planet (ψ) in all the 12 zones. Three tables of a statistical summary of the relationship between the two is also given.

Zone 1: Saturn Rainfall Cycle Model

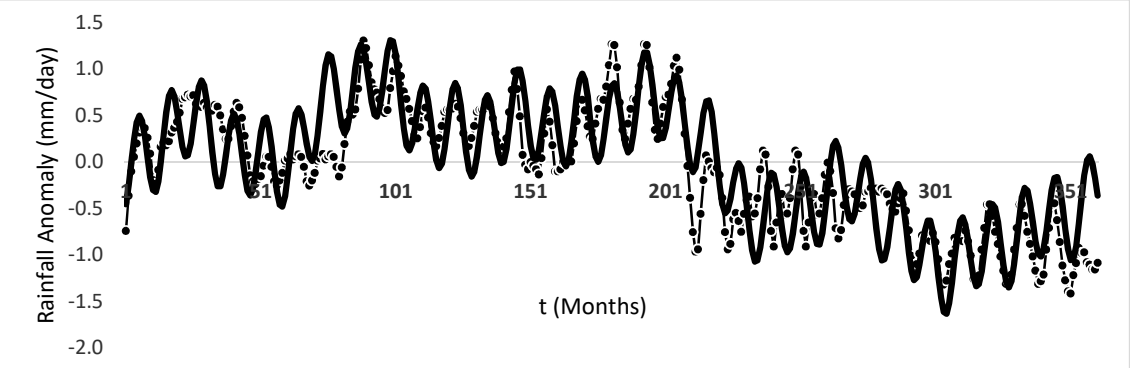

Figure 27: Variation of the mean Rainfall Anomaly (mm/day) and the fitted model curve in the Saturn 30-year cycle beginning at Saturn in Opposition phase in January.

The fitted curve;

$$RR_{\text{♄}} = 0.7\sin\big(0.0174(t-30)\big) + 0.2\sin\big(0.0349(t+15)\big) + 0.25\sin\big(0.0698(t+16)\big) + 0.2\sin\big(0.1046(t-10)\big) + 0.\ 1\sin 0.2616(t+5)) + 0.45\sin\big(0.5406(t-2)\big) \quad (57)$$

Regression Statistics	
Multiple R	0.81
R Square	0.66
Adjusted R Square	0.66
Standard Error	0.37
Observations	359

	df	SS	MS	F-Ratio	Significance F
Regression	1	98.15	98.15	698.69	0.00
Residual	357	50.15	0.14		
Total	358	148.31			

	Coefficients	Standard Error	t Stat	P-value
Intercept	-0.06	0.02	-3.00	0.00
Model	0.79	0.03	26.43	0.00

Zone 1: Jupiter Rainfall Cycle Model

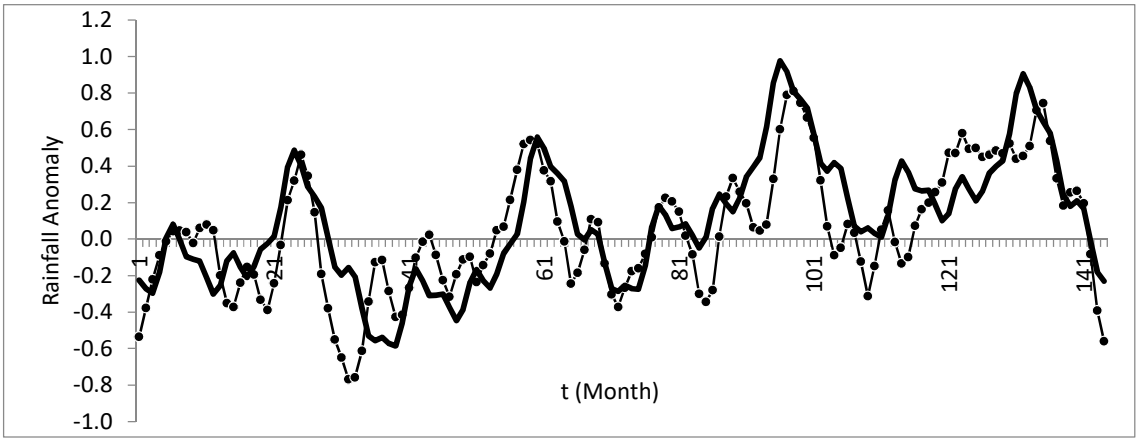

Figure 28: Variation of the mean Rainfall Anomaly (mm/day) and the fitted model curve in the Jupiter 12-year cycle beginning at Jupiter in Opposition phase in January.

The fitted curve;

$$RR_4 = 0.3\sin\big(0.0436(t+70)\big) + 0.3\sin\big(0.1744(t-15)\big) + 0.2\sin\big(0.3487(t-21)\big) + 0.1\sin\big(0.6974(t-22)\big) + 0.\ 07\sin 1.3949(t-18)) \quad (58)$$

The statistical summary of the relationship between the fitted curve and the rainfall anomaly;

Regression Statistics	
Multiple R	0.76
R Square	0.58
Adjusted R Square	0.58
Standard Error	0.22
Observations	143

	df	SS	MS	F-Ratio	Significance F
Regression	1	9.25	9.25	197.87	0.000
Residual	141	6.59	0.05		
Total	142	15.84			
	Coefficients	Standard Error		t Stat	P-value
Intercept	-0.03	0.02		-1.36	0.17
Model	0.74	0.05		14.07	0.00

Zone 1: Mars Rainfall Cycle Model

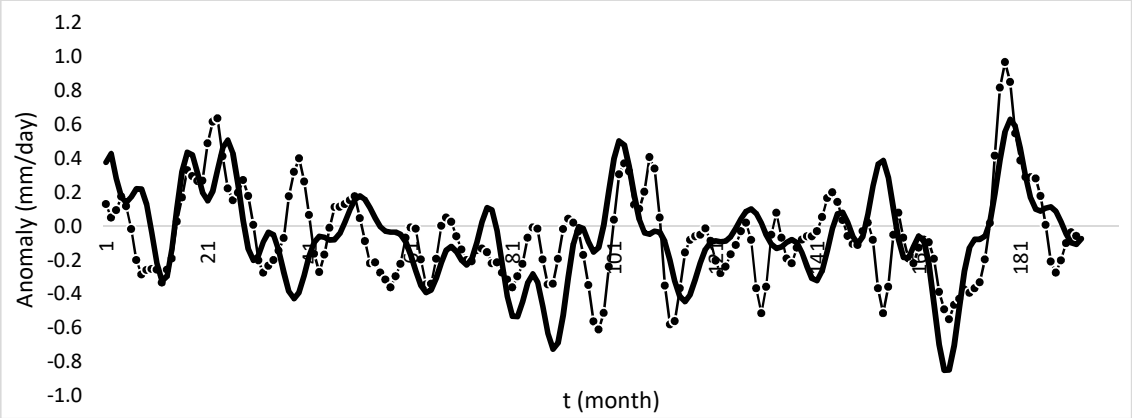

Figure 29: Variation of the mean Rainfall Anomaly (mm/day) and the fitted model curve in the Mars 15-year cycle beginning at Mars in Opposition phase in January.

The fitted curve;

$$RR_{\sigma}(t) = \{0.15\sin\big(0.035(t+39)\big) + 0.15\sin\big(0.14(t+2)\big) + 0.1\sin\big(0.7(t+9)\big) + 0.1\sin\big(0.3499(t+5)\big) + 0.35\sin\big(0.2449(t+7)\big) + 0.2\sin\big(0.7348(t+11)\big) - 0.1\} * \{1 + 0.9\sin 0.07t\} * 0.5 \quad (59)$$

The statistical summary of the relationship between the fitted curve and the rainfall anomaly;

Regression Statistics	
Multiple R	0.53
R Square	0.29
Adjusted R Square	0.28
Standard Error	0.23
Observations	179

	df	SS	MS	F-Ratio	Significance F
Regression	1	3.68	3.68	70.77	0.00
Residual	177	9.21	0.05		
Total	178	12.89			
	Coefficients	Standard Error		t Stat	P-value
Intercept	-0.03	0.02		-1.89	0.06
Model	0.52	0.06		8.41	0.00

Zone 1: Venus Rainfall Cycle Model

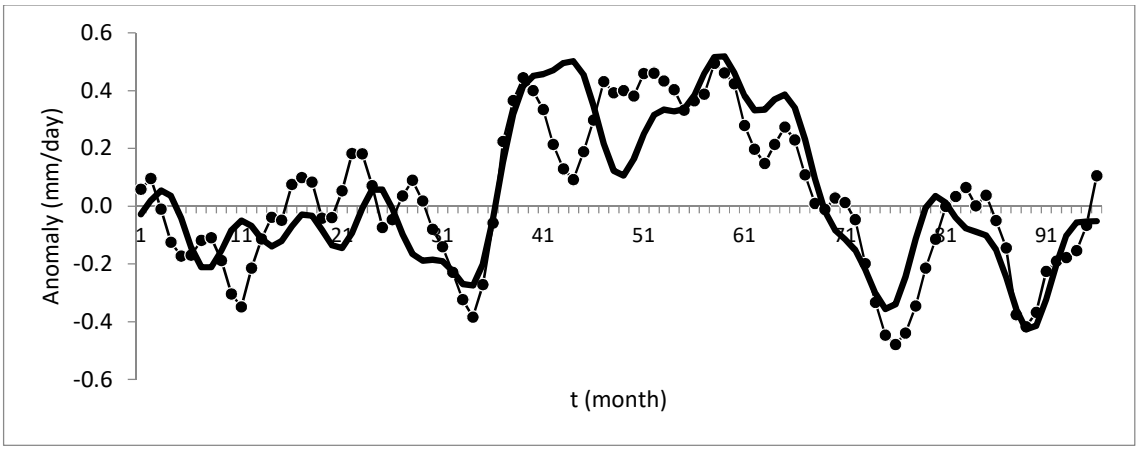

Figure 30: Variation of the mean Rainfall Anomaly (mm/day) and the fitted model (bold curve) in the Venus 8-year cycle beginning at Venus in inferior conjunction phase in January.

The fitted curve;

$$RR_{♀}(t) = 0.25\,sin\big(0.0665(t-27)\big) + 0.15\,sin\big(0.131(t-42)\big) + 0.15\,sin\big(0.3276(t-18)\big) + 0.07\,sin\big(0.9173(t-9)\big) + 0.07\,sin\big(0.2621(t-10)\big) + 0.1\,sin\big(0.4586(t-10)\big) + 0.03 \quad (60)$$

The statistical summary of the relationship between the fitted curve and the rainfall anomaly;

Regression Statistics	
Multiple R	0.84
R Square	0.71
Adjusted R Square	0.71
Standard Error	0.14
Observations	96

	df	SS	MS	F-Ratio	Significance F
Regression	1	4.31	4.31	229.96	0.00
Residual	94	1.76	0.02		
Total	95	6.07			
	Coefficients	Standard Error	t Stat	P-value	
Intercept	0.00	0.01	0.30	0.76	
Model	0.84	0.06	15.16	0.00	

Zone 2: Saturn Rainfall Cycle Model

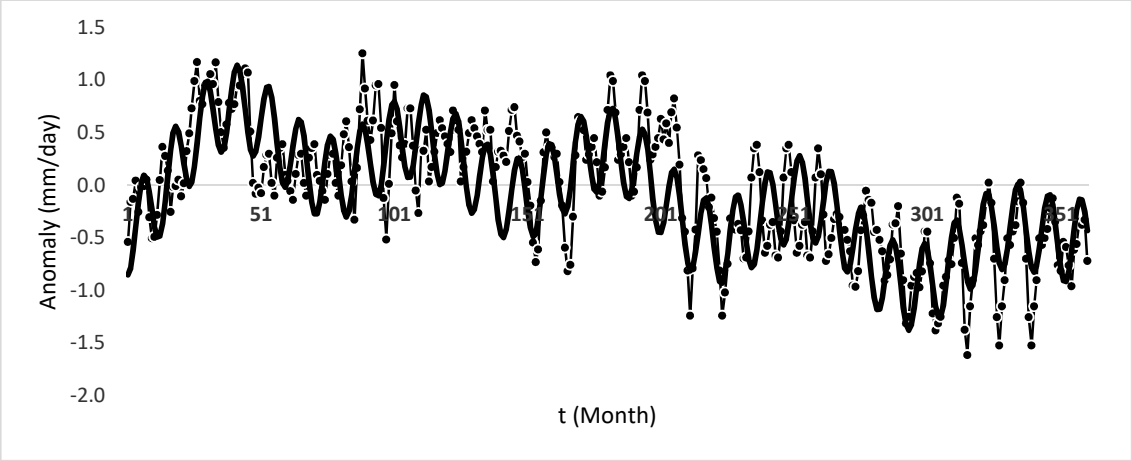

Figure 31: Variation of the mean Rainfall Anomaly (mm/day) and the fitted model (bold curve) in the Saturn 30-year cycle beginning at Saturn in Opposition phase in January.

The fitted curve;

$$RR_{t_2}(t) = 0.\ 5\ sin\big(0.01744(t-25)\big) + 0.2\ sin\big(0.0349(t+5)\big) + 0.1\ sin\ (0.0523(t-5))\ +\ 0.3\ sin(0.0872(t-20)) + 0.4\ sin\ (0.5406(t-4)) \quad (61)$$

The statistical summary of the relationship between the fitted curve and the rainfall anomaly;

Regression Statistics	
Multiple R	0.72
R Square	0.52
Adjusted R Square	0.52
Standard Error	0.41
Observations	359

	df	SS	MS	F-Ratio	Significance F
Regression	1	65.14	65.14	392.95	0.00
Residual	357	59.18	0.17		
Total	358	124.32			
	Coefficients	Standard Error		t Stat	P-value
Intercept	0.03	0.02		1.37	0.17
Model	0.81	0.04		19.82	0.00

Zone 2: Jupiter Rainfall Cycle Model

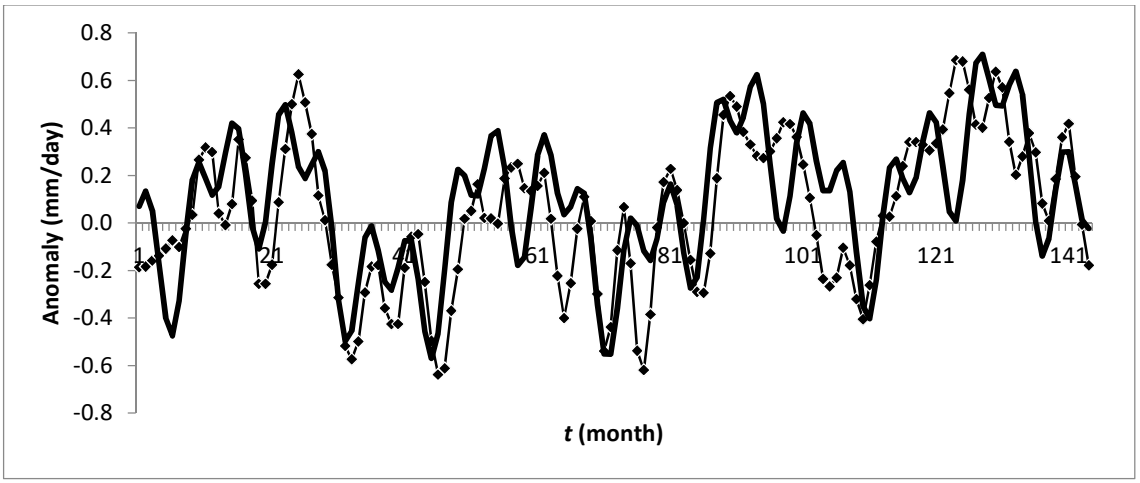

Figure 32: Variation of the mean Rainfall Anomaly (mm/day) and the fitted model (bold curve) in the Jupiter 12-year cycle beginning at Jupiter in Opposition phase in January

The fitted curve;

$$RR_{\mathbf{4}}(t) = 0.15\sin\big(0.0436(t+60)\big) + 0.25\sin\big(0.1744(t-12)\big) + 0.2\sin\big(0.4795(t+4)\big) + 0.2\sin\big(0.959(t-1)\big) \quad (62)$$

The statistical summary of the relationship between the fitted curve and the rainfall anomaly;

Regression Statistics	
Multiple R	0.69
R Square	0.47
Adjusted R Square	0.47
Standard Error	0.23
Observations	143

	df	SS	MS	F-Ratio	Significance F
Regression	1	6.58	6.58	126.52	0.00
Residual	141	7.33	0.05		
Total	142	13.91			
	Coefficients	Standard Error		t Stat	P-value
Intercept	-0.03	0.02		-1.47	0.14
Model	0.74	0.07		11.25	0.00

Zone 2: Mars Rainfall Cycle Model

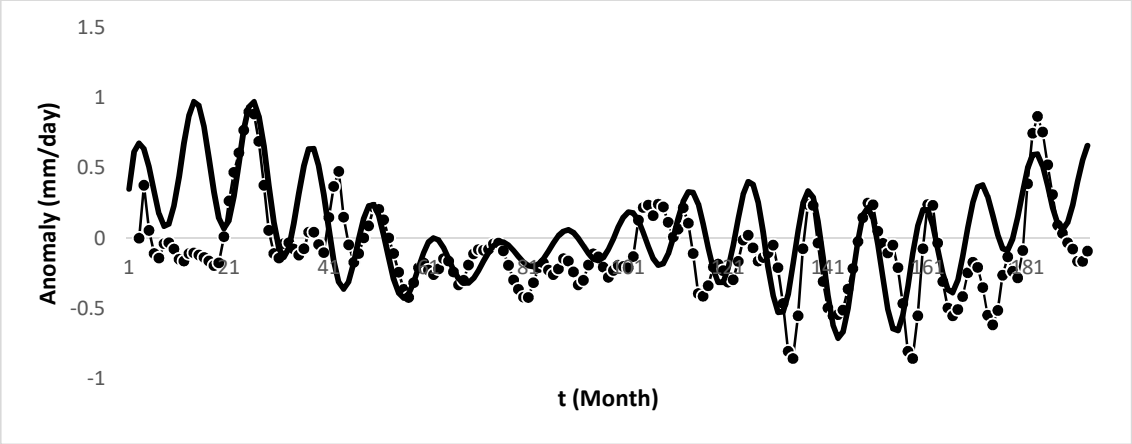

Figure 33: Variation of the mean Rainfall Anomaly (mm/day) and the fitted model (bold curve) in the Mars 15-year cycle beginning at Mars in Opposition phase in January.

The fitted curve;

$$RR_{\boldsymbol{\sigma}}(t) = \{0.\ 15\sin(0.035(t+35)) + 0.2\ \sin(0.07(t+3)) + 0.2\ \sin(0.05249(t - 1)\ + 0.15\sin(0.4899(t+5)) + 0.15\ \sin(0.5598(t))\} * \{1 + 0.8\sin(0.0349(t+5))\} * 0.7 \quad (63)$$

The statistical summary of the relationship between the fitted curve and the rainfall anomaly;

Regression Statistics	
Multiple R	0.34
R Square	0.12
Adjusted R Square	0.11
Standard Error	0.28
Observations	179

	df	SS	MS	F-Ratio	Significance F
Regression	1	1.82	1.82	23.03	0.00
Residual	177	14.01	0.08		
Total	178	15.83			
	Coefficients	Standard Error		t Stat	P-value
Intercept	-0.12	0.02		-5.63	0.00
Model	0.29	0.06		4.80	0.00

Zone 2: Venus Rainfall Cycle Model

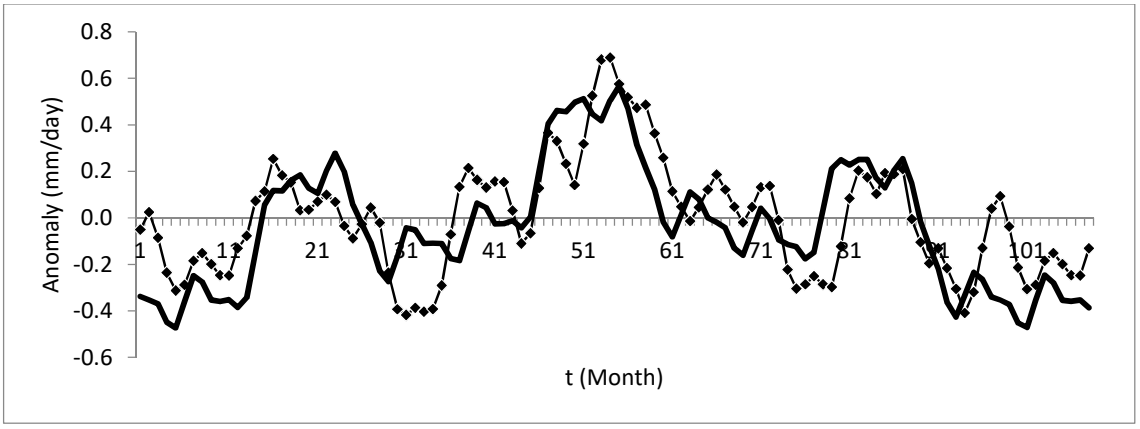

Figure 34: Variation of the mean Rainfall Anomaly (mm/day) and the fitted model (bold curve) in the Venus 8-year cycle beginning at Venus in inferior conjunction phase in January.

The fitted curve;

$$RR_{♀}(t) = 0.25\sin\big(0.1966(t-12)\big) + 0.1\sin(0.3931t) + 0.05\sin\big(1.5725(t+2)\big) + 0.1\sin\big(0.7862(t+2)\big) + 0.2\sin\big(0.0655(t-30)\big) \quad (64)$$

The statistical summary of the relationship between the fitted curve and the rainfall anomaly;

Regression Statistics	
Multiple R	0.74
R Square	0.54
Adjusted R Square	0.54
Standard Error	0.17
Observations	95

	df	SS	MS	F-Ratio	Significance F
Regression	1	3.23	3.23	110.44	0.00
Residual	93	2.72	0.03		
Total	94	5.95			
	Coefficients	Standard Error		t Stat	P-value
Intercept	0.01	0.02		0.83	0.41
Model	0.74	0.07		10.51	0.00

Zone 3: Saturn Rainfall Cycle Model

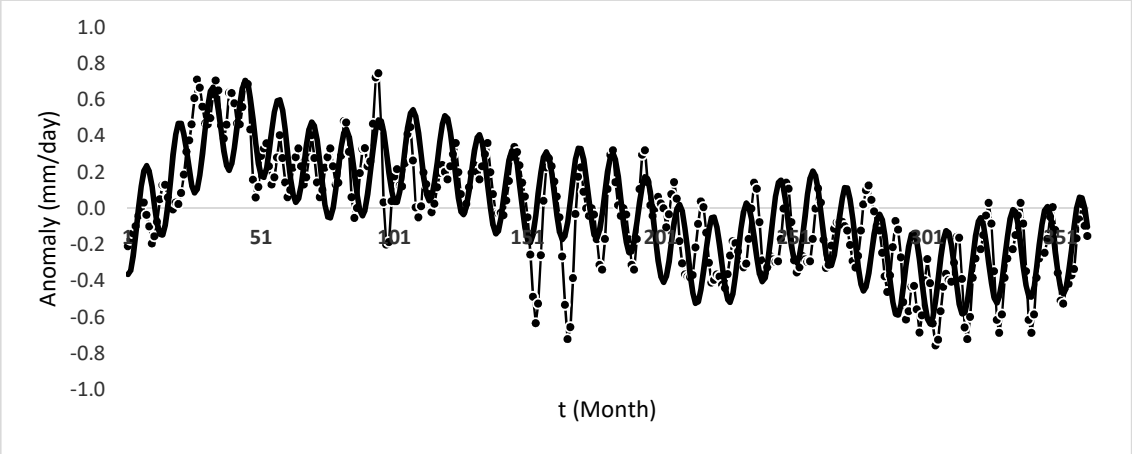

Figure 35: Variation of the mean Rainfall Anomaly (mm/day) and the fitted model (bold curve) in the Saturn 30-year cycle beginning at Saturn in Opposition phase in January.

The fitted curve;

$$RR_{\mathbf{t_2}}(t) = 0.3\sin\big(0.0173(t)\big) + 0.1\sin\big(0.0346(t-10)\big) + 0.1\sin\big(0.0519(t)\big) + 0.1\sin\big(0.0865(t-20)\big) + 0.25\sin\big(0.5017(t+8)\big) \quad (65)$$

The statistical summary of the relationship between the fitted curve and the rainfall anomaly;

Regression Statistics	
Multiple R	0.73
R Square	0.53
Adjusted R Square	0.53
Standard Error	0.22
Observations	359

	df	SS	MS	F-Ratio	Significance F
Regression	1	18.63	18.63	399.05	0.00
Residual	357	16.67	0.05		
Total	358	35.29			
	Coefficients	Standard Error		t Stat	P-value
Intercept	-0.03	0.01		-2.98	0.00
Model	0.75	0.04		19.98	0.00

Zone 3: Jupiter Rainfall Cycle Model

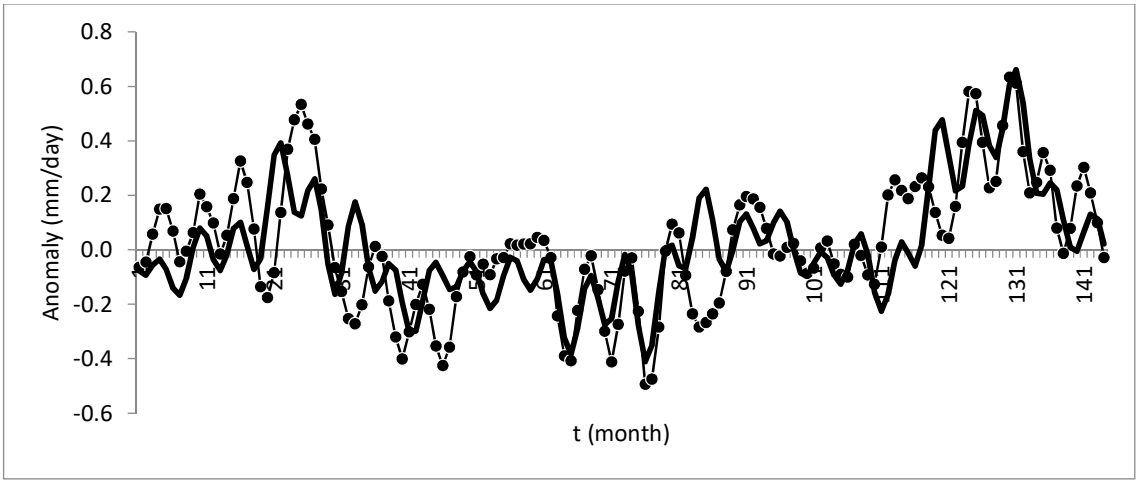

Figure 36: Variation of the mean Rainfall Anomaly (mm/day) and the fitted model (bold curve) in the Jupiter 12-year cycle beginning at Jupiter in Opposition phase in January.

The fitted curve;

$$RR_{\mathbf{4}}(t) = [0.2\sin(0.0436(t+50)) + 0.15\sin(0.1308(t-20)) + 0.1\sin(0.5231(t-20)) + 0.15\sin(0.1744(t-12)) + 0.15\sin(1.08987(t-20))] * [1 + 0.6\sin(0.1308(t-15))] * 0.5 \quad (66)$$

The statistical summary of the relationship between the fitted curve and the rainfall anomaly;

Regression Statistics	
Multiple R	0.69
R Square	0.48
Adjusted R Square	0.47
Standard Error	0.17
Observations	143

	df	SS	MS	F-Ratio	Significance F
Regression	1	3.67	3.67	128.16	0.00
Residual	141	4.04	0.03		
Total	142	7.71			
	Coefficients	Standard Error		t Stat	P-value
Intercept	0.01	0.01		0.50	0.62
Model	0.79	0.07		11.32	0.00

Zone 3: Mars Rainfall Cycle Model

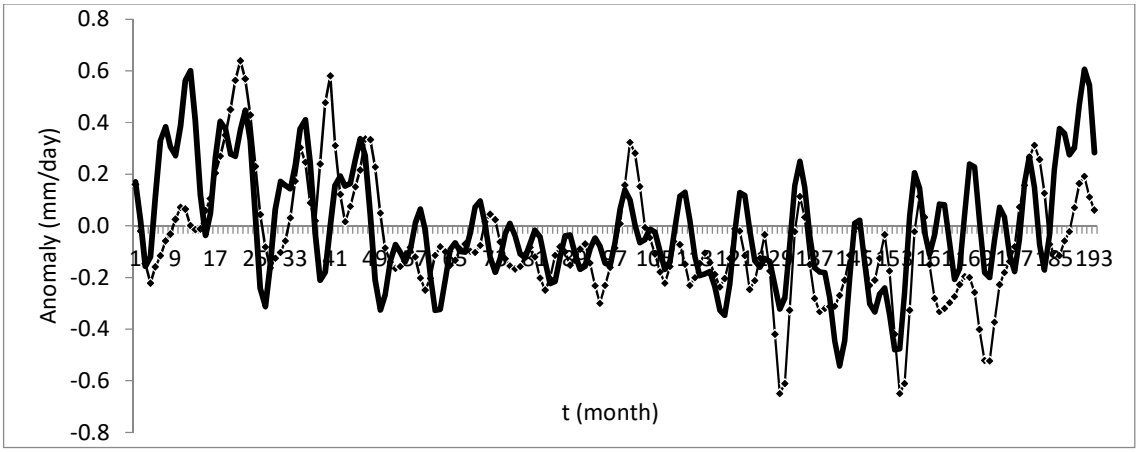

Figure 37: Variation of the mean Rainfall Anomaly (mm/day) and the fitted model (bold curve) in the Mars 15-year cycle beginning at Mars in Opposition phase in January.

The fitted curve;

$$RR_{\sigma}(t) = [0.03\sin\big(0.035(t+25)\big) + 0.1\sin\big(0.07(t+5)\big) + 0.1\sin\big(0.2099(t-5)\big) + 0.15\sin\big(1.0847(t+1)\big) + 0.1\sin\big(0.4899(t+9)\big)\,0.15\sin\big(0.5598(t+3)\big) +] * [1 + 0.6\sin\big(0.035(t+45)\big)] * 0.6 \quad (67)$$

The statistical summary of the relationship between the fitted curve and the rainfall anomaly;

Regression Statistics	
Multiple R	0.55
R Square	0.30
Adjusted R Square	0.30
Standard Error	0.19
Observations	180

	df	SS	MS	F-Ratio	Significance F
Regression	1	2.64	2.64	76.18	0.00
Residual	178	6.18	0.03		
Total	179	8.82			
	Coefficients	Standard Error		t Stat	P-value
Intercept	-0.03	0.01		-2.06	0.04
Model	0.62	0.07		8.73	0.00

Zone 3: Venus Rainfall Cycle Model

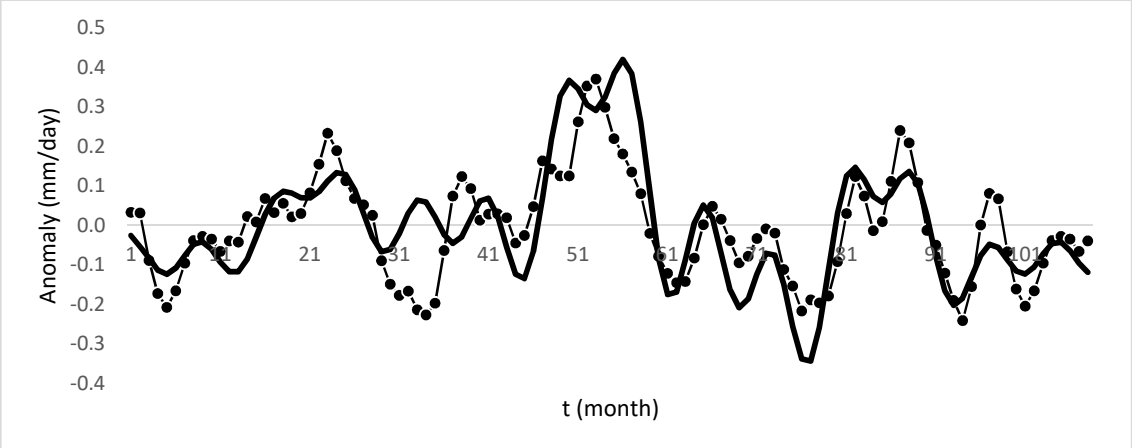

Figure 38: Variation of the mean Rainfall Anomaly (mm/day) and the fitted model (bold curve) in the Venus 8-year cycle beginning at Venus in inferior conjunction phase in January.

The fitted curve;

$$RR_{♀}(t) = \{0.1\sin\big(0.3931(t-17)\big) + 0.1\sin\big(0.7862(t-15)\big) + 0.1\sin\big(0.0655(t-20)\big) + 0.15\sin\big(0.1966(t-14)\big)\} * \{1 + 0.8\sin\big(0.0655(t-40)\big)\} * 0.6 \quad (68)$$

The statistical summary of the relationship between the fitted curve and the rainfall anomaly;

Regression Statistics	
Multiple R	0.78
R Square	0.60
Adjusted R Square	0.60
Standard Error	0.09
Observations	96

	df	SS	MS	F-Ratio	Significance F
Regression	1	1.040	1.040	143.4	0.000
Residual	94	0.682	0.007		
Total	95	1.722			
	Coefficients	Standard Error		t Stat	P-value
Intercept	-0.006	0.009		-0.679	0.499
Model	0.668	0.056		11.977	0.000

Zone 4: Saturn Rainfall Cycle Model

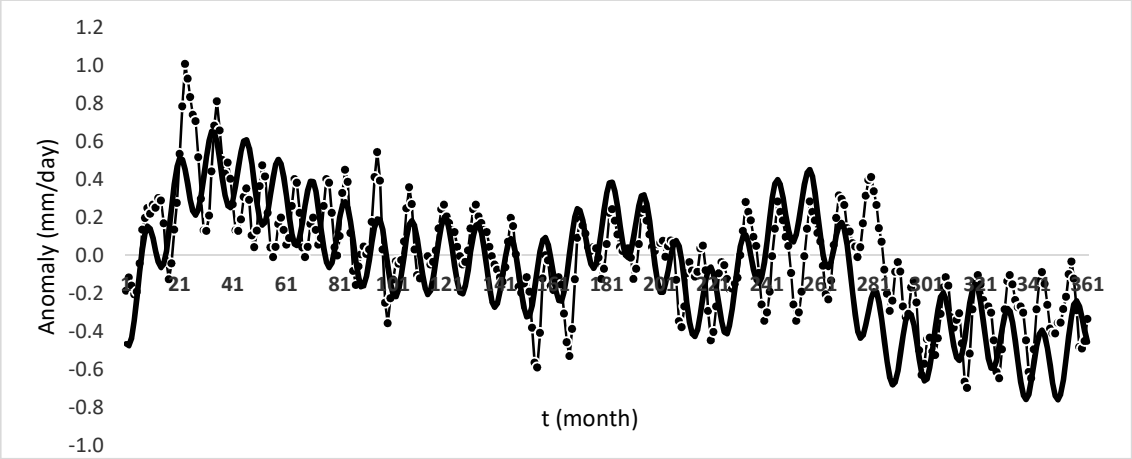

Figure 39 :Variation of the mean Rainfall Anomaly (mm/day) and the fitted model (bold curve) in the Saturn 30-year cycle beginning at Saturn in Opposition phase in January.

The fitted curve;

$$RR_{\mathbf{h}}(t) = 0.2\ \sin\big(0.0174(t-20)\big) + 0.25\ \sin\big(0.0349(t-5)\big) + 0.15\ \sin\big(0.0523(t-5)\big) + 0.1\ \sin\big(0.1046(t+1)\big) + 0.15\ \sin\big(0.0872(t-18)\big) + \ 0.2\ \sin\big(0.5058(t+7)\big) \quad (69)$$

The statistical summary of the relationship between the fitted curve and the rainfall anomaly;

Regression Statistics	
Multiple R	0.68
R Square	0.47
Adjusted R Square	0.47
Standard Error	0.21
Observations	359

	df	SS	MS	F-Ratio	Significance F
Regression	1	13.35	13.35	313.68	0.00
Residual	357	15.19	0.04		
Total	358	28.54			
	Coefficients	Standard Error		t Stat	P-value
Intercept	0.02	0.01		2.07	0.04
Model	0.61	0.03		17.71	0.00

Zone 4: Jupiter Rainfall Cycle Model

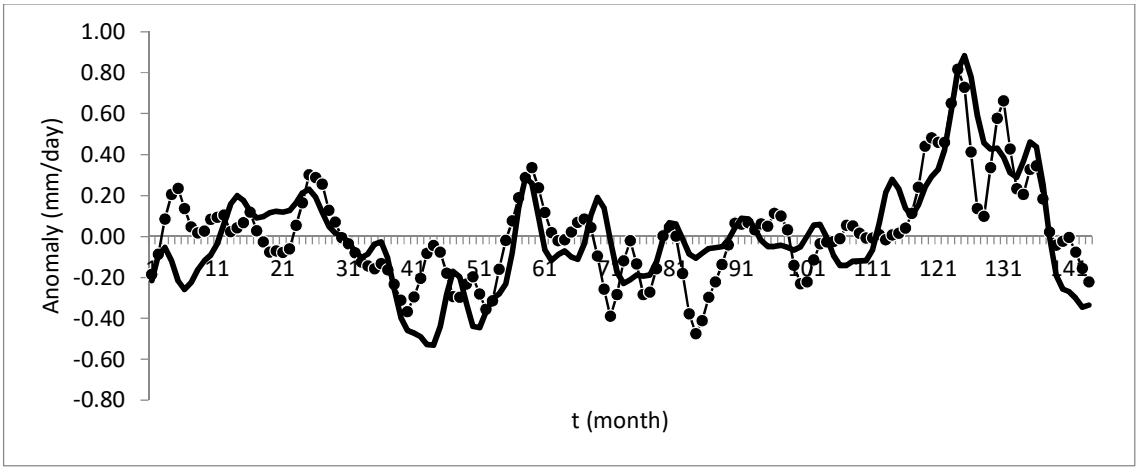

Figure 40: Variation of the mean Rainfall Anomaly (mm/day) and the fitted model (bold curve) in the Jupiter 12-year cycle beginning at Jupiter in Opposition phase in January.

The fitted curve;

$$RR_{\mathbf{4}}(t) = \{0.15\sin\big(0.0436(t+50)\big) + 0.2\sin\big(0.1308(t-12)\big) + 0.2\sin\big(0.1744(t-12)\big) + 0.15\sin\big(0.5667(t-11)\big) + 0.07\sin\big(1.1333(t-7)\big)\} * \{1 + 0.6\sin\big(0.0872(t-40)\big)\} * 0.8 \quad (70)$$

The statistical summary of the relationship between the fitted curve and the rainfall anomaly;

Regression Statistics	
Multiple R	0.74
R Square	0.55
Adjusted R Square	0.55
Standard Error	0.16
Observations	143

	df	SS	MS	F-Ratio	Significance F
Regression	1	4.24	4.24	175.74	0.00
Residual	141	3.40	0.02		
Total	142	7.64			
	Coefficients	Standard Error	t Stat	P-value	
Intercept	0.016	0.013	1.232	0.220	
Model	0.669	0.050	13.257	0.000	

Zone 4: Mars Rainfall Cycle Model

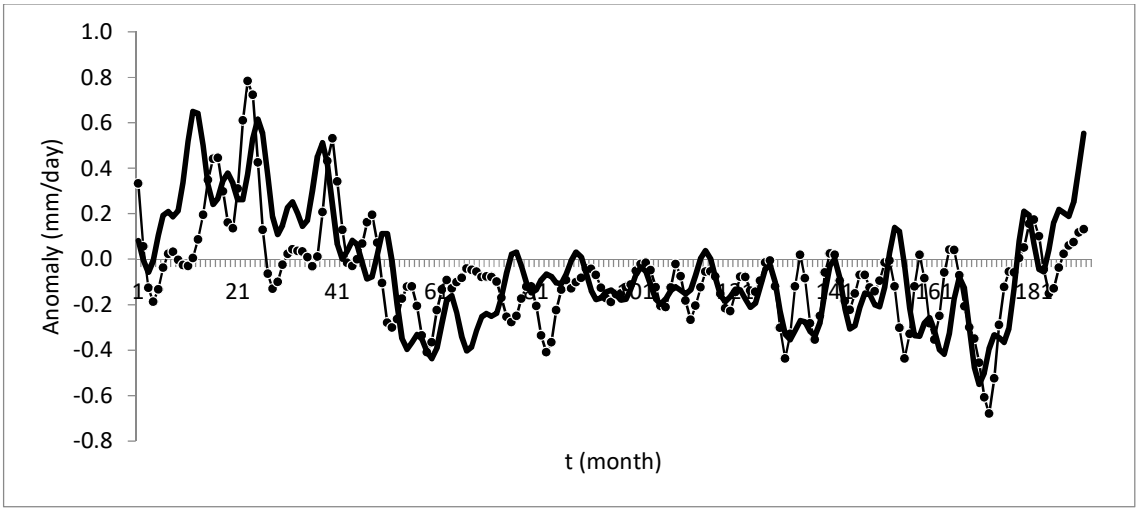

Figure 41: Variation of the mean Rainfall Anomaly (mm/day) and the fitted model (bold curve) in the Mars 15-year cycle beginning at Mars in Opposition phase in January.

The fitted curve;

$$RR_{\boldsymbol{\sigma}}(t) = \{0.2\sin\big(0.035(t+25)\big) + 0.15\sin 0.07t + 0.1\sin\big(0.1050(t-10)\big) + 0.1\sin\big(0.9797(t+2)\big) + 0.12\sin\big(0.4899(t+4)\big) + 0.1\sin 0.175t\} * \{1 + 0.7\sin\big(0.035(t+10)\big)\} * 0.6 \quad (71)$$

The statistical summary of the relationship between the fitted curve and the rainfall anomaly;

Regression Statistics	
Multiple R	0.62
R Square	0.38
Adjusted R Square	0.38
Standard Error	0.17
Observations	179

	df	SS	MS	F-Ratio	Significance F
Regression	1	3.00	3.00	108.17	0.00
Residual	177	4.90	0.03		
Total	178	7.90			
	Coefficients	Standard Error		t Stat	P-value
Intercept	-0.024	0.014		-1.777	0.077
Model	0.559	0.054		10.400	0.000

Zone 4: Venus Rainfall Cycle Model

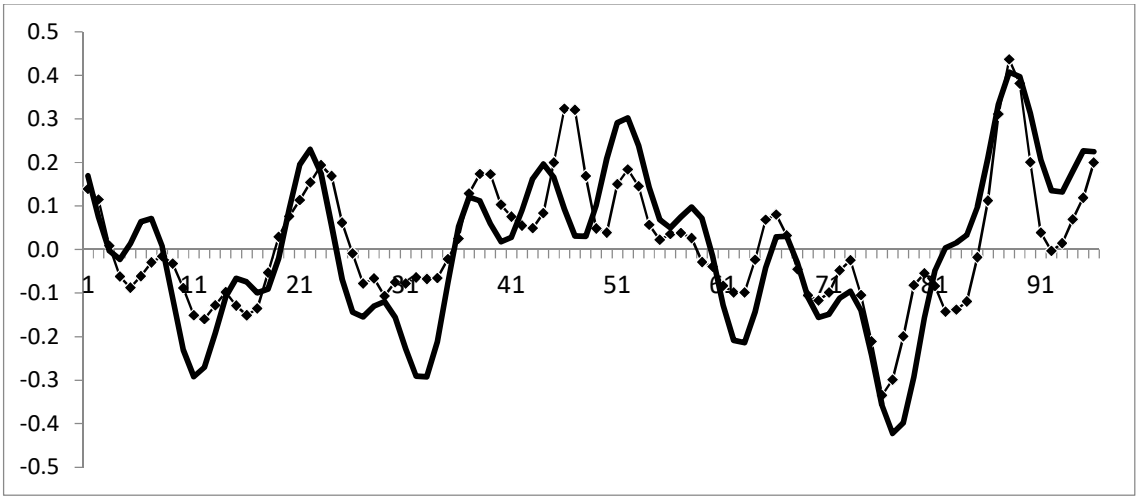

Figure 42: Variation of the mean Rainfall Anomaly (mm/day) and the fitted model (bold curve) in the Venus 8-year cycle beginning at Venus in inferior conjunction phase in January.

The fitted curve;

$$RR_{♀}(t) = 0.1\sin\big(0.3931(t-2)\big) + 0.1\sin\big(0.8518(t+2)\big) + 0.15\sin\big(0.131(t-35)\big) + 0.1\sin\big(0.1966(t-16)\big) + 0.1\sin\big(0.2621(t-14)\big) \quad (72)$$

The statistical summary of the relationship between the fitted curve and the rainfall anomaly;

Regression Statistics	
Multiple R	0.81
R Square	0.66
Adjusted R Square	0.66
Standard Error	0.08
Observations	95

	df	SS	MS	F	Significance F
Regression	1	1.18	1.18	180.49	0.00
Residual	93	0.61	0.01		
Total	94	1.79			
	Coefficients	Standard Error		t Stat	P-value
Intercept	0.01	0.01		1.38	0.17
Model	0.63	0.05		13.43	0.00

Zone 5: Saturn Rainfall Cycle Model

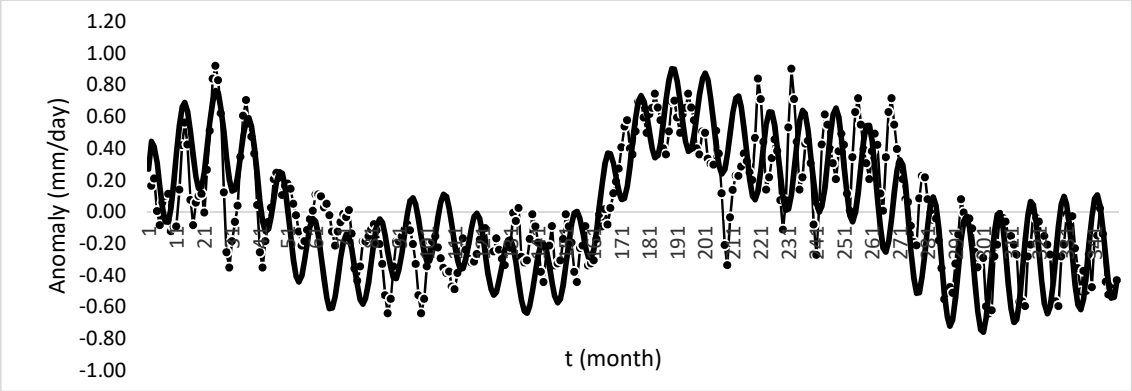

Figure 43: Variation of the mean Rainfall Anomaly (mm/day) and the fitted model (bold curve) in the Saturn 30-year cycle beginning at Saturn in Opposition phase in January.

The fitted curve;

$$RR_{♄}(t) = [0.4\sin(0.0346(t+20)) + 0.3\sin(0.5363(t+1)) + 0.17\sin(0.0692(t+10)) + 0.2\sin(0.173(t-140)) + 0.18\sin(0.0865(t-15))] * [1 + 0.4\sin(0.0173(\mathrm{t}+150))] * 0.65 \quad (73)$$

The statistical summary of the relationship between the fitted curve and the rainfall anomaly;

Regression Statistics	
Multiple R	0.73
R Square	0.53
Adjusted R Square	0.53
Standard Error	0.24
Observations	347

	df	SS	MS	F-Ratio	Significance F
Regression	1	23.01	23.01	383.49	0.00
Residual	345	20.70	0.06		
Total	346	43.71			
	Coefficients	Standard Error		t Stat	P-value
Intercept	0.01	0.01		1.05	0.29
Model	0.65	0.03		19.58	0.00

Zone 5: Jupiter Rainfall Cycle Model

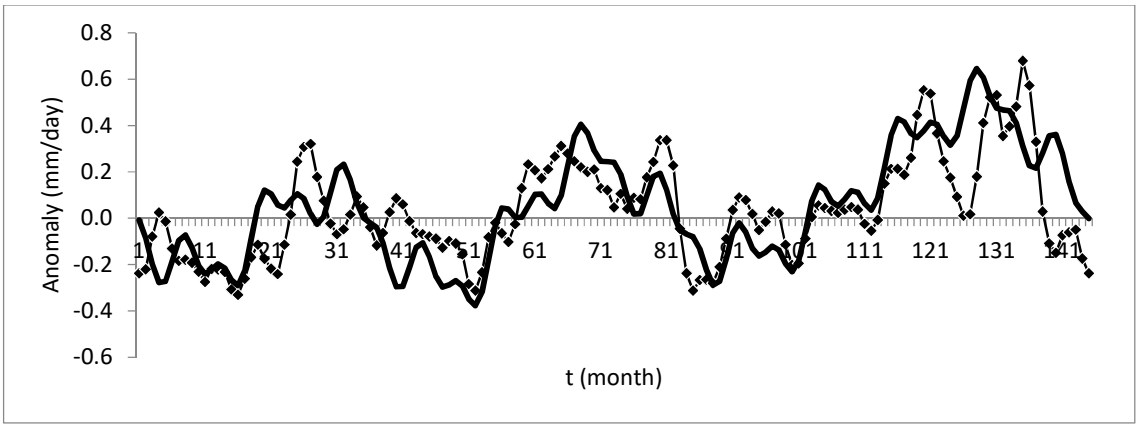

Figure 44: Variation of the mean Rainfall Anomaly (mm/day) and the fitted model (bold curve) in the Jupiter 12-year cycle beginning at Venus in inferior conjunction phase in January.

The fitted curve;

$$RR_{\mathbf{4}}(t) = 0.15\sin\big(0.0436(t+60)\big) + 0.15\sin\big(0.0872(t-40)\big) + 0.2\sin\big(0.1308(t-15)\big) + 0.07\sin\big(1.0462(t)\big) + 0.1\sin\big(0.1744(t-20)\big) + 0.1\sin\,(0.5231(t-6)) \quad (74)$$

The statistical summary of the relationship between the fitted curve and the rainfall anomaly;

Regression Statistics	
Multiple R	0.688
R Square	0.473
Adjusted R Square	0.470
Standard Error	0.156
Observations	144

	df	SS	MS	F-ratio	Significance F
Regression	1	3.12	3.12	127.59	0.00
Residual	142	3.48	0.02		
Total	143	6.60			
	Coefficients	Standard Error		t Stat	P-value
Intercept	0.003	0.013		0.223	0.824
Model	0.614	0.054		11.295	0.000

Zone 5: Mars Rainfall Cycle Model

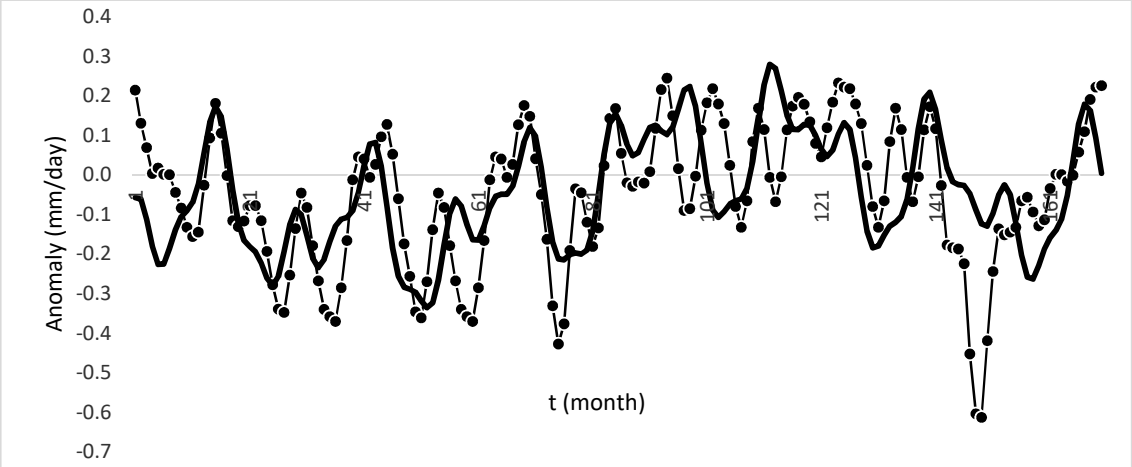

Figure 45: Variation of the mean Rainfall Anomaly (mm/day) and the fitted model (bold curve) in the Mars 15-year cycle beginning at Mars in Opposition phase in January.

The fitted curve;

$$RR_{\sigma}(t) = 0.05\sin\big(0.9097(t+14)\big) + 0.12\sin(0.2449(t-8)) + 0.1\sin\big(0.035(t-70)\big) + 0.05\sin\big(0.07(t-80)\big) + 0.1\sin\big(0.4549(t+16)\big) \quad (75)$$

The statistical summary of the relationship between the fitted curve and the rainfall anomaly;

Regression Statistics	
Multiple R	0.59
R Square	0.34
Adjusted R Square	0.34
Standard Error	0.14
Observations	169

	df	SS	MS	F-Ratio	Significance F
Regression	1	1.78	1.78	87.92	0.00
Residual	167	3.38	0.02		
Total	168	5.16			
	Coefficients	Standard Error		t Stat	P-value
Intercept	-0.01	0.01		-0.62	0.53
Model	1.13	0.12		9.38	0.00

Zone 5: Venus Rainfall Cycle Model

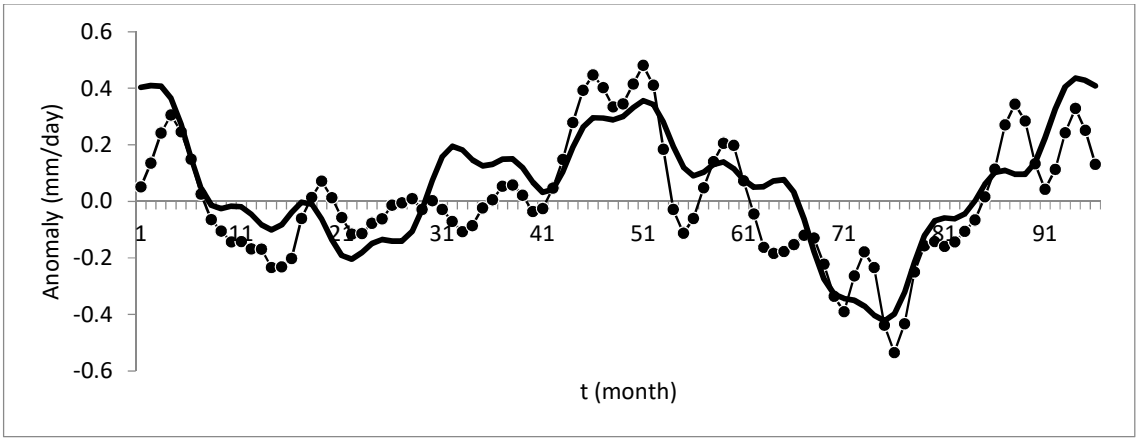

Figure 46 :Variation of the mean Rainfall Anomaly (mm/day) and the fitted model (bold curve) in the Venus 8-year cycle beginning at Venus in inferior conjunction phase in January.

The fitted curve;

$$RR_{♀}(t) = 0.05\sin\big(0.0655(t-7)\big) + 0.25\sin\big(0.131(t+12)\big) + 0.1\sin\big(0.1966(t-21)\big) + 0.1\sin\big(0.3931(t-13)\big) + 0.05\sin\,(0.9173(t-16)) \quad (76)$$

The statistical summary of the relationship between the fitted curve and the rainfall anomaly;

Regression Statistics	
Multiple R	0.82
R Square	0.67
Adjusted R Square	0.66
Standard Error	0.12
Observations	96

	df	SS	MS	F-Ratio	Significance F
Regression	1	2.81	2.81	189.49	0.00
Residual	94	1.39	0.01		
Total	95	4.20			
	Coefficients	Standard Error	t Stat	P-value	
Intercept	0.006	0.012	0.493	0.623	
Model	0.784	0.057	13.766	0.000	

Zone 6: Saturn Rainfall Cycle Model

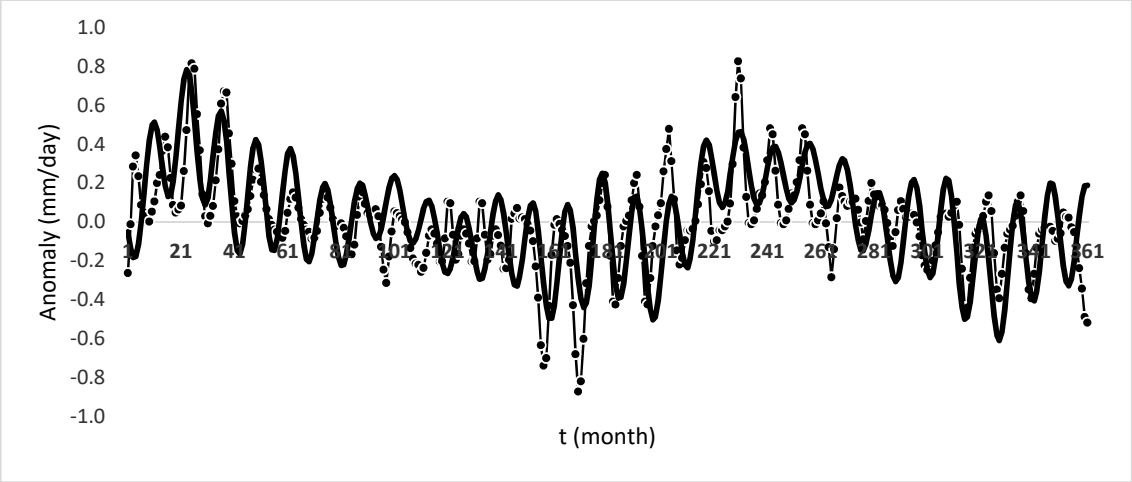

Figure 47 :Variation of the mean Rainfall Anomaly (mm/day) and the fitted model (bold curve) in the Saturn 30-year cycle beginning at Saturn in Opposition phase in January.

The fitted curve;

$$RR_{ħ}(t) = [0.1\sin(0.0346(t-10)) + 0.1\sin(0.0519(t+30)) + 0.1\sin(0.0865(t-5)) + 0.05\sin(0.1557(t+30)) + 0.2\sin(0.4844(t+6)) + 0.1\sin(0.0173(t+120))] * [1 + 0.3\sin(0.0173(t+170))]*0.8 \quad (77)$$

The statistical summary of the relationship between the fitted curve and the rainfall anomaly;

Regression Statistics	
Multiple R	0.63
R Square	0.40
Adjusted R Square	0.40
Standard Error	0.18
Observations	359

	df	SS	MS	F-Ratio	Significance F
Regression	1	7.81	7.81	239.03	0.00
Residual	357	11.66	0.03		
Total	358	19.47			
	Coefficients	Standard Error		t Stat	P-value
Intercept	-0.01	0.01		-0.66	0.51
Model	0.58	0.04		15.46	0.00

Zone 6: Jupiter Rainfall Cycle Model

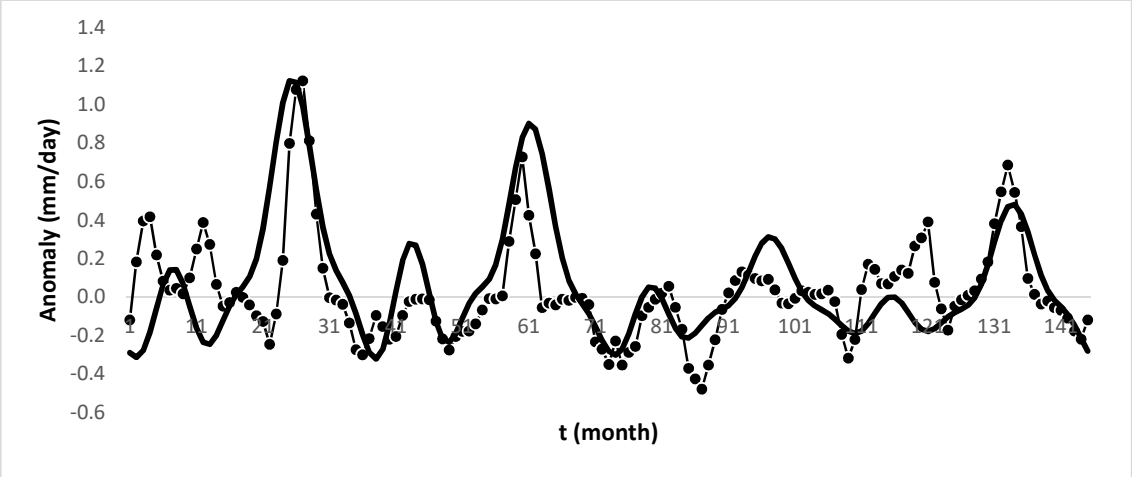

Figure 48: Variation of the mean Rainfall Anomaly (mm/day) and the fitted model (bold curve) in the Jupiter 12-year cycle beginning at Jupiter in Opposition phase in January.

The fitted curve;

$$RR_{\mathbf{4}}(t) == [0.1\,sin\big(0.0436(t)\big) + 0.3\,sin\big(0.1744(t + 20)\big) + 0.05\,sin\big(1.3949(t + 16)\big) + 0.25\,sin\big(0.3487(t + 15)\big) + 0.1\,sin\big(0.6974(t + 13)\big)] * [1 + 0.8\,sin\big(0.0436(t + 5)\big)]*0.65 \quad (78)$$

The statistical summary of the relationship between the fitted curve and the rainfall anomaly;

Regression Statistics	
Multiple R	0.62
R Square	0.38
Adjusted R Square	0.38
Standard Error	0.21
Observations	143

	df	SS	MS	F-Ratio	Significance F
Regression	1	3.80	3.80	87.35	0.00
Residual	141	6.13	0.04		
Total	142	9.94			
	Coefficients	Standard Error		t Stat	P-value
Intercept	-0.007	0.018		-0.406	0.685
Model	0.525	0.056		9.346	0.000

Zone 6: Mars Rainfall Cycle Model

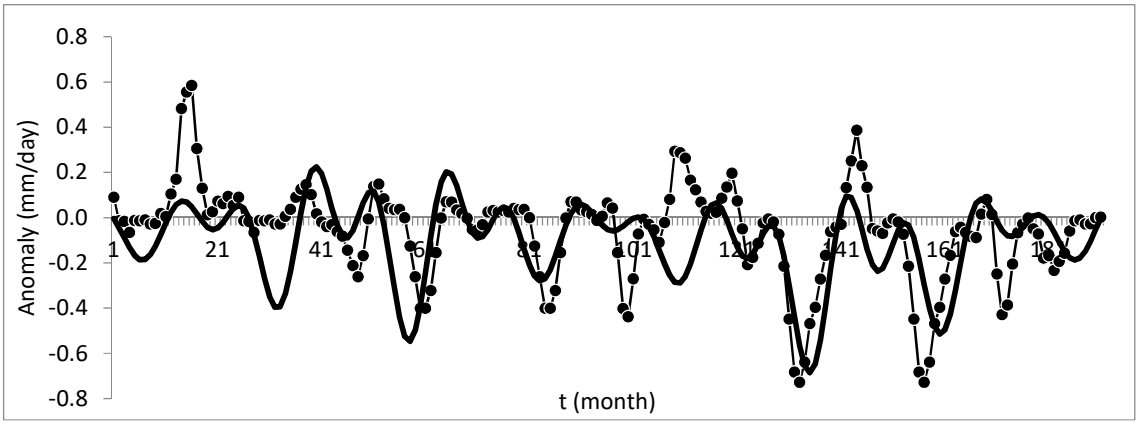

Figure 49: Variation of the mean Rainfall Anomaly (mm/day) and the fitted model (bold curve) in the Mars 15-year cycle beginning at Mars in Opposition phase in January.

The fitted curve;

$$RR_{\boldsymbol{\sigma}}(t) == 0.05\sin\big(0.035(t)\big) + 0.15\sin(0.2449(t - 12)) + 0.15\sin\big(0.4899(t-10)\big) - 0.1] * [1 + 0.8\sin\big(0.07(t+60)\big)]*0.7 \quad (79)$$

The statistical summary of the relationship between the fitted curve and the rainfall anomaly;

Regression Statistics	
Multiple R	0.51
R Square	0.26
Adjusted R Square	0.25
Standard Error	0.18
Observations	179

	df	SS	MS	F-Ratio	Significance F
Regression	1	2.04	2.04	61.22	0.00
Residual	177	5.90	0.03		
Total	178	7.95			
	Coefficients	Standard Error	t Stat	P-value	
Intercept	0.01	0.02	0.45	0.65	
Model	0.60	0.08	7.82	0.00	

Zone 6: Venus Rainfall Cycle Model

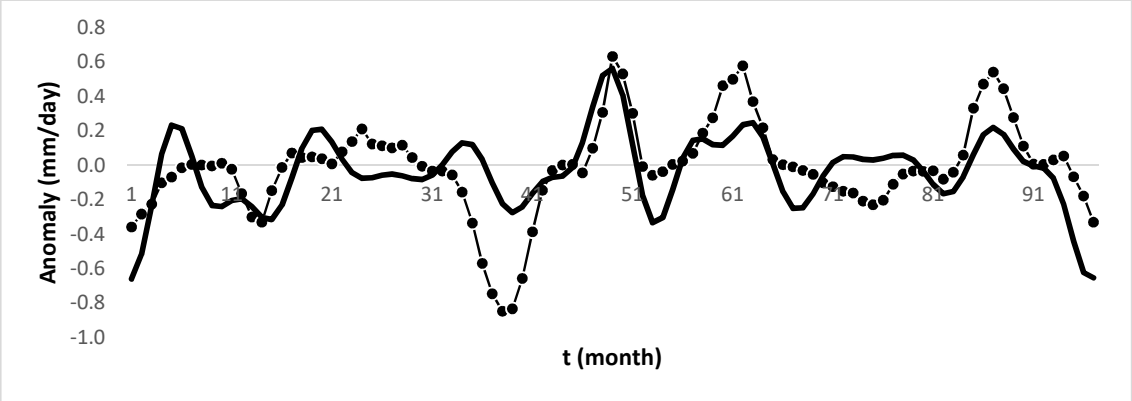

Figure 50: Variation of the mean Rainfall Anomaly (mm/day) and the fitted model (bold curve) in the Venus 8-year cycle beginning at Venus in inferior conjunction phase in January.

The fitted curve;

$$RR_{♀}(t) = [0.1\,sin\big(0.0655(t-35)\big) + 0.1\,sin\big(0.1966(t+20)\big) + 0.35\,\sin\big(0.4586(\mathrm{t}-3)\big) + 0.2\,\sin\big(0.8518(\mathrm{t}-3)\big)] * [\,1 + 0.8\,\sin\big(0.1310(\mathrm{t}-40)\big)] \quad (80)$$

The statistical summary of the relationship between the fitted curve and the rainfall anomaly;

Regression Statistics	
Multiple R	0.55
R Square	0.31
Adjusted R Square	0.30
Standard Error	0.22
Observations	95

	df	SS	MS	F-Ratio	Significance F
Regression	1	2.08	2.08	41.29	0.00
Residual	93	4.68	0.05		
Total	94	6.76			
	Coefficients	Standard Error		t Stat	P-value
Intercept	0.01	0.02		0.54	0.59
Model	0.74	0.12		6.43	0.00

Zone 7: Saturn Rainfall Cycle Model

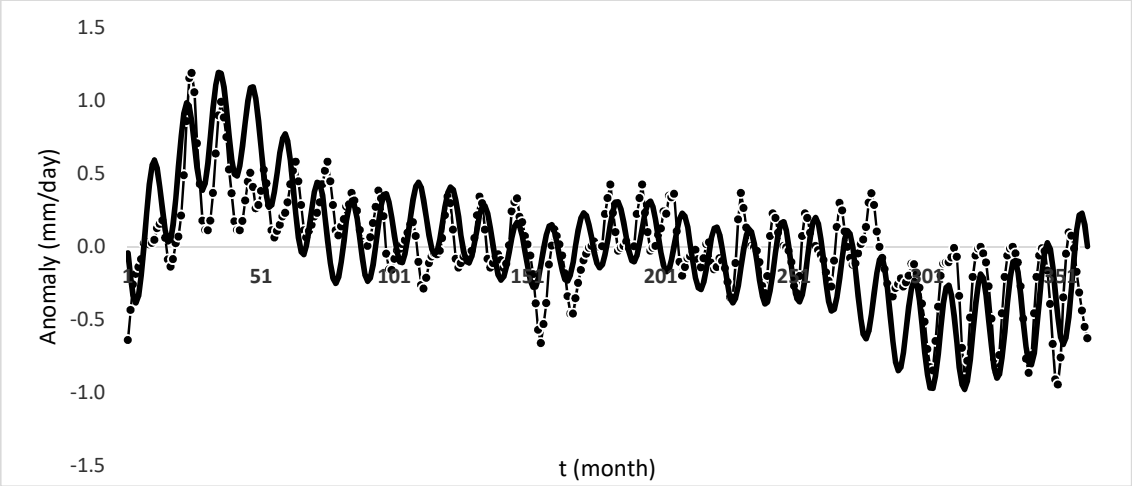

Figure 51: Variation of the mean Rainfall Anomaly (mm/day) and the fitted model (bold curve) in the Saturn 30-year cycle beginning at Saturn in Opposition phase in January.

The fitted curve;

$$RR_{\text{ħ}}(t) = [0.25\sin(0.0174t) + 0.2\sin\big(0.0349(t+5)\big) + 0.1\sin\big(0.0872(t-25)\big) + 0.1\sin(0.0523t) + 0.07\sin\big(0.0698(t-5)\big) + 0.25\sin(0.5058(t+5))] * [1 + 0.6\sin\big(0.01744(t+100)\big)]*0.6 \quad (81)$$

The statistical summary of the relationship between the fitted curve and the rainfall anomaly;

Regression Statistics	
Multiple R	0.71
R Square	0.50
Adjusted R Square	0.50
Standard Error	0.23
Observations	359

	df	SS	MS	F-Ratio	Significance F
Regression	1	18.66	18.66	359.49	0.00
Residual	357	18.53	0.05		
Total	358	37.19			
	Coefficients	Standard Error		t Stat	P-value
Intercept	0.00	0.01		0.17	0.86
Model	0.55	0.03		18.96	0.00

Zone 7: Jupiter Rainfall Cycle Model

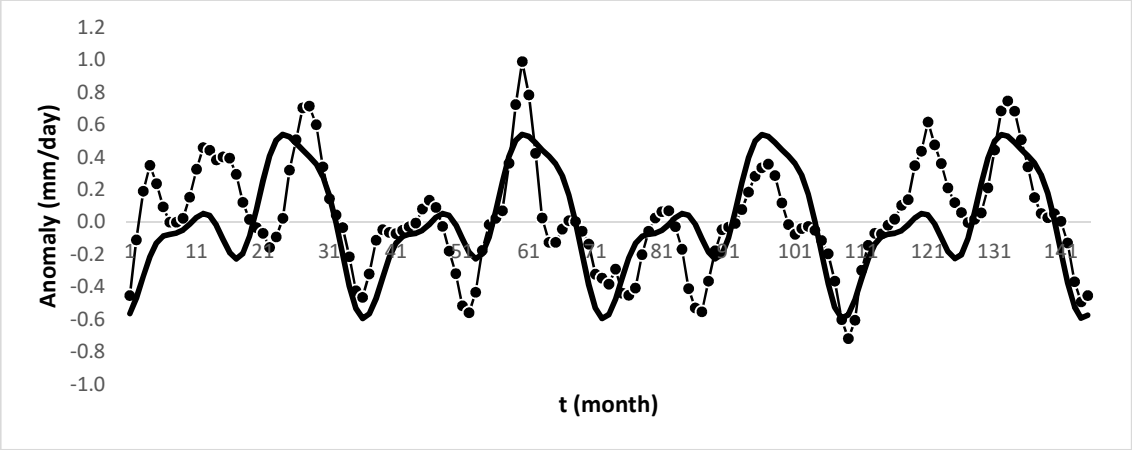

Figure 52: Variation of the mean Rainfall Anomaly (mm/day) and the fitted model (bold curve) in the Jupiter 12-year cycle beginning at Jupiter in Opposition phase in January.

The fitted curve;

$$RR_{\mathbf{4}}(t) = 0.1\sin\big(0.1744(t)\big) + 0.4\sin\big(0.1744(t-15)\big) + 0.3\sin\big(0.3487(t-4)\big) + 0.1\sin\big(0.6974(t-2)\big) \quad (82)$$

The statistical summary of the relationship between the fitted curve and the rainfall anomaly;

Regression Statistics	
Multiple R	0.66
R Square	0.43
Adjusted R Square	0.43
Standard Error	0.24
Observations	143

	df	SS	MS	F	Significance F
Regression	1	6.41	6.41	107.60	0.00
Residual	141	8.40	0.06		
Total	142	14.81			
	Coefficients	Standard Error	t Stat	P-value	
Intercept	0.03	0.02	1.59	0.11	
Model	0.67	0.06	10.37	0.00	

Zone 7: Mars Rainfall Cycle Model

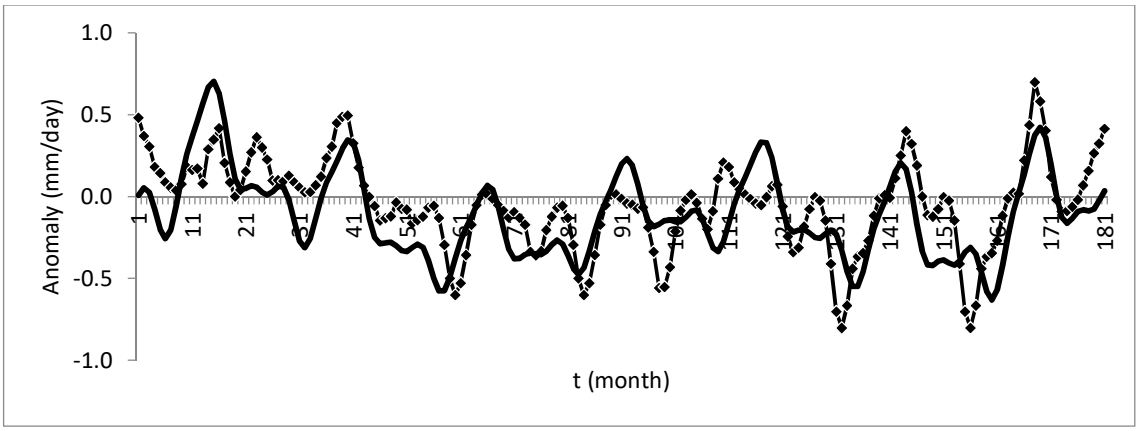

Figure 53 Variation of the mean Rainfall Anomaly (mm/day) and the fitted model (bold curve) in the Mars 15-year cycle beginning at Mars in Opposition phase in January.

The fitted curve;

$$RR_{\boldsymbol{\sigma}}(t) = 0.1\ sin\big(0.035(t+40)\big) + 0.15\ sin(0.07(t+5)) + 0.05\ sin\big(0.9797(t+18)\big) + 0.15\ sin(0.4899(t+15)) + 0.2\ sin(0.2449(t+17)) - 0.1 \quad (83)$$

The statistical summary of the relationship between the fitted curve and the rainfall anomaly;

Regression Statistics	
Multiple R	0.65
R Square	0.42
Adjusted R Square	0.42
Standard Error	0.20
Observations	179

	df	SS	MS	F-Ratio	Significance F
Regression	1	5.34	5.34	127.74	0.00
Residual	177	7.40	0.04		
Total	178	12.74			
	Coefficients	Standard Error	t Stat	P-value	
Intercept	0.02	0.02	1.10	0.27	
Model	0.66	0.06	11.30	0.00	

Zone 7: Venus Rainfall Cycle Model

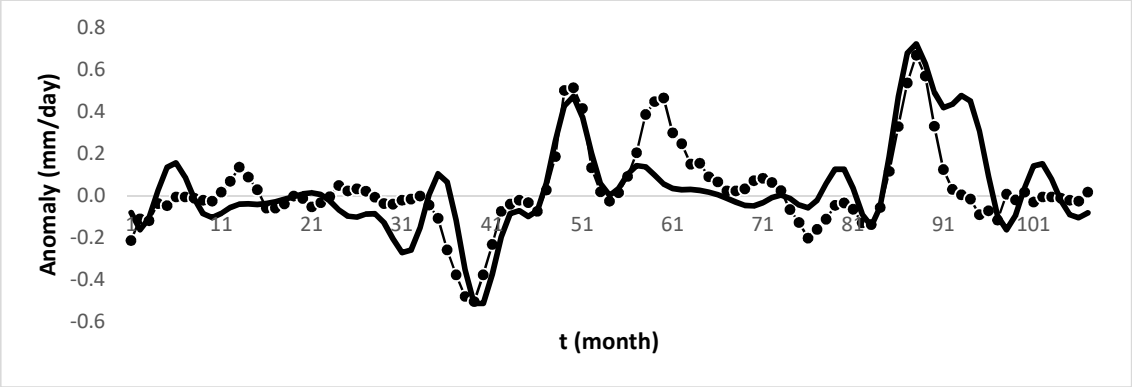

Figure 54: Variation of the mean Rainfall Anomaly (mm/day) and the fitted model (bold curve) in the Venus 8-year cycle beginning at Venus in inferior conjunction phase in January.

The fitted curve;

$$RR_{♀}(t) = [0.1\,sin\big(0.0655(t-50)\big) + 0.1\,sin\big(0.131(t+12)\big) + 0.1\,sin\big(0.1966(t+15)\big) + 0.1\,sin\big(0.4586(t - 4)\big) + 0.1\,sin\big(0.8518(t-4)\big) - 0.1] * [1 + sin\big(0.1310(t-30)\big)] \quad (84)$$

The statistical summary of the relationship between the fitted curve and the rainfall anomaly;

Regression Statistics	
Multiple R	0.72
R Square	0.52
Adjusted R Square	0.51
Standard Error	0.14
Observations	95

	df	SS	MS	F	Significance F
Regression	1	2.04	2.04	99.14	0.00
Residual	93	1.91	0.02		
Total	94	3.95			
	Coefficients	Standard Error	t Stat	P-value	
Intercept	0.01	0.01	0.69	0.49	
Model	0.59	0.06	9.96	0.00	

Zone 8: Saturn Rainfall Cycle Model

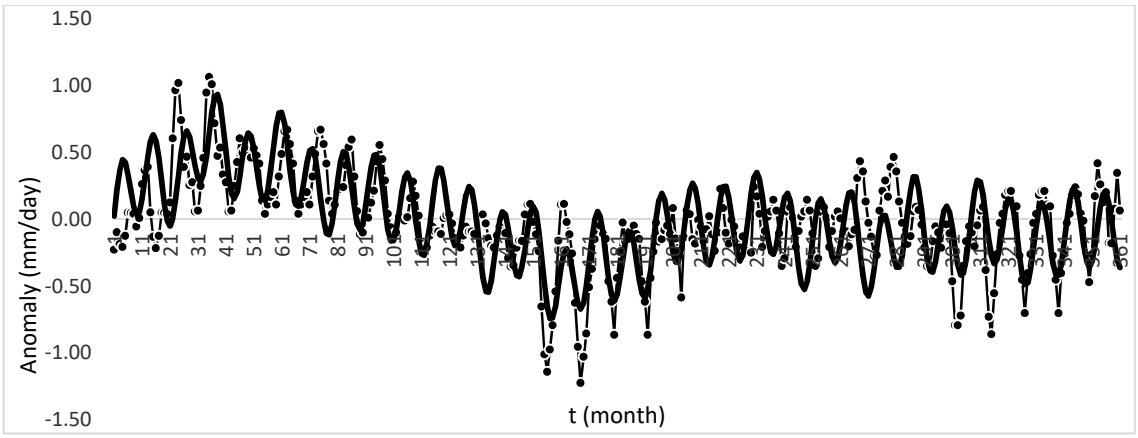

Figure 55: Variation of the mean Rainfall Anomaly (mm/day) and the fitted model (bold curve) in the Saturn 30-year cycle beginning at Saturn in Opposition phase in January.

The fitted curve;

$$RR_{♄}(t) = 0.25\,sin(0.0174(t+50)) + 0.1\,sin\big(0.0698(t-10)\big) + 0.3\,sin\big(0.5581(t-1)\big) + 0.2\,sin(0.0349(t-10)) + 0.05\,sin\big(0.2790(t-7)\big) + 0.1\,sin\,(0.2267(t-1)) \quad (85)$$

The statistical summary of the relationship between the fitted curve and the rainfall anomaly;

Regression Statistics	
Multiple R	0.55
R Square	0.31
Adjusted R Square	0.30
Standard Error	0.28
Observations	359

	df	SS	MS	F-ratio	Significance F
Regression	1	12.68	12.68	157.03	0.00
Residual	357	28.82	0.08		
Total	358	41.49			
	Coefficients	Standard Error		t Stat	P-value
Intercept	-0.02	0.01		-1.11	0.27
Model	0.57	0.05		12.53	0.00

Zone 8: Jupiter Rainfall Cycle Model

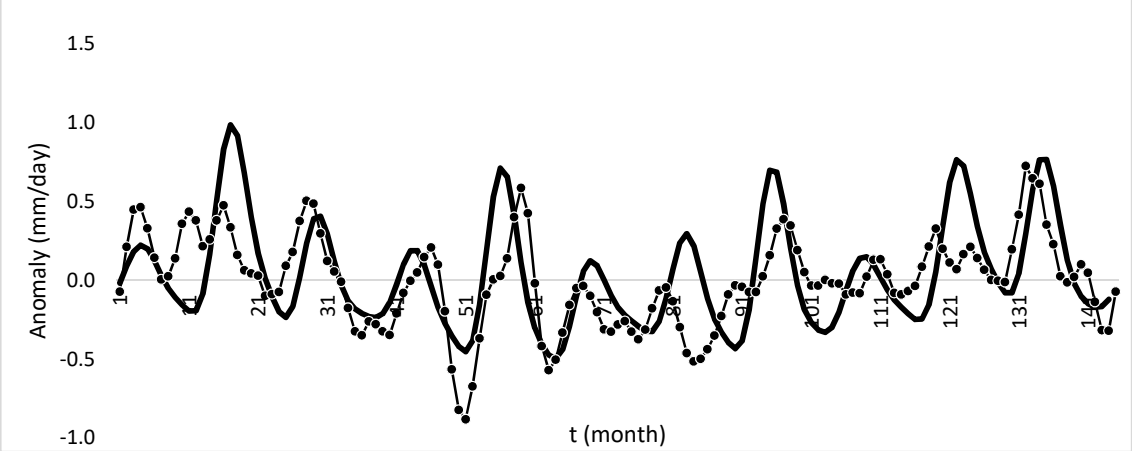

Figure 56: Variation of the mean Rainfall Anomaly (mm/day) and the fitted model (bold curve) in the Jupiter 12-year cycle beginning at Jupiter in Opposition phase in January.

The fitted curve;

$$RR_{\mathbf{4}}(t) = [0.1\,sin\big(0.0436(t+38)\big) + 0.25\,sin\big(0.4795(t-14)\big) + 0.05\,sin\big(0.959(t-15)\big)] * [(1 + 0.8\,sin\big(0.1744(t+25)\big)] \quad (86)$$

The statistical summary of the relationship between the fitted curve and the rainfall anomaly;

Regression Statistics	
Multiple R	0.50
R Square	0.25
Adjusted R Square	0.25
Standard Error	0.25
Observations	144

	df	SS	MS	F-Ratio	Significance F
Regression	1	3.01	3.01	47.48	0.00
Residual	142	9.00	0.06		
Total	143	12.01			
	Coefficients	Standard Error		t Stat	P-value
Intercept	0.00	0.02		0.16	0.87
Model	0.64	0.09		6.89	0.00

Zone 8: Mars Rainfall Cycle Model

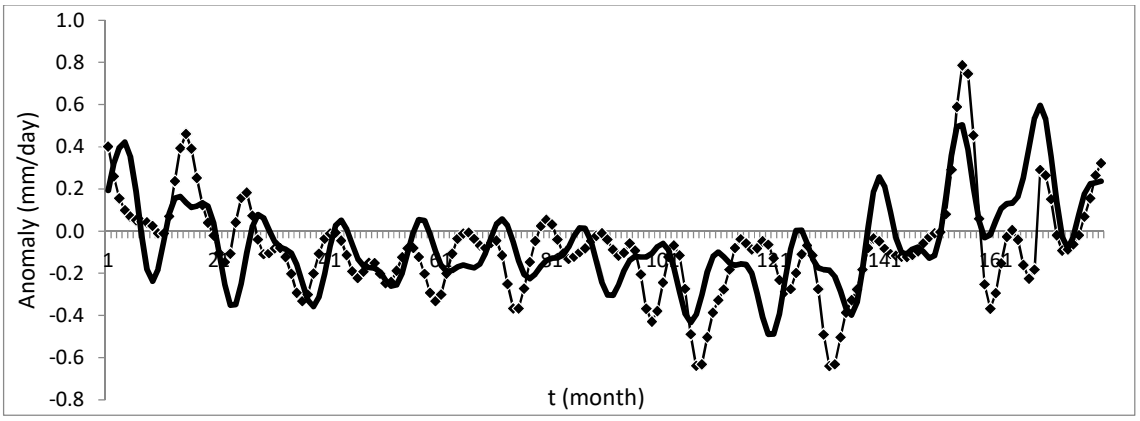

Figure 57: Variation of the mean Rainfall Anomaly (mm/day) and the fitted model (bold curve) in the Mars 15-year cycle beginning at Mars in Opposition phase in January.

The fitted curve;

$$RR_{\sigma}(t) = [0.2\,sin\big(0.035(t+50)\big) + 0.1\,sin(0.07(t+35)) + 0.2\,sin\big(0.4549(t+1)\big) + 0.1\,sin\big(0.8398(t-3)\big) - 0.1] * [1 + 0.6\,sin(0.035(t+60))] * 0.6 \quad (87)$$

The statistical summary of the relationship between the fitted curve and the rainfall anomaly;

Regression Statistics	
Multiple R	0.597
R Square	0.357
Adjusted R Square	0.353
Standard Error	0.177
Observations	180

	df	SS	MS	F-Ratio	Significance F
Regression	1	3.108	3.108	98.748	0.000
Residual	178	5.603	0.031		
Total	179	8.711			
	Coefficients	Standard Error		t Stat	P-value
Intercept	-0.050	0.014		-3.650	0.000
Model	0.631	0.064		9.937	0.000

Zone 8: Venus Rainfall Cycle Model

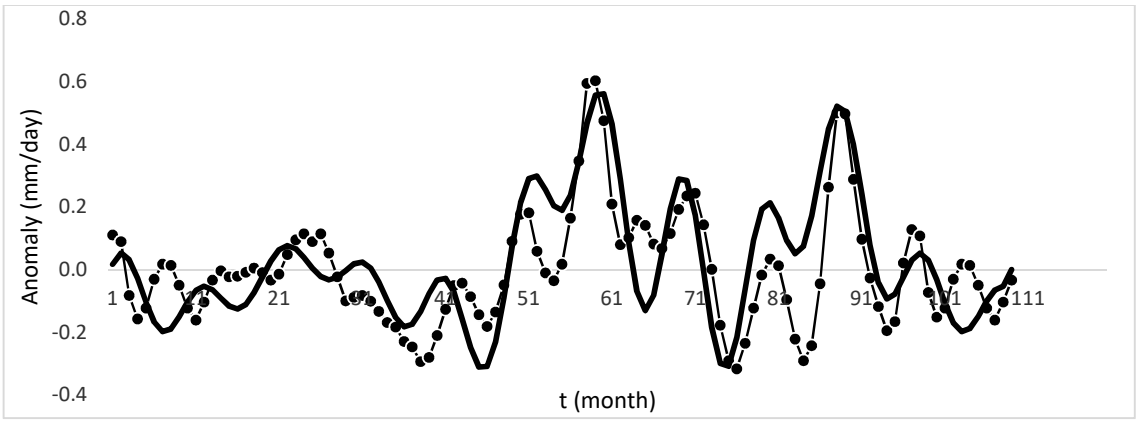

Figure 58: Variation of the mean Rainfall Anomaly (mm/day) and the fitted model (bold curve) in the Venus 8-year cycle beginning at Venus in inferior conjunction phase in January.

The fitted curve;

$$RR_{♀}(t) = [0.1\sin(0.3929(t-3)) + 0.2\sin(0.0655(t-47)) + 0.25\sin(0.6548(t-48)) + 0.3\sin(0.1964(t-49)) - 0.1] * [1 + \sin(0.0.0655(t+50))] * 0.4 \quad (88)$$

The statistical summary of the relationship between the fitted curve and the rainfall anomaly;

Regression Statistics	
Multiple R	0.752
R Square	0.565
Adjusted R Square	0.561
Standard Error	0.125
Observations	96

	df	SS	MS	F	Significance F
Regression	1	1.926	1.926	122.309	0.000
Residual	94	1.480	0.016		
Total	95	3.407			
	Coefficients	Standard Error		t Stat	P-value
Intercept	-0.024	0.013		-1.813	0.073
Model	0.694	0.063		11.059	0.000

Zone 9: Saturn Rainfall Cycle Model

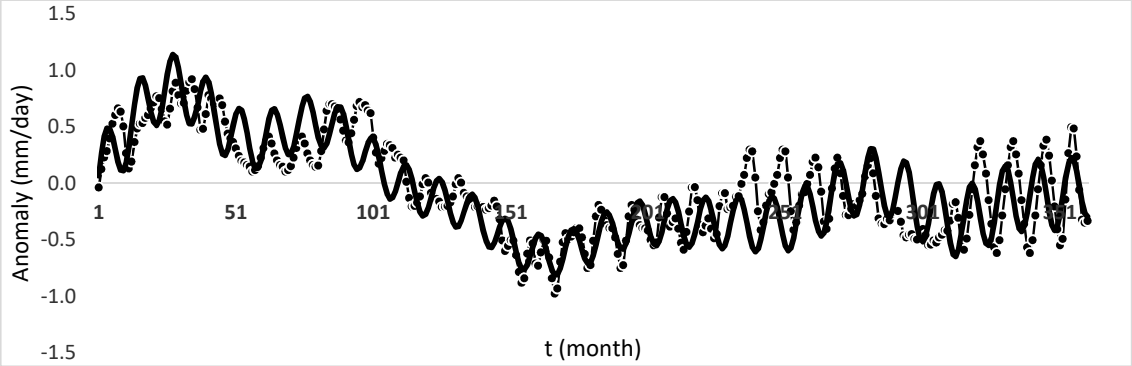

Figure 59: Variation of the mean Rainfall Anomaly (mm/day) and the fitted model (bold curve) in the Saturn 30-year cycle beginning at Saturn in Opposition phase in January.

The fitted curve;

$$RR_{\mathfrak{h}}(t) = 0.6\sin(0.0174(t+60)) + 0.35\sin\big(0.03488(t-15)\big) + 0.1\sin\big(0.1221(t-15)\big) + 0.1\sin(0.1046(t+50)) + 0.15\sin\big(0.6976(t+5)\big) + 0.3\sin(0.5232(t-1))] * [1 + 0.4\sin(0.0173(t+120))] * 0.55 \quad (89)$$

The statistical summary of the relationship between the fitted curve and the rainfall anomaly;

Regression Statistics	
Multiple R	0.77
R Square	0.59
Adjusted R Square	0.59
Standard Error	0.27
Observations	360

	df	SS	MS	F-Ratio	Significance F
Regression	1	37.33	37.33	523.45	0.00
Residual	358	25.53	0.07		
Total	359	62.87			

	Coefficients	Standard Error	t Stat	P-value
Intercept	-0.02	0.01	-1.24	0.22
Model	0.72	0.03	22.88	0.00

Zone 9: Jupiter Rainfall Cycle Model

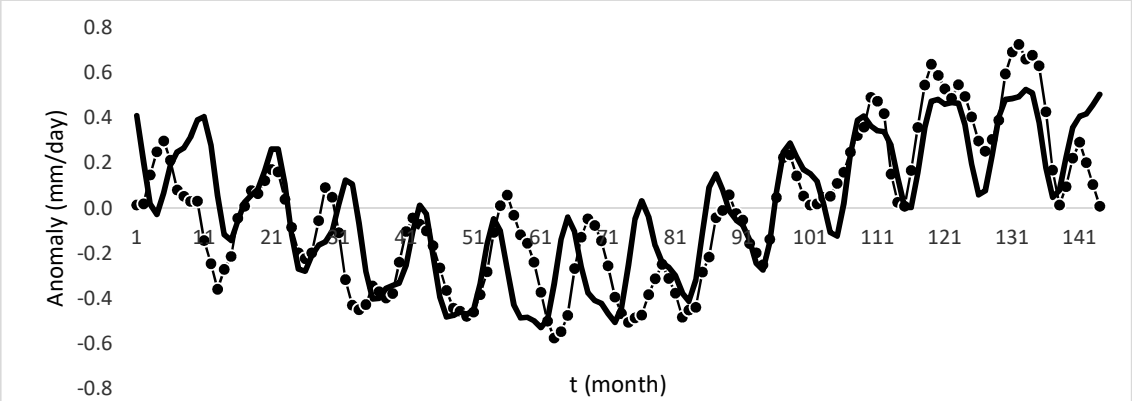

Figure 60: Variation of the mean Rainfall Anomaly (mm/day) and the fitted model (bold curve) in the Jupiter 12-year cycle beginning at Jupiter in Opposition phase in January.

The fitted curve;

$$RR_{\mathbf{4}}(t) = 0.35\sin\big(0.0436(t+50)\big) + 0.22\sin\big(0.5667(t-7)\big) + 0.08\sin\big(1.1769(t+6)\big) \quad (90)$$

The statistical summary of the relationship between the fitted curve and the rainfall anomaly;

Regression Statistics	
Multiple R	0.79
R Square	0.62
Adjusted R Square	0.62
Standard Error	0.20
Observations	144

	df	SS	MS	F-Ratio	Significance F
Regression	1	8.95	8.95	230.18	0.00
Residual	142	5.52	0.04		
Total	143	14.468			
	Coefficients	Standard Error		t Stat	P-value
Intercept	-0.018	0.016		-1.090	0.277
Model	0.840	0.055		15.172	0.000

Zone 9: Mars Rainfall Cycle Model

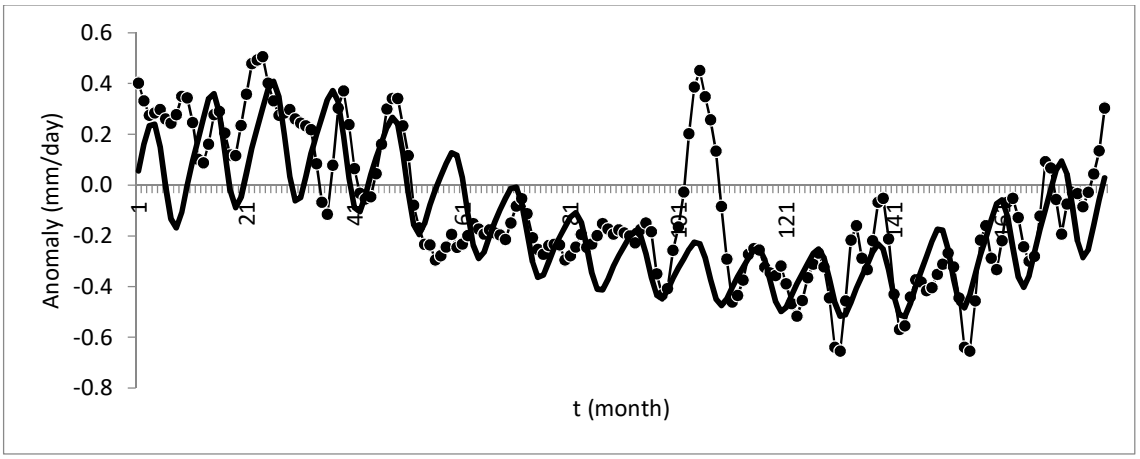

Figure 61: Variation of the mean Rainfall Anomaly (mm/day) and the fitted model (bold curve) in the Mars 15-year cycle beginning at Mars in Opposition phase in January.

The fitted curve;

$$RR_{\sigma}(t) = [0.5\sin\big(0.035(t+17)\big) + 0.05\sin\big(1.1197(t-3)\big) + 0.25\sin(0.5598t) - 0.3] * [1 + 0.5\sin(0.035(t+25))] * 0.45 \quad (91)$$

The statistical summary of the relationship between the fitted curve and the rainfall anomaly;

Regression Statistics	
Multiple R	0.763
R Square	0.583
Adjusted R Square	0.580
Standard Error	0.177
Observations	180

	df	SS	MS	F-Ratio	Significance F
Regression	1	7.786	7.786	248.591	0.000
Residual	178	5.575	0.031		
Total	179	13.362			
	Coefficients	Standard Error		t Stat	P-value
Intercept	-0.012	0.014		-0.828	0.409
Model	0.807	0.051		15.767	0.000

Zone 9: Venus Rainfall Cycle Model

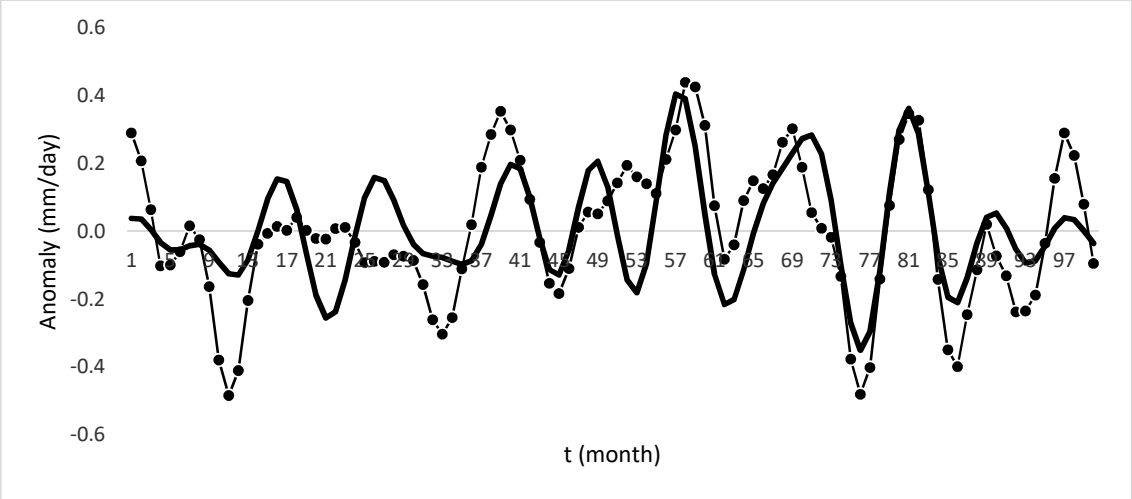

Figure 62: Variation of the mean Rainfall Anomaly (mm/day) and the fitted model (bold curve) in the Venus 8-year cycle beginning at Venus in inferior conjunction phase in January.

The fitted curve;

$$RR_{♀}(t) = [0.2\sin\big(0.7862(t-23)\big) + 0.1\sin\big(0.0655(t-35)\big) + 0.25\sin\big(0.5897(t-35)\big) + 0.2\sin\big(0.4586(t-11)\big)] * [\ 1 + 0.4\sin\big(0.0655(t-40)\big)] * 0.5 \quad (92)$$

The statistical summary of the relationship between the fitted curve and the rainfall anomaly;

Regression Statistics	
Multiple R	0.69
R Square	0.48
Adjusted R Square	0.48
Standard Error	0.15
Observations	95

	df	SS	MS	F-Ratio	Significance F
Regression	1	1.90	1.90	86.89	0.00
Residual	93	2.03	0.02		
Total	94	3.93			
	Coefficients	Standard Error		t Stat	P-value
Intercept	-0.02	0.02		-1.07	0.29
Model	0.89	0.10		9.32	0.00

Zone 10: Saturn Rainfall Cycle Model

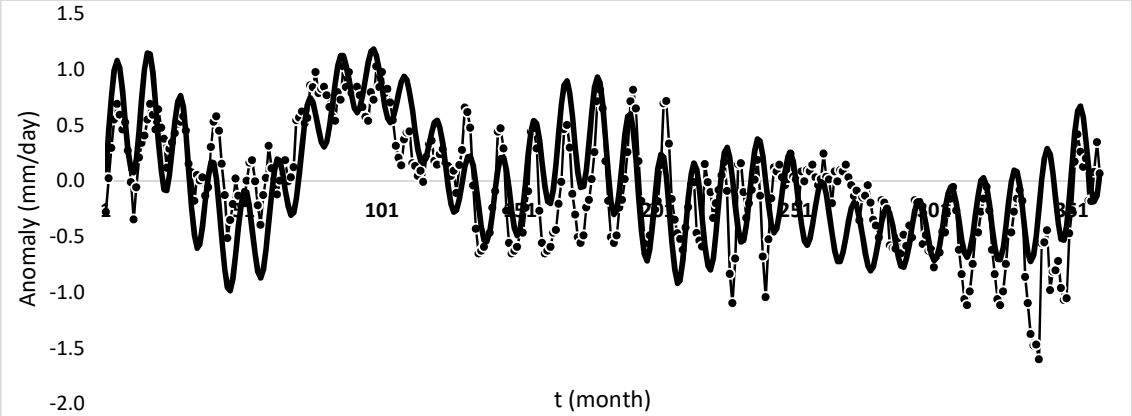

Figure 63: Variation of the mean Rainfall Anomaly (mm/day) and the fitted model (bold curve) in the Saturn 30-year cycle beginning at Saturn in Opposition phase in January.

The fitted curve;

$$RR_{\text{ħ}}(t) = 0.4\sin(0.0174(t-10)) + 0.25\sin\big(0.0872(t-5)\big) + 0.25\sin\big(0.0698(t+20)\big) + 0.25\sin(0.0523(t+45)) + 0.35\sin\big(0.5406(t-2)\big)] * [1 + 0.5\sin(0.0349(t+30))] * 0.8 \quad (93)$$

The statistical summary of the relationship between the fitted curve and the mean rainfall anomaly;

Regression Statistics	
Multiple R	0.69
R Square	0.47
Adjusted R Square	0.47
Standard Error	0.36
Observations	359

	df	SS	MS	F	Significance F
Regression	1	42.24	42.24	318.07	0.00
Residual	357	47.41	0.13		
Total	358	89.65			
	Coefficients	Standard Error		t Stat	P-value
Intercept	-0.04	0.02		-2.22	0.03
Model	0.67	0.04		17.83	0.00

Zone 10: Jupiter Rainfall Cycle Model

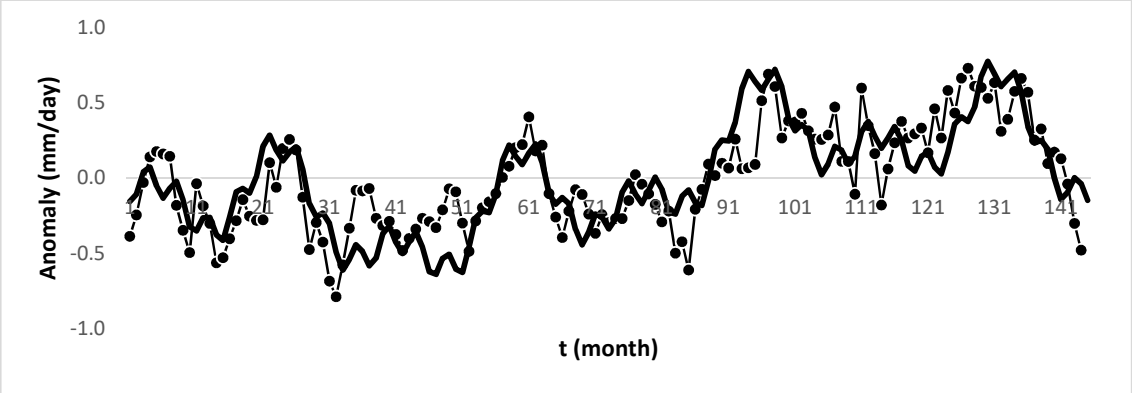

Figure 64: Variation of the Mean Rainfall Anomaly (mm/day) and the fitted model (bold curve) in the Jupiter 12-year cycle beginning at Jupiter in Opposition phase in January.

The fitted curve;

$$RR_{\mathbf{4}}(t) = 0.35\sin\big(0.0436(t+65)\big) + 0.2\sin\big(0.3487(t-19)\big) + 0.1\sin\big(1.3949(t-16)\big) + 0.25\sin\big(0.1744(t-15)\big) \quad (94)$$

he statistical summary of the relationship between the fitted model curve and the mean rainfall anomaly

Regression Statistics	
Multiple R	0.77
R Square	0.59
Adjusted R Square	0.59
Standard Error	0.22
Observations	144.00

	df	SS	MS	F	Significance F
Regression	1	9.8	9.8	207.9	0.00
Residual	142	6.7	0.0		
Total	143	16.5			
	Coefficients	Standard Error	t Stat	P-value	
Intercept	0.00	0.02	-0.27	0.78	
Model	0.76	0.05	14.42	0.00	

Zone 10: Mars Rainfall Cycle Model

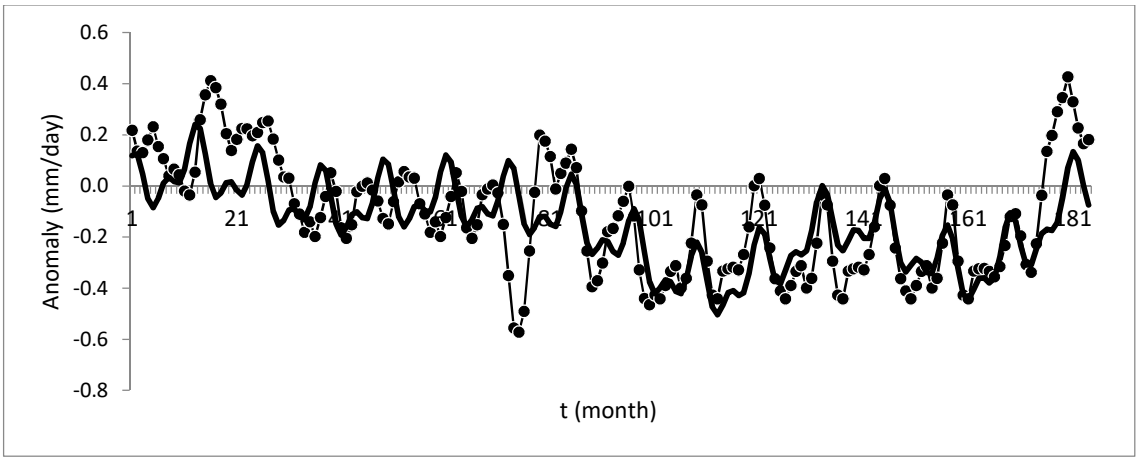

Figure 65: Variation of the mean Rainfall Anomaly (mm/day) and the fitted model (bold curve) in the Mars 15-year cycle beginning at Mars in Opposition phase in January.

The fitted curve;

$$RR_{\boldsymbol{\sigma}}(t) = 0.15\sin\big(0.035(t+10)\big) + 0.1\sin(0.105t) + 0.05\sin(0.14(t+6)) + 0.1\sin(0.5249(t-10)) + 0.07\sin\big(1.0497(t-12)\big) \quad (95)$$

The statistical summary of the relationship between the fitted curve and the rainfall anomaly;

Regression Statistics	
Multiple R	0.68
R Square	0.46
Adjusted R Square	0.45
Standard Error	0.16
Observations	179

	df	SS	MS	F	Significance F
Regression	1	4.01	4.01	148.76	0.00
Residual	177	4.77	0.03		
Total	178	8.77			

	Coefficients	Standard Error	t Stat	P-value
Intercept	0.02	0.02	1.11	0.27
Model	0.95	0.08	12.20	0.00

Zone 10: Venus Rainfall Cycle Model

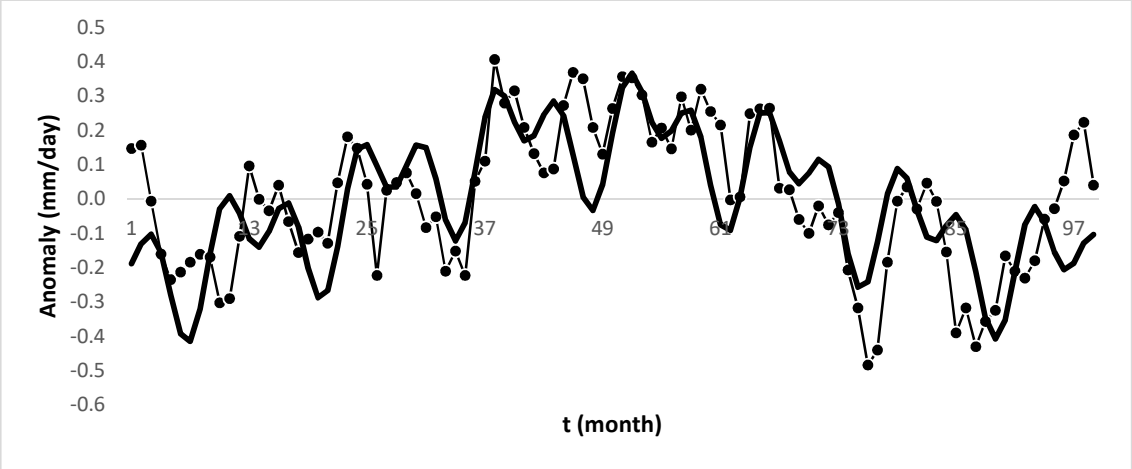

Figure 66: Variation of the mean Rainfall Anomaly (mm/day) and the fitted model (bold curve) in the Venus 8-year cycle beginning at Venus in inferior conjunction phase in January.

The fitted curve;

$$RR_{♀}(t) = 0.2\sin\big(0.0655(t-25)\big) + 0.12\sin\big(0.4584(t-37)\big) + 0.12\sin\big(0.9167(t-36)\big) - 0.1 \quad (96)$$

The statistical summary of the relationship between the fitted curve and the rainfall anomaly;

Regression Statistics	
Multiple R	0.70
R Square	0.50
Adjusted R Square	0.49
Standard Error	0.15
Observations	96

	df	SS	MS	F	Significance F
Regression	1	2.1	2.1	92.6	0.00
Residual	94	2.1	0.0		
Total	95	4.1			

	Coefficients	Standard Error	t Stat	P-value
Intercept	0.00	0.02	-0.08	0.93
X Variable 1	0.79	0.08	9.62	0.00

Zone 11: Saturn Rainfall Cycle Model

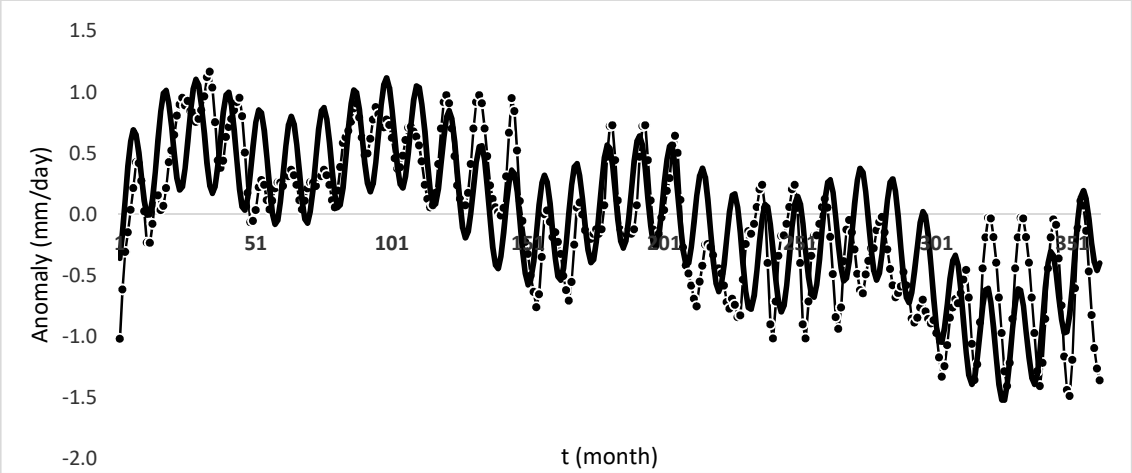

Figure 67: Variation of the mean Rainfall Anomaly (mm/day) and the fitted model (bold curve) in the Saturn 30-year cycle beginning at Saturn in Opposition phase in January.

The fitted curve;

$$RR_{\text{♄}}(t) = 0.5\sin(0.0174(t-10)) + 0.3\sin\big(0.0349(t-10)\big) + 0.15\sin\big(0.0523(t+3)\big) + 0.3\sin(0.0698(t+8)) + 0.45\sin\big(0.5406(t-3)\big) \quad (97)$$

The statistical summary of the relationship between the fitted curve and the rainfall anomaly;

Regression Statistics	
Multiple R	0.74
R Square	0.55
Adjusted R Square	0.55
Standard Error	0.39
Observations	359

	df	SS	MS	F	Significance F
Regression	1	67.39	67.39	432.41	0.00
Residual	357	55.63	0.16		
Total	358	123.02			
	Coefficients	Standard Error		t Stat	P-value
Intercept	-0.05	0.02		-2.64	0.01
Model	0.76	0.04		20.79	0.00

Zone 11: Jupiter Rainfall Cycle Model

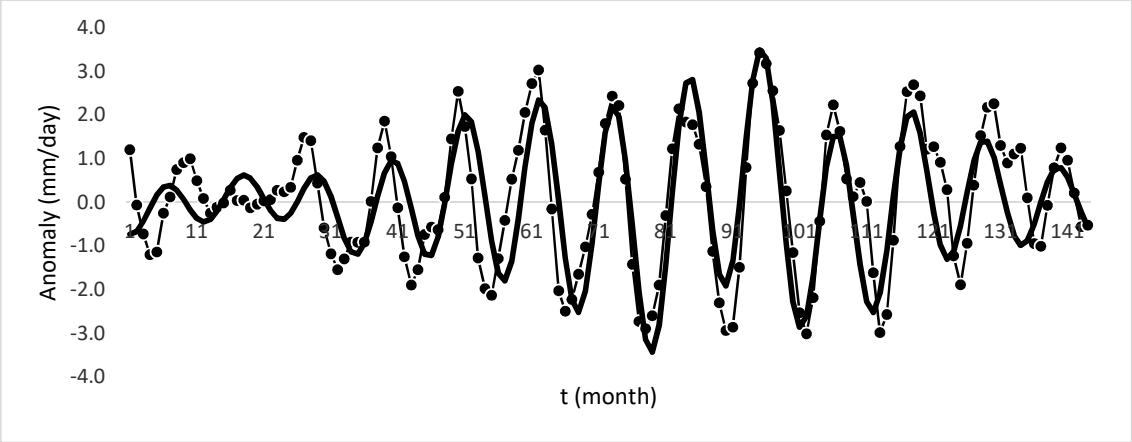

Figure 68: Variation of the mean Rainfall Anomaly (mm/day) and the fitted model (bold curve) in the Jupiter 12-year cycle beginning at Jupiter in Opposition phase in January.

The fitted curve;

$$RR_{\mathbf{4}}(t) = [0.35\sin(0.1744(t-10)) + 0.2\sin(0.2615(t-15)) + 0.15\sin(0.5667(t-4))] * [1 + 0.8\sin(0.0436(t-50))] \quad (98)$$

The statistical summary of the relationship between the fitted curve and the rainfall anomaly;

Regression Statistics	
Multiple R	0.79
R Square	0.63
Adjusted R Square	0.62
Standard Error	0.93
Observations	143

	df	SS	MS	F	Significance F
Regression	1	206.88	206.88	237.11	0.00
Residual	141	123.02	0.87		
Total	142	329.90			
	Coefficients	Standard Error	t Stat	P-value	
Intercept	0.08	0.08	1.05	0.30	
Model	0.88	0.06	15.40	0.00	

Zone 11: Mars Rainfall Cycle Model

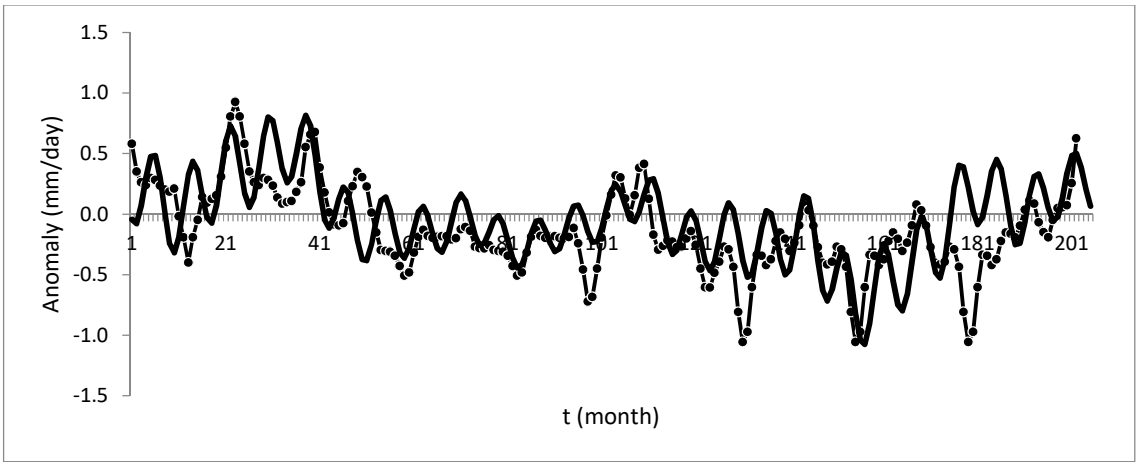

Figure 69: Variation of the mean Rainfall Anomaly (mm/day) and the fitted model (bold curve) in the Mars 15-year cycle beginning at Mars in Opposition phase in January.

The fitted curve;

$$RR_{\boldsymbol{\sigma}}(t) = [0.25\sin\big(0.035(t+10)\big) + 0.3\sin(0.07(t-2)) + 0.2\sin(0.175(t-25)) + 0.1\sin(0.35(t-15)) + 0.35\sin\big(0.77(t-20)\big)] * [1 + 0.5\sin\big(0.35(t+20)\big)] * 0.5 \quad (99)$$

The statistical summary of the relationship between the fitted curve and the rainfall anomaly;

Regression Statistics	
Multiple R	0.61
R Square	0.38
Adjusted R Square	0.37
Standard Error	0.28
Observations	179

	df	SS	MS	F-Ratio	Significance F
Regression	1	8.46	8.46	107.02	0.00
Residual	177	13.99	0.08		
Total	178	22.45			
	Coefficients	Standard Error	t Stat	P-value	
Intercept	-0.10	0.02	-4.74	0.00	
Model	0.62	0.06	10.35	0.00	

Zone 11: Venus Rainfall Cycle Model

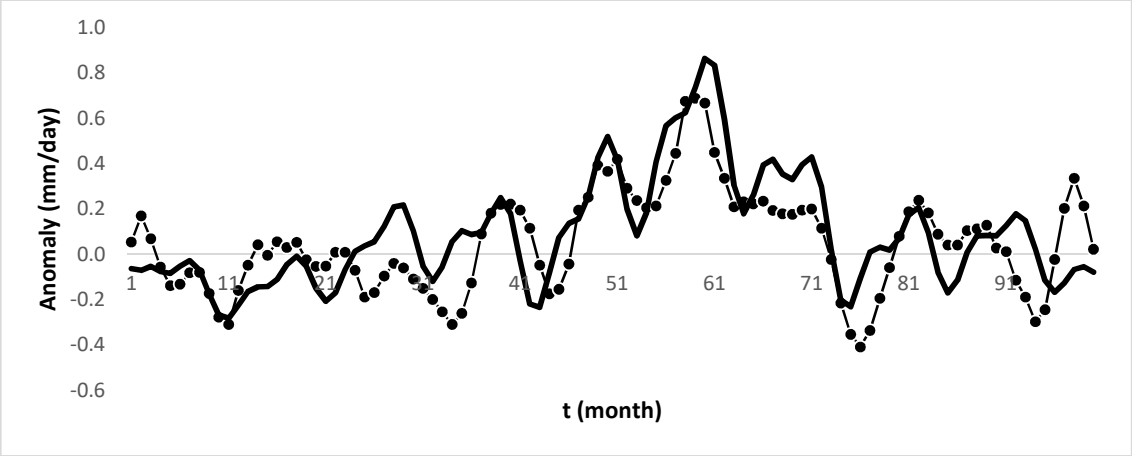

Figure 70: Variation of the mean Rainfall Anomaly (mm/day) and the fitted model (bold curve) in the Venus 8-year cycle beginning at Venus in inferior conjunction phase in January.

The fitted curve;

$$RR_{♀}(t) = 0.5\sin\big(0.0655(t-35)\big) + 0.35\sin\big(0.5897(t+18)\big) + 0.3\sin\big(0.1966(t+12)\big) + 0.2\sin\big(1.1794(t+15)\big)] * [1 + 0.7\sin\big(0.0655(t-35)\big)] * 0.3 \quad (100)$$

The statistical summary of the relationship between the fitted curve and the rainfall anomaly;

Regression Statistics	
Multiple R	0.77
R Square	0.60
Adjusted R Square	0.60
Standard Error	0.14
Observations	95

	df	SS	MS	F-Ratio	Significance F
Regression	1	2.90	2.90	139.75	0.00
Residual	93	1.93	0.02		
Total	94	4.84			
	Coefficients	Standard Error		t Stat	P-value
Intercept	-0.03	0.02		-1.57	0.12
Model	0.70	0.06		11.82	0.00

Zone 12: Mars Rainfall Cycle Model

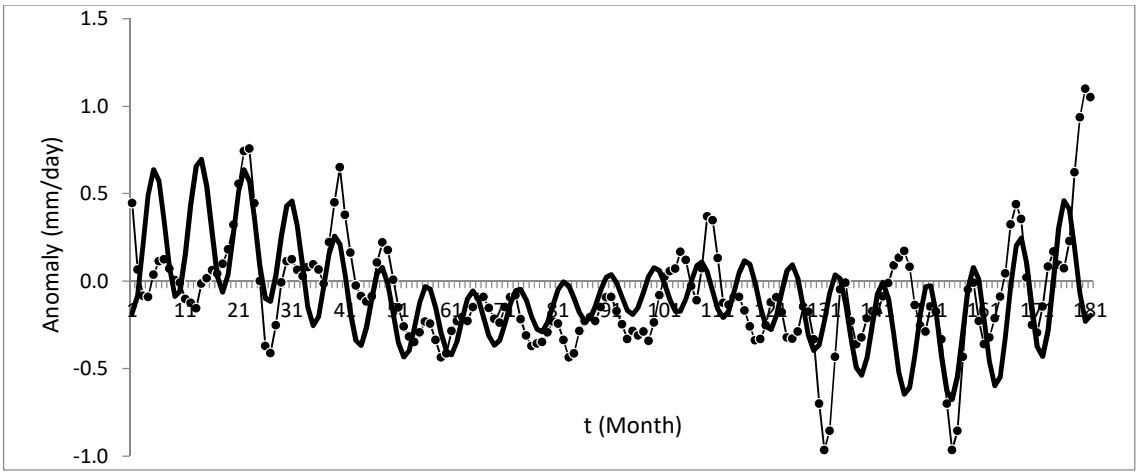

Figure 71: Variation of the mean Rainfall Anomaly (mm/day) and the fitted model curve in the Mars 15-year cycle beginning at Mars in Opposition phase in January.

The fitted curve;

$$RR_{\sigma} = \{0.2\sin\big(0.035(t+35)\big) + 0.25\sin\big(0.07(t+5)\big) + 0.35\sin\big(0.7348(t-3)\big)\} * \{1 + 0.8\sin\big(0.035(t+45)\big)\} * 0.5 - 0.15 \quad (101)$$

The statistical summary of the relationship between the fitted curve and the rainfall anomaly;

Regression Statistics	
Multiple R	0.45
R Square	0.21
Adjusted R Square	0.20
Standard Error	0.27
Observations	180

	df	SS	MS	F-Ratio	Critical F
Regression	1	3.28	3.28	46.27	0.00
Residual	178	12.63	0.07		
Total	179	15.91			
	Coefficients	Standard Error		t Stat	P-value
Intercept	-0.050	0.021		-2.418	0.017
Model	0.499	0.073		6.802	0.000

Zone 12: Jupiter Rainfall Cycle Model

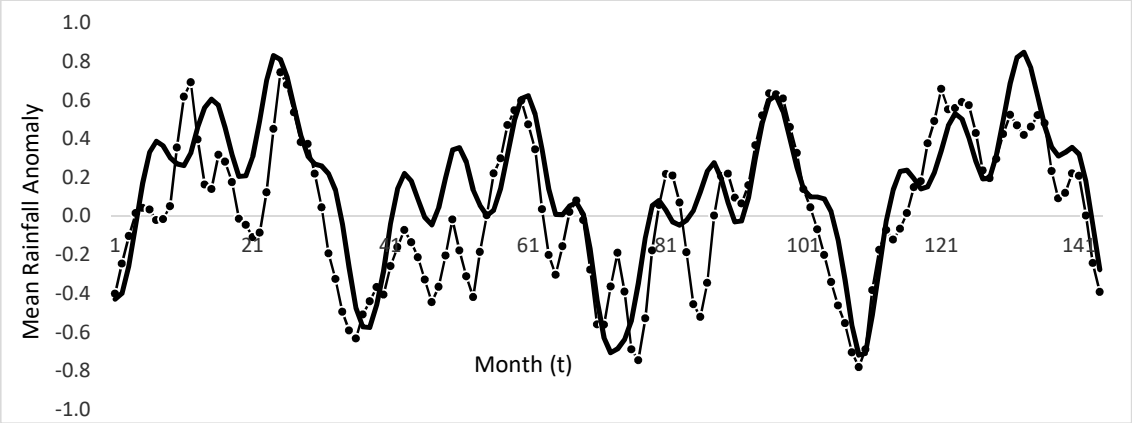

Figure 72: Variation of the mean Rainfall Anomaly (mm/day) and the fitted model curve in the Jupiter 12-year cycle beginning at Jupiter in Opposition phase in January.

The fitted curve;

$$RR_{\mathbf{4}} = 0.15\sin\big(0.0436(t+30)\big) + 0.3\sin\big(0.1744(t-12)\big) + 0.2\sin\big(0.3487(t-5)\big) + 0.2\sin\big(0.6974(t-4)\big) + 0.25\sin\big(1.3077(t-4)\big) \quad (102)$$

The statistical summary of the relationship between the fitted curve and the rainfall anomaly;

Regression Statistics	
Multiple R	0.802
R Square	0.643
Adjusted R Square	0.640
Standard Error	0.224
Observations	144

	df	SS	MS	F-Ratio	Critical F
Regression	1	12.78	12.78	255.45	0.00
Residual	142	7.10	0.05		
Total	143	19.88			
	Coefficients		Standard Error	t Stat	P-value
Intercept	-0.096		0.020	-4.734	0.000
Model	0.843		0.053	15.983	0.000

Zone 12: Venus Rainfall Cycle Model

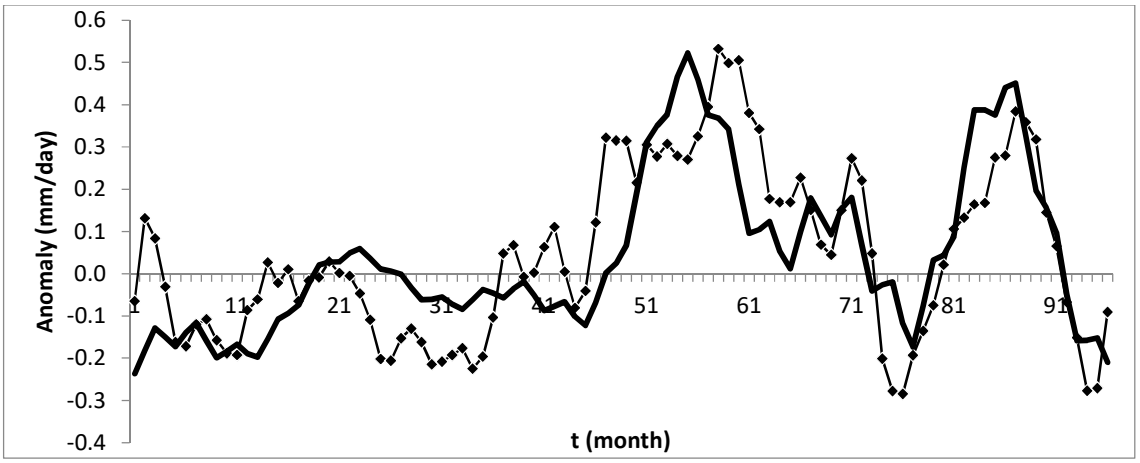

Figure 73: Variation of the mean Rainfall Anomaly (mm/day) and the fitted model curve in the Venus 8-year cycle beginning at Venus in inferior conjunction phase in January.

The fitted curve;

$$RR_{♀} = [0.2\sin(0.06554(t-40)) + 0.22\sin(0.1966(t-15)) + 0.15\sin(0.3931(t-2)) + 0.05\sin(1.5725(t+2))] * [1+\sin(0.0655(t-50))] * 0.5 \quad (103)$$

The statistical summary of the relationship between the fitted curve and the rainfall anomaly;

Regression Statistics	
Multiple R	0.73
R Square	0.54
Adjusted R Square	0.53
Standard Error	0.14
Observations	95

	df	SS	MS	F-Ratio	Critical F
Regression	1	2.13	2.13	108.94	0.00
Residual	93	1.82	0.02		
Total	94	3.95			
	Coefficients	Standard Error		t Stat	P-value
Intercept	0.01	0.01		0.55	0.59
Model	0.80	0.08		10.44	0.00

Zone 12: Saturn Rainfall Cycle Model

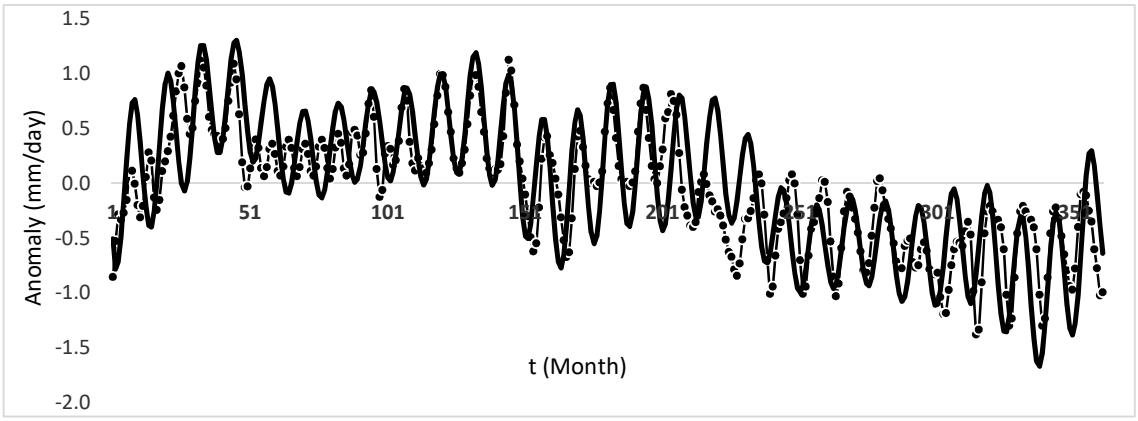

Figure 74: Variation of the mean Rainfall Anomaly (mm/day) and the fitted model curve in the Saturn 30-year cycle beginning at Saturn in Opposition phase in January.

The fitted curve;

$$RR_{♄} = [0.5\sin(0.0174(t-30)) + 0.15\sin(0.0174(t+50)) + 0.2\sin(0.0395(t + 5)) + 0.1\sin(0.1398(t+10)) + 0.2\sin 0.0698(t-10)) + 0.45\sin(0.5058(t + 7))] * [1 + 0.4\sin(0.0349(t+50))] * 0.8 \quad (104)$$

The statistical summary of the relationship between the fitted curve and the rainfall anomaly;

Regression Statistics	
Multiple R	0.812
R Square	0.659
Adjusted R Square	0.658
Standard Error	0.315
Observations	359

	df	SS	MS	F-Ratio	Significance F
Regression	1	68.30	68.30	690.46	0.00
Residual	357	35.31	0.10		
Total	358	103.61			
	Coefficients	Standard Error	t Stat	P-value	
Intercept	-0.043	0.017	-2.598	0.010	
Model	0.784	0.030	26.277	0.000	

Annex 2: Dates of the Observed Phase for the Celestial Bodies

Table 15 :Observed and Expected Dates of VENUS at INFERIOR CONJUNCTION Phase (1900-2050)

Jan 01, 2046	Feb 02,1942	Mar 15,2049	Apr 01,1993	Jun 01, 2028
Jan 04, 2038	Feb 05,1934	Mar 18,2041	Apr 03,1985	Jun 03, 2020
Jan 06, 2030	Feb 07,1926	Mar 20,2033	Apr 06,1977	Jun 06, 2012
Jan 09, 2022	Feb 10,1918	Mar 23,2025	Apr 08,1969	Jun 08, 2004
Jan 11,2014	Feb 12,1910	Mar 25,2017	Apr 10,1961	Jun 10, 1996
Jan 13,2006	Feb 14,1902	Mar 27,2009	Apr 13,1953	Jun 13, 1988
Jan 16,1998		Mar 30,2001	Apr 15,1945	Jun 15, 1980
Jan 18,1990			Apr 18,1937	Jun 17, 1972
Jan 21,1982			Apr 20,1929	Jun 19, 1964
Jan 23,1974			Apr 22,1921	Jun 22, 1956
Jan 26,1966			Apr 25,1913	Jun 24, 1948
Jan 28,1958			Apr 27,1905	Jun 26, 1940
Jan 31,1950				Jun 29, 1932
			May 27, 2044	
			May 30, 2036	
Jul 01, 1924	Aug 06, 2047	Sep 01, 1959	Oct 16, 2050	Nov 02, 1994
Jul 03, 1916	Aug 08, 2039	Sep 03, 1951	Oct 19, 2042	Nov 05, 1986
Jul 06, 1908	Aug 11, 2031	Sep 06, 1943	Oct 21, 2034	Nov 07, 1978
Jul 08, 1900	Aug 13, 2023	Sep 08, 1935	Oct 24, 2026	Nov 10, 1970
	Aug 15, 2015	Sep 10, 1927	Oct 26, 2018	Nov 12, 1962
	Aug 18, 2007	Sep 13, 1919	Oct 29, 2010	Nov 15, 1954
	Aug 20, 1999	Sep 15, 1911	Oct 31, 2002	Nov 17, 1946
	Aug 22, 1991	Sep 17, 1903		Nov 20, 1938
	Aug 25, 1983			Nov 22, 1930
	Aug 27, 1975			Nov 25, 1922
	Aug 29, 1967			Nov 27, 1914
				Nov 30, 1906

Table 16: Observed and Expected Dates of JUPITER at OPPOSITION Phase (1900-2050)

Jan 01, 2002	Feb 02, 2003	Mar 04, 2004	Apr 03, 2005	May 01, 1911
Jan 02, 1919	Feb 03, 1920	Mar 05, 1921	Apr 04, 1922	May 04, 2006
Jan 05, 2014	Feb 06, 2015	Mar 08, 2016	Apr 07, 2017	May 05, 1923
Jan 06, 1931	Feb 07, 1932	Mar 09, 1933	Apr 08, 1934	May 09, 2018
Jan 10, 2026	Feb 11, 2027	Mar 12, 2028	Apr 12, 2029	May 10, 1935
Jan 11, 1943	Feb 11, 1944	Mar 13, 1945	Apr 13, 1946	May 13, 2030
Jan 14, 2038	Feb 15, 2039	Mar 16, 2040	Apr 17, 1958	May 14, 1947
Jan 15, 1955	Feb 16, 1956	Mar 17, 1957	Apr 16, 2041	May 17, 2042
Jan 19, 2050	Feb 20, 1968	Mar 21, 1969	Apr 21, 1970	May 18, 1959
Jan 20, 1967	Feb 24, 1980	Mar 26, 1981	Apr 26, 1982	May 23, 1971
Jan 24, 1979	Feb 28, 1909	Mar 30, 1993	Apr 30, 1994	May 27, 1983
Jan 29, 1908		Mar 31, 1910		
Jan 29, 1991				
Jun 01, 1912	Jul 04, 1996	Aug 04, 1985	Sep 05, 1974	Oct 02, 2034
Jun 01, 1995	Jul 05, 1913	Aug 05, 1902	Sep 10, 1986	Oct 03, 1951
Jun 05, 2007	Jul 09, 2008	Aug 09, 1997	Sep 12, 1903	Oct 07, 2046
Jun 06, 1924	Jul 10, 1925	Aug 10, 1914	Sep 16, 1998	Oct 08, 1963
Jun 10, 2019	Jul 14, 2020	Aug 14, 2009	Sep 17, 1915	Oct 13, 1975
Jun 10, 1936	Jul 15, 1937	Aug 15, 1926	Sep 21, 2010	Oct 18, 1904
Jun 15, 2031	Jul 19, 2032	Aug 20, 2021	Sep 22, 1927	Oct 18, 1987
Jun 15, 1948	Jul 19, 2032	Aug 21, 1938	Sep 26, 2022	Oct 23, 1999
Jun 20, 2043	Jul 20, 1949	Aug 25, 2033	Sep 27, 1939	Oct 24, 1916
Jun 20, 1960	Jul 24, 2044	Aug 26, 1950		Oct 29, 1928
Jun 24, 1972	Jul 25, 1961	Aug 30, 2045		Oct 29, 2011
Jun 29, 1984	Jul 30, 1973	Aug 31, 1962		Oct 29, 1928
Jun 30, 1901				
Nov 03, 1940	Dec 03, 1929			
Nov 08, 2035	Dec 03, 2012			
Nov 03, 2023	Dec 07, 2024			
Nov 08, 1952	Dec 08, 1941			
Nov 13, 2047	Dec 12, 2036			
Nov 13, 1964	Dec 13, 1953			
Nov 18, 1976	Dec 17, 2048			
Nov 23, 1988	Dec 18, 1965			
Nov 24, 1905	Dec 23, 1977			
Nov 28, 2000	Dec 27, 1989			
Nov 29, 1917	Dec 28, 1906			

Years with No Opposition 1930,1942, 1954, 1966, 1978, 1990, 2001, 2013, 2025

Table 17: Observed and Expected Dates of VENUS at SUPERIOR CONJUNCTION Phase (1900-2050)

Jan 01, 2042	Feb 01, 1946	Mar 18, 2045	Apr 02, 1997	Jun 04, 2024
Jan 04, 2034	Feb 04, 1938	Mar 21, 2037	Apr 04, 1989	Jun 02, 2032
Jan 06, 2026	Feb 06, 1930	Mar 23, 2029	Apr 07, 1981	Jun 06, 2016
Jan 09, 2018	Feb 09, 1922	Mar 26, 2021	Apr 09, 1973	Jun 09, 2008
Jan 11, 2010	Feb 11, 1914	Mar 28, 2013	Apr 12, 1965	Jun 11, 2000
Jan 14, 2002	Feb 14, 1906	Mar 31, 2005	Apr 14, 1957	Jun 13, 1992
Jan 17, 1994			Apr 16, 1949	Jun 15, 1984
Jan 19, 1986			Apr 19, 1941	Jun 18, 1976
Jan 22, 1978			Apr 21, 1933	Jun 20, 1968
Jan 24, 1970			Apr 24, 1925	Jun 22, 1960
Jan 27, 1962			Apr 26, 1917	Jun 24, 1952
Jan 30, 1954			Apr 28, 1909	Jun 27, 1944
				Jun 29, 1936
			May 28, 2048	
			May 31, 2040	

Jul 01, 1928	Aug 07, 2043	Sep 01, 1955	Oct 15 2046	Nov 01 1990
Jul 03, 1920	Aug 09, 2035	Sep 03, 1947	Oct 18 2038	Nov 04 1982
Jul 06, 1912	Aug 12, 2027	Sep 05, 1939	Oct 22 2022	Nov 06 1974
Jul 08, 1904	Aug 14, 2019	Sep 08, 1931	Oct 25 2014	Nov 09 1966
	Aug 16, 2011	Sep 10, 1923	Oct 27 2006	Nov 11 1958
	Aug 18, 2003	Sep 12, 1915	Oct 30 1998	Nov 14 1950
	Aug 21, 1995	Sep 15, 1907		Nov 16 1942
	Aug 23, 1987			Nov 19 1934
	Aug 25, 1979			Nov 21 1926
	Aug 27, 1971			Nov 24 1918
	Aug 30, 1963			Nov 26 1910
				Dec 29 2049

Table 18: Observed and Expected Dates of NEW MOON Phase in the month of March (1900-2025)

1-5th	6-10th	11-15th	16-20th	21-25th	26-31st
1908	1902	1907	1901	1906	1900
1916	1905	1910	1904	1909	1903
1919	1913	1915	1912	1917	1911
1924	1921	1918	1920	1925	1914
1927	1932	1926	1923	1928	1922
1935	1940	1929	1931	1936	1930
1946	1943	1934	1942	1939	1933
1954	1948	1937	1950	1944	1938
1957	1951	1945	1958	1947	1941
1965	1959	1953	1961	1952	1949
1973	1962	1956	1969	1955	1960
1984	1970	1964	1980	1963	1968
1992	1978	1967	1988	1966	1971
2003	1981	1972	1991	1974	1976
2011	1986	1975	1996	1982	1979
2014	1989	1977	1999	1985	1987
2022	1997	1983	2004	1993	1990
	2000	1994	2007	2001	1995
	2005	2002	2015	2012	1998
	2008	2010	2018	2020	2006
	2016	2013		2023	2009
	2019	2021			2017
	2024				2025

Table 19 :Observed and Expected Dates of FULL MOON Phase in the month of March (1900-2050)

1-5th	6-10th	11-15th	16-20th	21-25th	26-31st
1901	1906	1903	1900	1902	1904
1904	1909	1911	1908	1905	1907
1912	1917	1914	1916	1910	1915
1915	1925	1922	1919	1913	1918
1920	1928	1930	1927	1921	1926
1923	1936	1941	1935	1924	1934
1931	1944	1949	1946	1929	1937
1939	1947	1952	1954	1932	1945
1942	1955	1960	1957	1940	1953
1950	1963	1968	1965	1943	1956
1958	1966	1971	1973	1948	1964
1961	1974	1979	1976	1951	1967
1969	1982	1987	1981	1959	1972
1977	1985	1990	1984	1962	1975
1980	1993	1998	1992	1970	1983
1988	2001	2006	1995	1978	1986
1996	2004	2009	2000	1989	1991
2007	2012	2017	2003	1997	1994
2015	2020	2025	2011	2005	1999
2026	2023	2028	2014	2008	2002
2034	2031	2036	2022	2016	2010
2037	2039	2044	2030	2019	2013
2045	2042	2047	2033	2024	2018
			2041	2027	2021
			2049	2035	2029
				2038	2032
				2046	2040
					2043
					2048

Table 20: Observed and Expected Dates of MARS at OPPOSITION phase (1900-2050)

Jan 02, 2040	Feb 04, 1963	Mar 01, 1933	Apr 06, 1935	May 01, 1952
Jan 05, 1914	Feb 06, 2042	Mar 03, 2012	Apr 08, 2014	May 04, 2031
Jan 07, 1993	Feb 10, 1916	Mar 09, 1965	Apr 15, 1967	May 08, 1905
Jan 14, 1946	Feb 12, 1995	Mar 11, 2044	Apr 17, 2046	May 11, 1984
Jan 16, 2025	Feb 17, 1948	Mar 15, 1918	Apr 21, 1920	May 22, 2016
Jan 21, 1978	Feb 19, 2027	Mar 23, 1950	Apr 24, 1999	May 31, 1969
Jan 27, 1931	Feb 22, 1901	Mar 25, 2029	Apr 24, 1982	
Jan 29, 2010	Feb 25, 1980	Mar 29, 1903		
		Mar 31, 1982		
		Mar 31, 1997		
Jun 03, 2048	Jul 06, 1907	Aug 10, 1971	Sep 10, 1956	Oct 10, 1941
Jun 10, 1922	Jul 10, 1986	Aug 14, 2050	Sep 15, 2035	Oct 13, 2020
Jun 13, 2001	Jul 23, 1939	Aug 23, 1924	Sep 24, 1909	Oct 25, 1973
Jun 24, 1954	Jul 27, 2018	Aug 28, 2003	Sep 28, 1988	
Jun 27, 2033				
Nov 04, 1926	Dec 05, 1943			
Nov 07, 2005	Dec 08, 2022			
Nov 16, 1958	Dec 15, 1975			
Nov 19, 2037	Dec 21, 1928			
Nov 25, 1911	Dec 28, 2007			
Nov 27, 1990	Dec 30, 1960			

Table 21: Observed and Expected Dates of MARS at CONJUNCTION (1900-2050)

Jan 06, 1947	Feb 01, 1932	Mar 04, 1996	Apr 02, 1981	May 02, 2045
Jan 09, 2026	Feb 04, 2011	Mar 17, 1949	Apr 14, 1934	May 09, 1919
Jan 16, 1900	Feb 17, 1964	Mar 21, 2028	Apr 18, 2013	May 22, 1951
Jan 20, 1979	Feb 20, 2043	Mar 30, 1902	Apr 29, 1966	May 25, 2030
	Feb 28, 1917			May 30, 1904
Jun 11, 1936	Jul 01, 2000	Aug 02, 1970	Sep 02, 2019	Oct 06, 1942
Jun 14, 2015	Jul 08, 1953	Aug 04, 2049	Sep 07, 1972	Oct 08, 2021
Jun 21, 1968	Jul 11, 2032	Aug 08, 1923	Sep 13, 1925	Oct 14, 1974
Jun 25, 2047	Jul 15, 1906	Aug 10, 2002	Sep 21, 1957	Oct 21, 1927
Jun 29, 1921	Jul 18, 1985	Aug 17, 1955	Sep 23, 2036	Oct 23, 2006
	Jul 24, 1938	Aug 19, 2034	Sep 27, 1910	Oct 30, 1959
	Jul 27, 2017	Aug 22, 1908	Sep 29, 1989	
		Aug 25, 1987		
		Aug 30, 1940		
Nov 01, 2038	Dec 03, 1929			
Nov 05, 1912	Dec 05, 2008			
Nov 08, 1991	Dec 14, 1961			
Nov 14, 1944	Dec 17, 2040			
Nov 18, 2023	Dec 24, 1914			
	Dec 27, 1993			

Table 22: Observed and Expected Dates of SATURN at OPPOSITION Phase (1900-2050)

1916 Jan 04	1977 Feb 02	1979 Mar 01	1952 Apr 01	1925 May 01
1975 Jan 06	2036 Feb 05	2038 Mar 03	2011 Apr 03	1984 May 03
2034 Jan 08	1948 Feb 09	1950 Mar 07	1982 Apr 09	2043 May 05
1946 Jan 12	2007 Feb 10	2009 Mar 08	1923 Apr 07	1955 May 09
2005 Jan 13	1919 Feb 14	1921 Mar 12	2041 Apr 10	1926 May 14
1917 Jan 17	1978 Feb 16	1980 Mar 14	1953 Apr 14	1927 May 26
1976 Jan 20	2037 Feb 17	2039 Mar 16	2012 Apr 15	1956 May 20
2035 Jan 22	1949 Feb 21	1951 Mar 20	1924 Apr 19	2014 May 10
1947 Jan 26	2008 Feb 24	2010 Mar 22	1983 Apr 21	1985 May 15
2006 Jan 27	1920 Feb 28	1922 Mar 25	2042 Apr 23	2044 May 17
1918 Jan 31		1981 Mar 27	1954 Apr 26	2015 May 23
		2040 Mar 28	2013 Apr 28	2045 May 29
				1986 May 28
1957 Jun 01	1930 Jul 01	2021 Aug 02	1994 Sep 01	1967 Oct 02
2016 Jun 03	1989 Jul 02	1933 Aug 05	1906 Sep 05	2026 Oct 04
1928 Jun 06	2048 Jul 03	1992 Aug 07	1965 Sep 06	1938 Oct 08
1987 Jun 09	1901 Jul 05	1904 Aug 10	2024 Sep 08	1997 Oct 10
2046 Jun 10	1960 Jul 07	1963 Aug 13	1936 Sep 12	1909 Oct 13
1958 Jun 13	2019 Jul 09	2022 Aug 14	1995 Sep 14	1968 Oct 15
2017 Jun 15	1931 Jul 13	1934 Aug 18	1907 Sep 18	2027 Oct 18
1929 Jun 19	1990 Jul 14	1993 Aug 19	1966 Sep 19	1939 Oct 22
1988 Jun 20	2049 Jul 16	1905 Aug 23	2025 Sep 21	1998 Oct 23
2047 Jun 22	1902 Jul 18	2023 Aug 27	1937 Sep 25	1910 Oct 27
1900 Jun 23	1961 Jul 19	1935 Aug 31	1996 Sep 26	1969 Oct 29
1959 Jun 26	2020 Jul 20		1908 Sep 30	2028 Oct 30
2018 Jun 27	1932 Jul 24			
	1991 Jul 27			
	2050 Jul 28			
	1903 Jul 30			
	1962 Jul 31			
1940 Nov 03	1942 Dec 01	Years with No Opposition 1915, 1945, 1974, 2004		
1999 Nov 06	2001 Dec 03			
1911 Nov 10	1913 Dec 07			
1970 Nov 11	1972 Dec 09			
2029 Nov 13	2031 Dec 11			
1941 Nov 17	1943 Dec 15			
2000 Nov 19	2002 Dec 17			
1912 Nov 23	1914 Dec 21			
1971 Nov 25	1973 Dec 23			
2030 Nov 27	2032 Dec 24			
	1944 Dec 29			
	2003 Dec 31			